Nine Papers to be Presented at International Symposium on WAVES — PHYSICAL AND NUMERICAL MODELLING

RESEARCH REPORT NO. CACR-94-11

June 1994

CENTER FOR APPLIED COASTAL RESEARCH

Ocean Engineering Laboratory
University of Delaware
Newark, Delaware 19716

PREFACE

This report presents nine papers that will be presented at the INTERNATIONAL SYMPOSIUM ON WAVES – PHYSICAL AND NUMERICAL MODELLING which will be held at Vancouver, Canada during August 21–24, 1994. These papers are based on our ongoing research efforts to improve nearshore wave and circulation modelling.

ACKNOWLEDGEMENT

The work presented in the first six papers listed in the following Contents was supported by University Research Initiative Grant DAAL 03-92-G-0116 from the U.S. Army Research Office as acknowledged in each of the six papers.

CONTENTS

DERIVATION AND PROPERTIES OF A FULLY NONLINEAR MODEL FOR WEAKLY DISPERSIVE WAVES

James T. Kirby and Ge Wei
Center for Applied Coastal Research, University of Delaware,
Newark, DE 19716 USA

ABSTRACT

Fully nonlinear equations are derived for the propagation of weakly dispersive, long surface water waves. We study the properties of these equations using Stokes type perturbation expansions. In this paper, it is shown that the model improves the prediction (at second order) of amplitudes of bound sub- and superharmonic waves in intermediate water depth, relative to the predictions given by extended-dispersion models with consistent Boussinesq ordering. In the presentation, we further demonstrate that the principle features of modulated wave evolution at third order are correctly predicted.

INTRODUCTION

Standard Boussinesq models based on depth-averaged velocities have limitations on their range of application arrising both from small amplitude assumptions and from the assumption that the modelled waves are long relative to the water depth. The second limitation is apparent primarily through the linear terms of the model equation, which construct a polynomial approximation to the usual hyperbolic tangent behavior in the wave dispersion relation. Recent efforts by Madsen et al (1991, 1992) and Nwogu (1993, 1994) have shown that it is possible to construct rational polynomial dispersion relations that are relatively much more accurate in comparison to the full result, and which correspond to model equations which stay within the order of approximation of the standard Boussinesq model.

In this presentation, we extend the model of Nwogu to further include nonlinear effects to all orders. This leads to a model which should exhibit correct behavior to $O(\mu^2)$ dispersion at any order of an expansion in small nonlinearity δ. We test the accuracy of the resulting model by examining its behavior at second-order, in the generation of corrections to a random sea. In the presentation, we also examine the evolution of modulated swell waves due to self-interactions at third order. Tests of the model for strongly nonlinear evolution near

wave breaking in shallow water are described in Grilli et al (1994).

FULLY NONLINEAR MODEL EQUATION

We proceed, using standard techniques, to construct the fully nonlinear form of the governing equations based on a series solution for Laplace's equation in the fluid interior. Following Mei (1982), we use a reference wavenumber k_0 to scale horizontal distances x, y, a reference water depth h_0 to scale the vertical coordinate z and local depth $h(x,y)$, and amplitude a to scale the surface displacement η. We then introduce the parameters $\delta = a/h_0$ and $\mu^2 = (k_0 h_0)^2$. Based on these, we choose a scale of $(k_0(gh_0)^{1/2})^{-1}$ for time t and $\delta h_0(gh_0)^{1/2}/\mu$ for velocity potential ϕ. Introducing these scales into the boundary value problem for inviscid, irrotational motion leads to the problem

$$\phi_{zz} + \mu^2\nabla^2\phi = 0; \qquad -h \le z \le \delta\eta \tag{1}$$

$$\phi_z + \mu^2\nabla h\cdot\nabla\phi = 0; \qquad z = -h \tag{2}$$

$$\eta + \phi_t + \delta[(\nabla\phi)^2 + \frac{1}{\mu^2}(\phi_z)^2] = 0; \qquad z = \delta\eta \tag{3}$$

$$\eta_t + \delta\nabla\phi\cdot\nabla\eta - \frac{1}{\mu^2}\phi_z = 0; \qquad z = \delta\eta \tag{4}$$

We develop an equation expressing volume flux conservation by integrating (1) over z from $-h$ to $\delta\eta$ and using (2) and (4) to obtain

$$\eta_t + \nabla\cdot\mathbf{M} = 0; \qquad \mathbf{M} = \int_{-h}^{\delta\eta}\nabla\phi dz \tag{5}$$

In the following, we use (5) to obtain expressions for mass conservation, while a momentum equation is obtained using the gradient of the Bernoulli equation (3).

Approximate expression for the velocity potential

As in previous studies of weakly dispersive shallow water waves, we reduce the dimensionality of the boundary value problem by introducing a series expansion for ϕ. An expression for ϕ which retains terms to $O(\mu^2)$ and satisfies the bottom boundary condition is given by

$$\phi = \phi_0(\mathbf{x},t) - \mu^2(h+z)\nabla h\cdot\nabla\phi_0 - \mu^2\frac{(h+z)^2}{2}\nabla^2\phi_0 + O(\mu^4) \tag{6}$$

where ϕ_0 is the value of the velocity potential at $z = -h$. In practice, we may replace ϕ_0 by the value of the potential at any level in the water column. Any choice will lead to a set of model equations with the same level of asymptotic approximation but with numerically different dispersion properties. Following Nwogu (1993) and Chen and Liu (1993), we denote ϕ_α as the value of ϕ at $z = z_\alpha$, or

$$\phi_\alpha = \phi_0 - \mu^2(h+z_\alpha)\nabla h\cdot\nabla\phi_0 - \mu^2\frac{(h+z_\alpha)^2}{2}\nabla^2\phi_0 + O(\mu^4) \tag{7}$$

This expression is then used in (6) to obtain an expression for ϕ in terms of ϕ_α:

$$\phi = \phi_\alpha + \mu^2(z_\alpha - z)\nabla\cdot(h\nabla\phi_\alpha) + \frac{1}{2}\mu^2(z_\alpha^2 - z^2)\nabla^2\phi_\alpha + O(\mu^4) \tag{8}$$

This form of the velocity potential is then used in the governing equations to obtain the approximate models.

Two-equation model for η and ϕ_α

First, a two-equation model for η and ϕ_α is developed. The expression for $\mathbf{M}$ in (5) becomes

$$\begin{aligned}\mathbf{M} &= (h+\delta\eta)\left[\nabla\phi_\alpha + \mu^2\left\{\nabla\left[z_\alpha\nabla\cdot(h\nabla\phi_\alpha) + \frac{z_\alpha^2}{2}\nabla^2\phi_\alpha\right]\right.\right.\\ &\left.\left. + \frac{(h-\delta\eta)}{2}\nabla(\nabla\cdot(h\nabla\phi_\alpha)) - \frac{(h^2 - h\delta\eta + (\delta\eta)^2)}{6}\nabla^2\nabla\phi_\alpha\right\}\right]\end{aligned} \tag{9}$$

which clearly goes to zero identically as the total depth $h+\delta\eta$ goes to zero. We note that Nwogu's mass conservation equation does not exhibit this property, which makes a specification of a shoreline boundary condition potentially difficult for his form of the Boussinesq approximation.

The corresponding form of the Bernoulli equation (3) becomes

$$\begin{aligned}&\eta + \phi_{\alpha t} + \frac{\delta}{2}(\nabla\phi_\alpha)^2 + \mu^2\left[(z_\alpha - \delta\eta)\nabla\cdot(h\nabla\phi_{\alpha t}) + \frac{1}{2}(z_\alpha^2 - (\delta\eta)^2)\nabla^2\phi_{\alpha t}\right]\\ &+\delta\mu^2\left\{\nabla\phi_\alpha\cdot\left[\nabla z_\alpha\nabla\cdot(h\nabla\phi_\alpha) + (z_\alpha - \delta\eta)\nabla(\nabla\cdot(h\nabla\phi_\alpha)) + z_\alpha\nabla z_\alpha\nabla^2\phi_\alpha\right.\right.\\ &\left.\left.+\frac{1}{2}(z_\alpha^2 - (\delta\eta)^2)\nabla(\nabla^2\phi_\alpha)\right] + \frac{1}{2}[\nabla\cdot(h\nabla\phi_\alpha)]^2 + \delta\eta\nabla\cdot(h\nabla\phi_\alpha)\nabla^2\phi_\alpha + \frac{1}{2}(\delta\eta)^2(\nabla^2\phi_\alpha)\right\} = 0\end{aligned} \tag{10}$$

Equations at the order of approximation of the usual Boussinesq theory may be immediately obtained by neglecting terms of $O(\delta)$ or higher in the $O(\mu^2)$ dispersive terms. The modified expression for volume flux $\mathbf{M}$ is

$$\begin{aligned}\mathbf{M} &= (h+\delta\eta)\nabla\phi_\alpha + \mu^2\left\{h\nabla\left[z_\alpha\nabla\cdot(h\nabla\phi_\alpha) + \frac{z_\alpha^2}{2}\nabla^2\phi_\alpha\right]\right.\\ &\left. + \frac{h^2}{2}\nabla(\nabla\cdot(h\nabla\phi_\alpha)) - \frac{h^3}{6}\nabla^2\nabla\phi_\alpha\right\}\end{aligned} \tag{11}$$

and the Bernoulli equation reduces to

$$\eta + \phi_{\alpha t} + \frac{\delta}{2}(\nabla\phi_\alpha)^2 + \mu^2\left[z_\alpha\nabla\cdot(h\nabla\phi_{\alpha t}) + \frac{1}{2}z_\alpha^2\nabla^2\phi_{\alpha t}\right] = 0 \tag{12}$$

These results may be compared to the two-equation model of Wu (1981), which uses the depth averaged value of ϕ. The models are the same to within rearrangements of dispersive terms.

Three equation model based on η and $\mathbf{u}_\alpha$

We further introduce a horizontal velocity $\mathbf{u}_\alpha$ as $\mathbf{u}_\alpha = \nabla\phi|_{z_\alpha}$. Retaining terms to $O(\mu^2)$ and to all orders in δ gives a fully nonlinear version of the model with volume flux

$$\begin{aligned}\mathbf{M} &= (h+\delta\eta)\left[\mathbf{u}_\alpha + \mu^2\left\{\left[\frac{1}{2}z_\alpha^2 - \frac{1}{6}(h^2 - h\delta\eta + (\delta\eta)^2)\right]\nabla(\nabla\cdot\mathbf{u}_\alpha)\right.\right.\\ &\left.\left. + \left[z_\alpha + \frac{1}{2}(h-\delta\eta)\right]\nabla(\nabla\cdot(h\mathbf{u}_\alpha))\right\}\right] + O(\mu^4) \qquad (13)\end{aligned}$$

and momentum equation

$$\mathbf{u}_{\alpha t} + \delta(\mathbf{u}_\alpha\cdot\nabla)\mathbf{u}_\alpha + \nabla\eta + \mu^2\mathbf{V_1} + \delta\mu^2\mathbf{V_2} = O(\mu^4) \qquad (14)$$

where

$$\mathbf{V_1} = \frac{1}{2}z_\alpha^2\nabla(\nabla\cdot\mathbf{u}_{\alpha t}) + z_\alpha\nabla(\nabla\cdot(h\mathbf{u}_{\alpha t})) - \nabla\left[\frac{1}{2}(\delta\eta)^2\nabla\cdot\mathbf{u}_{\alpha t} + \delta\eta\nabla\cdot(h\mathbf{u}_{\alpha t})\right] \qquad (15)$$

$$\begin{aligned}\mathbf{V_2} &= \nabla\left[(z_\alpha - \delta\eta)(\mathbf{u}_\alpha\cdot\nabla)(\nabla\cdot(h\mathbf{u}_\alpha)) + \frac{1}{2}(z_\alpha^2 - (\delta\eta)^2)(\mathbf{u}_\alpha\cdot\nabla)(\nabla\cdot\mathbf{u}_\alpha)\right]\\ &\quad + \frac{1}{2}\nabla\left[(\nabla\cdot(h\mathbf{u}_\alpha) + \delta\eta\nabla\cdot\mathbf{u}_\alpha)^2\right] \qquad (16)\end{aligned}$$

The Boussinesq approximation of Nwogu (1993) is recovered by neglecting terms of $O(\mu^4, \delta\mu^2)$, yielding the expressions

$$\mathbf{M} = (h+\delta\eta)\mathbf{u}_\alpha + \mu^2\left\{\left(\frac{hz_\alpha^2}{2} - \frac{h^3}{6}\right)\nabla(\nabla\cdot\mathbf{u}_\alpha) + \left(hz_\alpha + \frac{h^2}{2}\right)\nabla(\nabla\cdot(h\mathbf{u}_\alpha))\right\} \qquad (17)$$

and

$$\mathbf{u}_{\alpha t} + \delta(\mathbf{u}_\alpha\cdot\nabla)\mathbf{u}_\alpha + \nabla\eta + \mu^2\left\{\frac{z_\alpha^2}{2}\nabla(\nabla\cdot\mathbf{u}_{\alpha t}) + z_\alpha\nabla(\nabla\cdot(h\mathbf{u}_{\alpha t}))\right\} = O(\delta\mu^2, \mu^4) \qquad (18)$$

STOKES EXPANSION IN POWERS OF δ

In intermediate water depths, the first nonlinear correction to a homogeneous random sea takes the form of a set of bound, non-resonant superharmonics and a corresponding set of bound, non-resonant subharmonics. Nwogu (1994) has shown that the extended Boussinesq model gives transfer coefficients which are qualitatively similar to those predicted by the second-order Stokes theory (Dean and Sharma, 1981), but which differ quantitatively by as much as 50% within the range of frequencies for which the linearized form of the model is felt to be accurate. Similar results have been shown by Madsen and Sørensen (1993). The present theory provides $O(\mu^2)$ corrections to the transfer coefficients, and we test whether the modified coefficients have improved accuracy relative to the full theory.

The derivation in the present case is simpler starting from the two-equation model for η and ϕ_α. We proceed by truncating the model equations to $O(\delta^2)$, corresponding to the

retention of cubic nonlinear terms. We then introduce the expansions $\eta = \eta_0 + \delta\eta_1$ and $\phi_\alpha = \phi_0 + \delta\phi_1$ (where subscripts now refer to ordering in the expansions) and order the resulting set of equations by powers of δ. At $O(\delta^0)$, the resulting linear system is given by

$$\eta_{0t} + h\nabla^2\phi_0 + \mu^2 h^3(\alpha + \frac{1}{3})\nabla^2(\nabla^2\phi_0) = 0 \tag{19}$$

$$\phi_{0t} + \eta_0 + \mu^2 h^2 \alpha \nabla^2 \phi_{0t} = 0 \tag{20}$$

where $\alpha = (z_\alpha/h)(1 + (z_\alpha/h)/2)$. At $O(\delta)$, we obtain the set of equations

$$\eta_{1t} + h\nabla^2\phi_1 + \mu^2 h^3(\alpha + \frac{1}{3})\nabla^2(\nabla^2\phi_1) = -\nabla\cdot(\eta_0\nabla\phi_0) - \mu^2 h^2\alpha\nabla\cdot(\eta_0\nabla(\nabla^2\phi_0)) \tag{21}$$

$$\phi_{1t} + \eta_1 + \mu^2 h^2\alpha\nabla^2\phi_{1t} = -\frac{1}{2}(\nabla\phi_0)^2 + \mu^2\left\{h\eta_0\nabla^2\phi_{0t} - h^2\alpha\nabla\phi_0\cdot\nabla(\nabla^2\phi_0) - \frac{1}{2}h^2(\nabla^2\phi_0)^2\right\} \tag{22}$$

These equations differ from the set of perturbation equations obtained by Nwogu (1994) in the inclusion of $O(\mu^2)$ terms in the forcing terms on the right hand side. It is clear from this result that the coupling coefficients derived by Nwogu (1993, 1994) or Madsen et al (1993) are not consistent to $O(\mu^2)$ due to the lack of the appropriate correction in the forcing.

FORCED SECOND-ORDER SEA

Introducing a linear random sea of the form

$$\eta_0 = \sum_n a_n\cos\psi_n, \quad \phi_0 = \sum_n b_n\sin\psi_n, \quad \psi_n = \mathbf{k_n}\cdot\mathbf{x} - \omega_n t + \epsilon_n \tag{23}$$

in (19 - 20) gives the results

$$\omega_n^2 = k_n^2 h(1 - (\alpha + \frac{1}{3})\mu^2(k_n h)^2)/(1 - \alpha\mu^2(k_n h)^2) \tag{24}$$

$$b_n = \omega_n a_n / \left[k_n^2 h[1 - \mu^2(\alpha + \frac{1}{3})(k_n h)^2]\right] \tag{25}$$

which agree with the linear dispersion relation given by Nwogu (1993). Substituting the linear solutions in (21) and (22) and evaluating the right hand sides leads to the system

$$\eta_{1t} + h\nabla^2\phi_1 + \mu^2 h^3(\alpha + \frac{1}{3})\nabla^2(\nabla^2\phi_1) = \frac{1}{4}\sum_m\sum_l a_m a_l\left[\mathcal{F}_{ml}^+\sin(\psi_m + \psi_l) + \mathcal{F}_{ml}^-\sin(\psi_m - \psi_l)\right] \tag{26}$$

$$\phi_{1t} + \eta_1 + \mu^2 h^2\alpha\nabla^2\phi_{1t} = \frac{1}{4}\sum_m\sum_l a_m a_l\left[\mathcal{G}_{ml}^+\cos(\psi_m + \psi_l) + \mathcal{G}_{ml}^-\cos(\psi_m - \psi_l)\right] \tag{27}$$

where

$$\mathcal{F}_{ml}^\pm = \frac{\omega_l k_m^2 \pm \omega_m k_l^2 + \omega_{ml}^\pm \mathbf{k}_m\cdot\mathbf{k}_l}{\omega_m\omega_l} \tag{28}$$

and

$$\mathcal{G}_{ml}^\pm = \frac{-\omega_m\omega_l(\mathbf{k}_m\cdot\mathbf{k}_l)(1 - \mu^2h^2\alpha(k_m^2 + k_l^2) + \mu^2h^2(\pm\omega_m\omega_l k_m^2 k_l^2 + \omega_m^2 k_m^2 K_l k_l + \omega_l^2 k_l^2 K_m k_m)}{K_m K_l k_m k_l h^2} \tag{29}$$

The expression for $\mathcal{F}$ agrees exactly with the corresponding expression obtained from Stokes theory (Dean and Sharma, 1981), aside from differences in the evaluation of the wavenumbers from the true vs. approximate dispersion relations. The expression for $\mathcal{G}$ may be rearranged to the form

$$\mathcal{G}^{\pm}_{ml} = \frac{-\mathbf{k}_m \cdot \mathbf{k}_l + \mu^2(\omega_m\omega_l(\omega_m^2 + \omega_l^2) \pm \omega_m^2\omega_l^2)}{\omega_m\omega_l} + O(\mu^4) \tag{30}$$

This is equivalent to the form obtained from Stokes theory after neglect of the $O(\mu^4)$ terms, which may be done consistently owing to the level of approximation in the governing equations. We compare results obtained both with and without this last step below. Finally, we obtain an expression for the bound second order water surface η_1 given by

$$\eta_1 = \frac{1}{2}\sum_m\sum_l a_m a_l G^+_{ml}\cos(\psi_m + \psi_l) + \frac{1}{2}\sum_m\sum_l a_m a_l G^-_{ml}\cos(\psi_m - \psi_l) \tag{31}$$

where the first term represents superharmonic components and the last term represents subharmonics, and where

$$G^{\pm}_{ml} = \frac{1}{4}\frac{\omega^{\pm}_{ml}\mathcal{F}^{\pm}_{ml} - k^{\pm}_{ml}T^{\pm}_{ml}\mathcal{G}^{\pm}_{ml}}{(\omega^{\pm}_{ml})^2/g - k^{\pm}_{ml}T^{\pm}_{ml}} \tag{32}$$

Other terms used in the expressions above are defined according to

$$K_m = k_m(1 - \mu^2(\alpha + \frac{1}{3})(k_m h)^2) \tag{33}$$

$$\omega^{\pm}_{ml} = \omega_m \pm \omega_l \tag{34}$$

$$k^{\pm}_{ml} = |\mathbf{k}_m \pm \mathbf{k}_l| \tag{35}$$

$$T^{\pm}_{ml} = k^{\pm}_{ml}h\frac{1 - (\alpha + \frac{1}{3})\mu^2(k^{\pm}_{ml}h)^2}{1 - \alpha\mu^2(k^{\pm}_{ml}h)^2} \tag{36}$$

We proceed by comparing values of $G^{\pm}$ to values obtained from full Stokes theory (Dean and Sharma, 1981) and the extended Boussinesq model of Nwogu (1994). In Figure 1, we show the normalized superharmonic coupling coefficient as a function of depth for the case where the two linear component waves have a frequency separation of 10%. l_0 denotes the deepwater wavelength corresponding to the center frequency of the pair of linear wave components. In the figure, solid curves denote full Stokes theory, dashed curves indicate the extended Boussinesq theory of Nwogu, and the dash-dot curve denotes the present theory. The upper set of curves corresponds to the case where the two linear waves are propagating in the same direction, while the bottom set corresponds to the case of a separation of 40° between the two components. In both cases, it is seen that the present theory (based here on the expression (29) for $\mathcal{G}$) provides a more consistent approximation to the full theory except at large depths, where the form of the error in the Nwogu theory leads to a fortuitously better prediction. We remark that if the expression (30) for $\mathcal{G}$ is used, then the maximum error over the entire range is on the order of 2%.

In Figure 2, similar results are shown for the subharmonics, with similar overall conclusions.

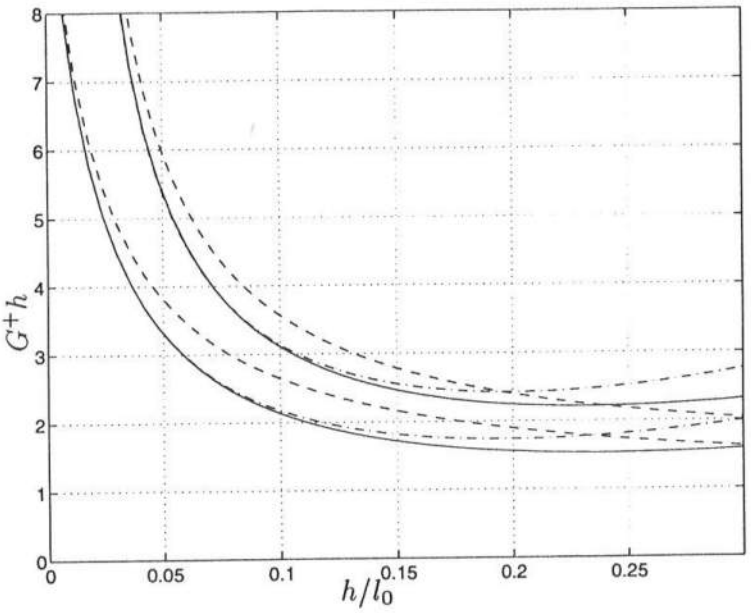

Figure 1: Superharmonic coupling coefficient for waves with 10% frequency separation. Solid line - Stokes theory; Dash line - Nwogu (1994); Dash-dot line - present theory. Upper curves - $\Delta\theta = 0°$. Lower curves - $\Delta\theta = 40°$.

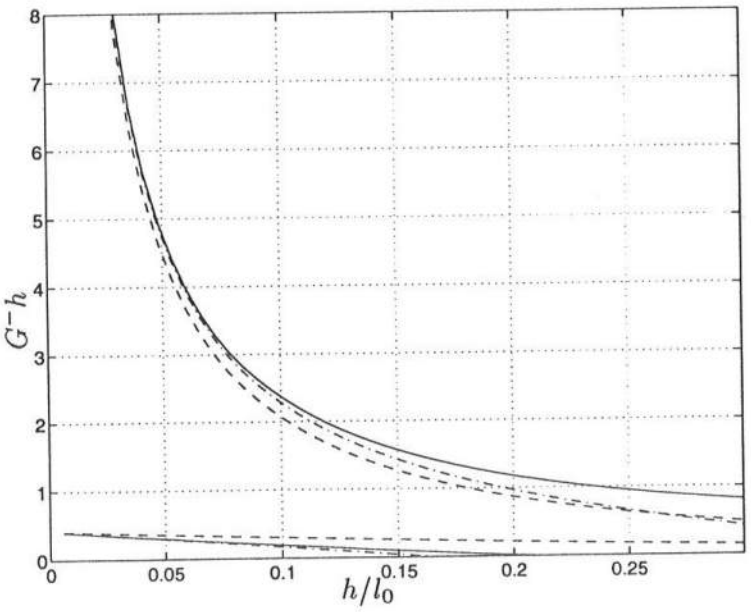

Figure 2: Subharmonic coupling coefficient for waves with 10% frequency separation. Solid line - Stokes theory; Dash line - Nwogu (1994); Dash-dot line - present theory. Upper curves - $\Delta\theta = 0°$. Lower curves - $\Delta\theta = 40°$.

In Figure 3, we show an alternate view of the accuracy of the prediced coupling coefficients for three versions of the weakly dispersive theory. In each plot, we show the ratio of the value of G predicted by the weakly dispersive theory to the value predicted by the theory of Dean and Sharma (1981), where we vary the frequencies of the two component linear waves over a wide range with water depth held fixed. All the results shown are for the case where the linear component waves are propagating in the same direction. The column of results on the left refer to superharmonics, while the column on the right refers to subharmonics. Figures 3a and b give results for transfer coefficients derived from Nwogu's equation, where errors of $O(\mu^2)$ appear in the second-order forcing terms. Figures 3c and d show the same results for the present theory with $\mathcal{G}$ given by (29). We see that the prediction of the transfer function is generally more accurate for the present theory except for large values of ω, where the form of the transfer function obtained from Nwogu's equations leads to fortuitously better agreement. In Figures 3e and f, results are shown for G computed using the form (30) of $\mathcal{G}$. These results show close agreement between the Stokes and present theories, with maximum errors overall on the order of 2%, which coincides with the level of errors in the model-predicted dispersion relation.

CONCLUSIONS

We have shown here that a fully nonlinear variant of the extended Boussinesq theory of Nwogu (1993) provides better predictions of bound second-order components of a random wave train over the range of validity of Boussinesq theory. We have shown that this range can be extended by a consistent rearrangement of terms to give results which are accurate over the claimed extent of validity of the extended Boussinesq theory. However, we caution that this extension involves the effective rearrangement of higher-order dispersive terms in the original governing equation, and thus the accuracy of those results will not be reproduced by direct numerical simulations based on the given equations.

This paper and the companion paper by Grilli et al (1994) show that several of the deficiencies remaining in the Boussinesq theory may be improved by the simple retention of all nonlinear effects, leaving weak dispersion as the only asymptotic approximation in the theory. This step does not conceptually complicate the resulting model equations and appears to be worth the effort involved. We have further evidence that significant improvements may be obtained by retaining dispersive properties to $O(\mu^4)$, and work in this direction is being pursued.

Acknowledgements

This work was supported by University Research Initiative Grant DAAL 03-92-G-0116 from the Army Research Office.

REFERENCES

Chen, Y. and Liu, P. L.-F. 1993. Modified Boussinesq equations and associated parabolic models for wave propagation. Research Report CACR-93-06, Center for Applied Coastal Research, University of Delaware, Newark.

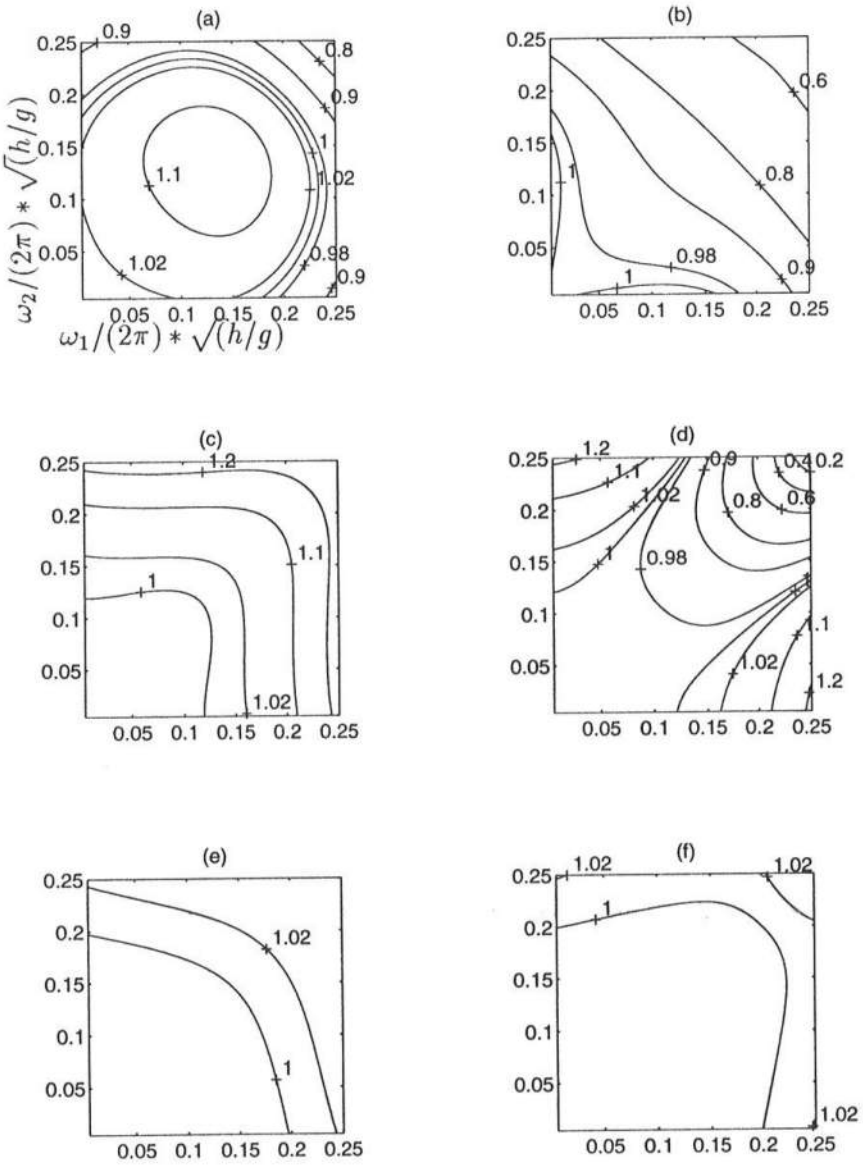

Figure 3: Ratio of model predicted $G^{\pm}$ to value from Stokes theory. (a,c,e) - Superharmonics; (b,d,f) - Subharmonics. $\Delta\theta = 0$. (a,b) - Nwogu equation; (c,d) - present theory using equation (29); (e,f) - present theory using equation (30).

Dean, R. G. and Sharma, J. N. 1981. Simulation of wave systems due to nonlinear directional spectra. *Proc. Int. Symp. on Hydrodynamics in Ocean Engineering*, Trondheim, 1211-1222.

Grilli, S. T., Subramanya, R., Kirby, J. T. and Wei, G. 1994. Comparison of modified Boussinesq and fully nonlinear potential models for shoaling solitary waves. *Proc. Intl. Symp. Waves - Physical and Numerical Modelling*, Vancouver, August 21-24.

Madsen, P. A., Murray, R. and Sørensen, O. R. 1991. A new form of the Boussinesq equations with improved linear dispersion characteristics. *Coastal Engineering*, 15, 371-388.

Madsen, P. A., and Sørensen, O. R. 1992. A new form of the Boussinesq equations with improved linear dispersion characteristics. Part 2. A slowly-varying bathymetry. *Coastal Engineering*, 18, 183-204.

Madsen, P. A. and Sørensen, O. R. 1993. Bound waves and triad interactions in shallow water. *Ocean Engineering*, 20, 359-388.

Mei, C. C. 1989. *The Applied Dynamics of Ocean Surface Waves*, World Scientific.

Nwogu, O. 1993. An alternative form of the Boussinesq equations for nearshore wave propagation. *J. Waterway, Port, Coastal and Ocean Engineering*, 119, 618-638.

Nwogu, O. 1994. Nonlinear transformation of multi-directional waves in water of variable depth. submitted to *J. Fluid Mech.*

Wu, T. Y. T. 1981. Long waves in ocean and coastal waters. *J. Engineering Mechanics*, 107, 501-522.

A HIGH ORDER TIME-DEPENDENT NUMERICAL MODEL FOR THE EXTENDED BOUSSINESQ EQUATIONS

Ge Wei and James T. Kirby
Center for Applied Coastal Research, University of Delaware,
Newark, Delaware 19716 USA

ABSTRACT

A numerical code for the extended Boussinesq equations derived by Nwogu (1993) is developed. The model utilizes a fourth-order predictor-corrector method to advance in time, and discretizes first order spatial derivatives to fourth-order accuracy, thus reducing all truncation errors to a level smaller than the dispersive terms retained by the model. The basic numerical scheme is described and the model is applied to several examples of wave propagation in variable depth. These initial results indicate that the model is capable of simulating wave transformation from relatively deep water to shallow water, giving accurate predictions of the height and shape of shoaled waves.

INTRODUCTION

The ability to accurately predict wave transformation from deep to shallow water is vital to an understanding of coastal processes. As waves propagate toward shore, a combination of shoaling, refraction and diffraction effects modify the wave form. Nonlinear effects induce energy transfers both up and down the spectrum, leading to the generation of low-frequency surf-beat as well as high-frequency corrections (enhancements) to the shoaling wave crests.

Boussinesq-type equations, which include the lowest order effects of nonlinearity and frequency dispersion, have been shown to provide an accurate description of wave evolution in coastal regions, if used within the bounds of the validity of the underlying approximations. The first such set of equations for variable depth was derived by Peregrine (1967), and use the surface displacement η and a depth-averaged horizontal velocity $\overline{u}$ as dependent variables. Using frequency-domain formulations derived from Peregrine's equations, Freilich and Guza

(1984) and Elgar and Guza (1985) have demonstrated that the evolution of power spectra of normally incident waves may be accurately predicted, while Elgar and Guza (1986) and Elgar et al (1990) have shown that the evolution of bispectra or third-moment statistics is also well predicted. Freilich et al (1993) provided evidence that the frequency domain model also correctly predicts the shoreward evolution of a directional wave train. Similar success has been noted in comparisons between laboratory data and model predictions. Goring (1978) has shown that the models give good predictions of the scattering and transmission of solitary waves at depth transitions, while Liu et al (1985) and Rygg (1988) have demonstrated that accurate predictions of wave refraction and focussing by underwater shoals may be made (Whalin, 1971). Kirby (1990) has shown that an angular spectrum formulation of the standard Boussinesq model gave good predictions of the evolution of a Mach stem measured in the laboratory (Hammack et al, 1990).

Due to increasing error in the modelled linear dispersion relation with increasing water depth, the standard Boussinesq equations are limited to relatively shallow water. Recently, efforts have been made by a number of investigators to derive alternative forms of Boussinesq equations which can be applied in deeper water regions (Witting, 1984; Murray, 1989; Madsen et al., 1991; Nwogu, 1993). Of these models, the two by Madsen et al and Nwogu have generated the most interest. Each model is different in the form and arrangement of dispersive terms, but both lead to a dispersion relation which may be interpreted as being a Padé approximant of the full linear dispersion relation. This result is significant since the resulting dispersion relation may be interpreted as being accurate through $O(\mu^4)$, even though the Boussinesq model equations are derived to provide a correction to $O(\mu^2)$ to the shallow water theory ($\mu = O(kh)$). Of these two models, the Boussinesq equations derived by Nwogu (1993) are obtained through a consistent derivation from the continuity and Euler equations of motion. In the derivation, the horizontal velocity at an arbitrary depth is used as the dependent variable. The depth at which the velocity is evaluated is then determined from the resulting dispersion relation compared with that of linear theory. As a result, the new form of equations are found to be able to predict the propagation of waves in water which is relatively much deeper than allowed by the standard approximation.

In this study, we develop a high-order numerical model based on Nwogu's Boussinesq equations. We use a fourth-order predictor-corrector scheme for time stepping and discretize the first order spatial derivatives to fourth-order accuracy. This discretization automatically eliminates error terms which would be of the same form as the dispersive terms, and which must therefore be corrected for if lower order schemes are used. The model is applied to several cases of wave propagation from relatively deep to shallow water. Numerical results are compared with experimental data when available.

GOVERNING EQUATIONS

The new form of Boussinesq equations derived by Nwogu (1993) are given by

$$\eta_t + \nabla \cdot [(h+\eta)\boldsymbol{u}] + \nabla \cdot \left\{ \left(\frac{{z_\alpha}^2}{2} - \frac{h^2}{6} \right) h \nabla (\nabla \cdot \boldsymbol{u}) + \left(z_\alpha + \frac{h}{2} \right) h \nabla [\nabla \cdot (h\boldsymbol{u})] \right\} = 0 \qquad (1)$$

$$\boldsymbol{u}_t + g\nabla\eta + (\boldsymbol{u}\cdot\nabla)\boldsymbol{u} + z_\alpha\left\{\frac{z_\alpha}{2}\nabla(\nabla\cdot\boldsymbol{u}_t) + \nabla[\nabla\cdot(h\boldsymbol{u}_t)]\right\} = 0 \qquad (2)$$

where η is the surface elevation, h is the local water depth, $\boldsymbol{u} = (u, v)$ is the horizontal velocity at an arbitrary depth z_α, $\nabla = (\partial/\partial x, \partial/\partial y)$ is the horizontal gradiant operator, and g is the gravitational acceleration. The above equations are statements of conservation of mass and momentum, respectively. Compared to the standard Boussinesq equations derived by Peregrine (1967), there is an additional dispersive term in the continuity equation, and the coefficients of dispersive terms in the momentum equations are different. As will be shown below, it is these differences that improve the linear dispersive properties of the model and make the new form of equations usable in relatively deep water regions.

Consider the case of wave propagation in 1-D horizontal direction with constant depth. The equations then reduce to

$$\eta_t + hu_x + (\eta u)_x + (\alpha + 1/3)h^3u_{xxx} = 0 \qquad (3)$$

$$u_t + g\eta_x + uu_x + \alpha h^2 u_{txx} = 0 \qquad (4)$$

where

$$\alpha = (1/2)\beta^2 + \beta, \quad \beta = z_\alpha/h \qquad (5)$$

Linearizing the system of equations and substituting a trial solution

$$\eta = \eta_0 \exp[i(kx - \omega t)], \quad u = u_0 \exp[i(kx - \omega t)] \qquad (6)$$

leads to the linear dispersion relation

$$\omega^2 = gk^2h\frac{1 - (\alpha + 1/3)(kh)^2}{1 - \alpha(kh)^2} \qquad (7)$$

which varies with the values of α. The standard form of Boussinesq equations corresponds to the choice $\alpha = -1/3$. A value of $\alpha = -4/10$ reduces (7) to the (2,2) Padé approximant of the exact full linear relation, as shown by Witting (1984). Figure 1 shows a comparison between the dispersion relation for full linear theory, and the model dispersion relation for several values of α. In the shallow water limit $kh \to 0$, all of the dispersion relations are asymptotically equivalent. However, in deep water regions where kh increases, the dispersion relation for arbitrary values of α deviates significantly from the linear theory. Using an error minimizing criterion over the range of kh values from 0 to 5, Nwogu (1993) obtains an optimized value of $\alpha = -0.390$ which corresponds to a depth of $z_\alpha = -0.531h$. As shown in Figure 1, the resulting dispersion relation is superior to the standard form of Boussinesq equation in the deep water limit.

NUMERICAL MODEL

The choice of a numerical scheme for equations (1-2) is guided here by two principal factors. First, as occurs in any Boussinesq equation system, finite-differencing of first order derivative terms to second-order accuracy leads to leading order truncation error terms which are of the same form mathematically as the dispersive terms appearing in the model. These

terms are eliminated consistently in the limit as $\Delta x, \Delta y, \Delta t \rightarrow 0$, but usually are large enough in magnitude to interfere with the solution at typical grid resolutions. Most existing schemes for equations of this type (Abbott et al, 1984; Nwogu, 1993) treat these terms by back substitution into the initial second-order accurate scheme, thus incorporating them as intentional distortions to the modelled dispersive effects. In this study, we seek, instead, to reduce all differencing errors to a size that is small relative to all retained terms in the model equations. We therefore adopt a scheme where the spatial differencing in first order terms is done to fourth-order accuracy, leading to a truncation error of $O(\Delta x^4/\mu^2)$ relative to the model dispersive terms at $O(\mu^2)$. In contrast, the dispersive terms themselves are finite-differenced only to second-order accuracy, leading to errors of $O(\Delta x^2)$ relative to the actual dispersive terms. Finally, the system of equations is written in a form that makes the application of a higher-order time-stepping procedure convenient. We utilize a fourth-order Adams predictor-corrector scheme to perform this updating.

The second factor is the impliciteness of the dispersive terms in the momentum equations. In order to address this, we rewrite (1-2) as

$$\eta_t = E(\eta, u, v) \tag{8}$$

$$U_t = F(\eta, u, v) + [F_1(v)]_t \tag{9}$$

$$V_t = G(\eta, u, v) + [G_1(u)]_t \tag{10}$$

where

$$U(u) = u + h\left[b_1 h u_{xx} + b_2 (hu)_{xx}\right] \tag{11}$$

$$V(v) = v + h\left[b_1 h v_{yy} + b_2 (hv)_{yy}\right] \tag{12}$$

are treated as simple variables in the time stepping scheme. The remaining quantities E, F, G, F_1, G_1 are functions of η, u and v which are defined as

$$\begin{aligned} E(\eta, u, v) = & - [(h+\eta)u]_x - [(h+\eta)v]_y \\ & - \left\{a_1 h^3 (u_{xx} + v_{xy}) + a_2 h^2 \left[(hu)_{xx} + (hv)_{xy}\right]\right\}_x \\ & - \left\{a_1 h^3 (v_{yy} + u_{xy}) + a_2 h^2 \left[(hv)_{yy} + (hu)_{xy}\right]\right\}_y \end{aligned} \tag{13}$$

$$F(\eta, u, v) = - g\eta_x - (uu_x + vu_y) \tag{14}$$

$$G(\eta, u, v) = - g\eta_y - (vv_y + uv_x) \tag{15}$$

$$F_1(v) = - h\left[b_1 h v_{xy} + b_2 (hv)_{xy}\right] \tag{16}$$

$$G_1(u) = - h\left[b_1 h u_{xy} + b_2 (hu)_{xy}\right] \tag{17}$$

The constants a_1, a_2, b_1, b_2 are given by

$$a_1 = \beta^2/2 - 1/6, \quad a_2 = \beta + 1/2, \quad b_1 = \beta^2/2, \quad b_2 = \beta \tag{18}$$

For the standard form of the Boussinesq equations, the constants reduce to

$$a_1 = 0, \quad a_2 = 0, \quad b_1 = 1/6, \quad b_2 = -1/2 \tag{19}$$

The governing equations are finite-differenced on an un-staggered grid in x, y, t. We discretize the independent variables as $x = i\Delta x, y = j\Delta y, t = n\Delta t$. Level n refers to

information at the present, known time level. The predictor step is the third-order explicit Adams-Bashforth scheme, given by

$$\eta_{i,j}^{n+1} = \eta_{i,j}^{n} + \frac{\Delta t}{12}\left[23E_{i,j}^{n} - 16E_{i,j}^{n-1} + 5E_{i,j}^{n-2}\right] \tag{20}$$

$$U_{i,j}^{n+1} = U_{i,j}^{n} + \frac{\Delta t}{12}\left[23F_{i,j}^{n} - 16F_{i,j}^{n-1} + 5F_{i,j}^{n-2}\right] + 2F_1^n - 3F_1^{n-1} + F_1^{n-2} \tag{21}$$

$$V_{i,j}^{n+1} = V_{i,j}^{n} + \frac{\Delta t}{12}\left[23G_{i,j}^{n} - 16G_{i,j}^{n-1} + 5G_{i,j}^{n-2}\right] + 2G_1^n - 3G_1^{n-1} + G_1^{n-2} \tag{22}$$

where all information on the right is known from previous calculations. The values of $\eta_{i,j}^{n+1}$ are straightforward to obtain. The evaluation of horizontal velocities at the new time level, however, requires solution of tridiagonal systems which are linear in the unknowns at level $n+1$. Specifically, for a given j, $u_{i,j}^{n+1}(i = 1, 2, ..., M)$ are obtained through tridiagonal matrix solution. Similarly, $v_{i,j}^{n+1}(j = 1, 2, ..., N)$ are solved by a system of tridiagonal matrix equation for given i. The matrices involved are constant in time and may be pre-factored, inverted and stored for use at each time step.

After the predicted values of $\eta_{i,j}^{n+1}, u_{i,j}^{n+1}$ and $v_{i,j}^{n+1}$ are evaluated, we obtain the corresponding spatial derivatives $E_{i,j}^{n+1}, F_{i,j}^{n+1}, G_{i,j}^{n+1}, (F_1)_{i,j}^{n+1}, (G_1)_{i,j}^{n+1}$ from equations (14-18). Then the fourth-order Adams-Moulton corrector scheme is applied

$$\eta_{i,j}^{n+1} = \eta_{i,j}^{n} + \frac{\Delta t}{24}\left[9E_{i,j}^{n+1} + 19E_{i,j}^{n} - 5E_{i,j}^{n-1} + E_{i,j}^{n-2}\right] \tag{23}$$

$$U_{i,j}^{n+1} = U_{i,j}^{n} + \frac{\Delta t}{24}\left[9F_{i,j}^{n+1} + 19F_{i,j}^{n} - 5F_{i,j}^{n-1} + F_{i,j}^{n-2}\right] + F_1^{n+1} - F_1^{n} \tag{24}$$

$$V_{i,j}^{n+1} = V_{i,j}^{n} + \frac{\Delta t}{24}\left[9G_{i,j}^{n+1} + 19G_{i,j}^{n} - 5G_{i,j}^{n-1} + G_{i,j}^{n-2}\right] + G_1^{n+1} - G_1^{n} \tag{25}$$

The corrector step is iterated until the error between two successive results reaches a required limit. The error is computed for each of the three dependent variables η, u, v and is defined as

$$\Delta f = \frac{\sum_{i,j} |f_{i,j}^{n+1} - f_{i,j}^{(n+1)*}|}{\sum_{i,j} |f_{i,j}^{n+1}|} \tag{26}$$

where f denotes any of the variables and $()^*$ denotes the previous estimate. The corrector step is iterated if any of the Δf's exceeds 0.001. The scheme typically requires no iteration unless problems arise at boundaries. Then the same procedure is applied to the next time step.

CASE STUDIES

Random waves shoaling on a slope

For the 1-D version of the numerical model, we study random wave propagation over a slope and compare numerical results with the laboratory data of Mase and Kirby (1992). The experimental layout consists of a constant depth of $0.47m$ and a constant slope (1:20).

Two sets of random waves with peak frequencies of $0.6Hz$ (run1) and $1.0Hz$ (run2) were generated by the wavemaker on the end of the constant depth. The target incident spectrum was a Pierson-Moskowitz spectrum. Wave gauges at depths $h = 47$ (two gages), $35, 30, 25, 20, 17.5, 15, 12.5, 10, 7.5, 5$ and $2.5\,cm$ collected time series of surface elevation. Further details of the experimental setup may be found in Mase and Kirby (1992).

The incident boundary for the numerical model was taken to be the location of the first wave gauge $2\,m$ seaward of the toe of the beach slope (at a depth of $47cm$) where experimental data is available. The horizontal velocity $u(t)$ at the incident boundary was derived from the surface elevation data $\eta(t)$ through Fourier analysis, based on linear relation between u and η. The present model does not include wave breaking, which occurs in the larger waves near the gage at the depth of $17.5\,cm$. We thus end the beach slope at a point shoreward of the gage at $h = 17.5\,cm$ and introduce a flat bottom. The sponge layer method is used to absorb the waves propagating past the last gage.

Comparisons of the model and experimental data for the first 60 seconds run2 are shown in Figure 2, where the results are shown for the initial conditions (bottom trace) and for gage positions $35, 30, 25, 20$ and $17.5\,cm$ going up the plot. We see that the model reproduces the measured wave form (both wave height and wave phase) quite well. For this case, the value of kh for the peak wave frequency is about 2.0 at the incident wave boundary, and thus this case represents a severe test of the applicability of the model to deeper water conditions. As a comparison, we ran a model based on the standard Boussinesq equations for the case of run2, and show the results in Figure 3. The severe discrepancies between modelled and measured waves indicate that the standard Boussinesq model is not capable of handling the range of depths used in this example.

Waves evolution in a closed rectangular basin

Compared to the 1-D model, the 2-D model involves a number of mixed x and y derivative terms, which are handled differently in the time-stepping scheme than terms containing derivatives in one direction only. In order to verify the correctness of the model and to test its stability and associated boundary conditions in 2-D, we use the model to study wave evolution in a closed basin, where linear analytical solution exists.

Consider a rectangular domain $0 \leq x \leq L_x, 0 \leq y \leq L_y$ bounded by reflective vertical walls. Assuming the initial condition to be a superelevation of the surface $\eta_0(x, y)$ above an otherwise constant depth $h_0 = 0.45m$, the linear analytic solution can be found to be

$$\eta(x, y, t) = \sum_{n=0}^{\infty} \sum_{m=0}^{\infty} \tilde{\eta}_{nm} \cos(\omega_{nm} t) \cos(\frac{n\pi x}{L_x}) \cos(\frac{m\pi y}{L_x}) \tag{27}$$

where $\tilde{\eta}_{nm}$ and ω_{nm} are the Fourier coefficient and the natural frequency corresponding to mode (n, m) and can be determined from the inital and boundary conditions. For the runs shown here, the initial surface elevation is of Gaussian shape:

$$\eta_0(x, y) = H_0 \exp\{-2[(x - 3.75)^2 + (y - 3.75)^2]\} \tag{28}$$

where x and y are defined with the origin in the left and bottom corner of the basin. The initial superelevation is symmetric about the center ($x = 3.75m$, $y = 3.75m$).

To examine the symmetry and conservation properties of the solution, an initial maximum elevation H_0 of $0.045m$ (with a corresponding height-to-depth ratio of 0.1) is used. The model was run for $100s$, using a grid size of $\Delta x = 0.15m$ and time step of $\Delta t = 0.05s$. Results from the model show that the surface elevation is symmetric and the total water volume is conserved (less than one percent error).

To compare the agreement between the linearized model and the linear solution, and to show the effects of large initial nonlinearity on the computed solution, we take an initial maximum $H_0 = 0.45\,m$. Figure 4 shows a comparison of nonlinear (dash-dot line), linear numerical (dashed line) and linear analytical (solid line) results for the first 25 seconds after the release of the elevation. The effect of nonlinearity is apparent through the more rapid arrival of the initial pulse at the corner point, the progressive increase in phase lead of the nonlinear crests, and in the apparent steepening of the individual nonlinear wave crests. (See, in particular, the corner point near $t = 10 - 15s$). There is also an apparent, but slight, discrepancy between the two linear solutions. This discrepancy shows up as an occasional modification of the shape of an individual wave crest or trough, rather than as a modification or relative drift in the overall solution. Further analysis show that the discrepancy is due to the effect of errors in the higher frequency portion of the solution, which contributes relatively little variance to the overall surface record.

CONCLUSION

A high order numerical scheme has been developed for a new form of the Boussinesq equations derived by Nwogu (1993). The scheme has been tested in a number of examples which illustrate its basic stability and which show that the new Boussinesq equations may be applied to a wide range of water depths.

Like other Boussinesq approximations, Nwogu's new Boussinesq equations is limited to the lowest order of nonlinearity. To account for $O(1)$ nonlinearity of waves near breaking or the dominant cubic nonlinearity of intermediate depth waves, we are presently extending the model equations described here to include higher order terms; results for this extension of the model capability will be described separately (Kirby and Wei, 1994).

Acknowledgement

This research was supported by the Army Research Office through University Research Initiative grant DAAL 03-92-G-0116.

REFERENCES

Abbott, M. B., McCowan, A. D. and Warren, I. R., 1984, "Accuracy of short-wave numerical model", *J. Hydr. Engnrg.*, **110**, 1287-1301.

Elgar, S. and Guza, R. T., 1985, "Shoaling gravity waves: comparisons between field observations, linear theory and a nonlinear model", *J. Fluid Mech.*, **158**, 47-70.

Elgar, S. and Guza, R. T., 1986, "Nonlinear model predictions of bispectra of shoaling surface gravity waves", *J. Fluid Mech.*, **167**, 1-18.

Elgar, S., Freilich, M. H. and Guza, R. T., 1990, "Model-data comparisons of moments of nonbreaking shoaling surface gravity waves", *J. Geophys. Res.*, **95**(C9), 16055-16063.

Freilich, M. H., and Guza, R. T., 1984, "Nonlinear effects on shoaling surface gravity waves", *Philos. Trans. R. Soc. London, Ser. A*, **311**, 1-41.

Freilich, M. H., Guza, R. T., and Elgar, S. L., 1993, "Field test of two-dimensional Boussinesq shoaling wave model", *MEET'N'93- First Joint ASCE/ASME/SES MEETING*, Eds: C.T. Herakovich and J.M. Duva, Charlottesville, VA, USA (abstract only).

Goring, D. G., 1978, "Tsunamis-the propagation of long waves onto a shelf". Ph.D dissertation, California Institute fo Technology, Pasadena, California.

Hammack, J. L., Scheffner, N. W., and Segur, H., 1990, personal communication.

Kirby, J. T., 1990, "Modelling shoaling directional wave spectra in shallow water", *Proc. of 22nd Int. Conf. Coastal Engr.*, Delft, 109-121.

Kirby, J. T. and Wei, G., 1994, "Derivation and properties of a fully nonlinear, extended Boussinesq model", this conference.

Liu P. L-F., Yoon, S. B. and Kirby, J. T., 1985, "Nonlinear refraction-diffraction of waves in shallow water", *J. Fluid Mech.*, **153**, 185-201.

Madsen, P. A., Murray, R. and Sørensen, O.R., 1991, "A new form of Boussinesq equations with improved linear dispersion characteristics", *Coastal Engng*, **15**, 371-388.

Mase, H. and Kirby, J. T., 1992, "Hybrid frequency-domain KdV equation for random wave transformation", *Proc. 23rd Int. Conf. Coastal Engr.*, Venice, Oct. 1992.

Murray, R. J., 1989, "Short wave modelling using new equations of Boussinesq type", *Proc. 9th Australasian Conference on Coastal and Ocean Engineering*, Adelaide, Australia, 331-336.

Nwogu, O., 1993, "An alternative form of the Boussinesq equations for nearshore wave propagation", *J. Waterway, Port, Coast. Ocean Engng*, **119**(6), 618-638.

Peregrine, D. H., 1967, "Long waves on a beach", *J. Fluid Mech.*, **27**, 815-82.

Rygg, O. B., 1988, "Nonlinear refraction-diffraction of surface waves in intermediate and shallow water", *Coastal Engng*, **12**, 191-211.

Whalin, R. W., 1971, "The limit of applicability of linear wave refraction theory in a convergence zone", Res. Rept. H-71-3, Hydraulics Laboratory, U. S. Army Corps of Engineers Waterways Experiment Station, Vicksburg.

Witting, J. M., 1984, "A unified model for the evolution of nonlinear water waves", *J. Comp. Phys.*, **56**, 203-239.

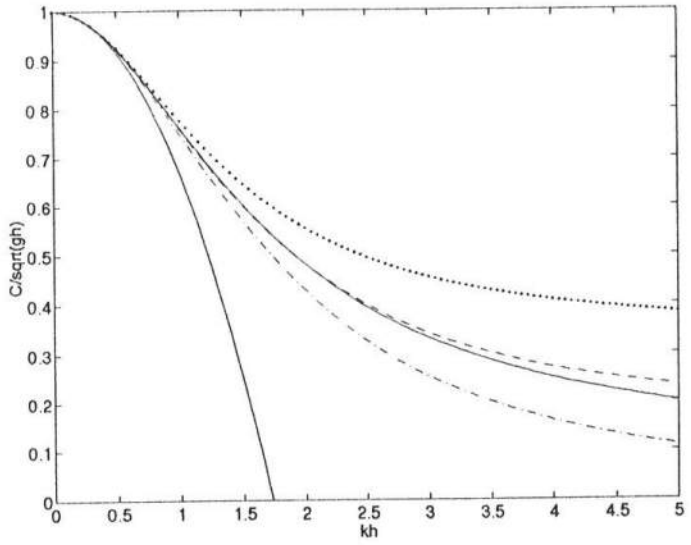

Figure 1: Comparison of dispersion relation for different values of α with linear theory: linear theory (——); $\alpha = -0.390$ (- - -); α=-0.400 ($\cdots$); α=-1/3 (- $\cdots$ -); α =0 (——).

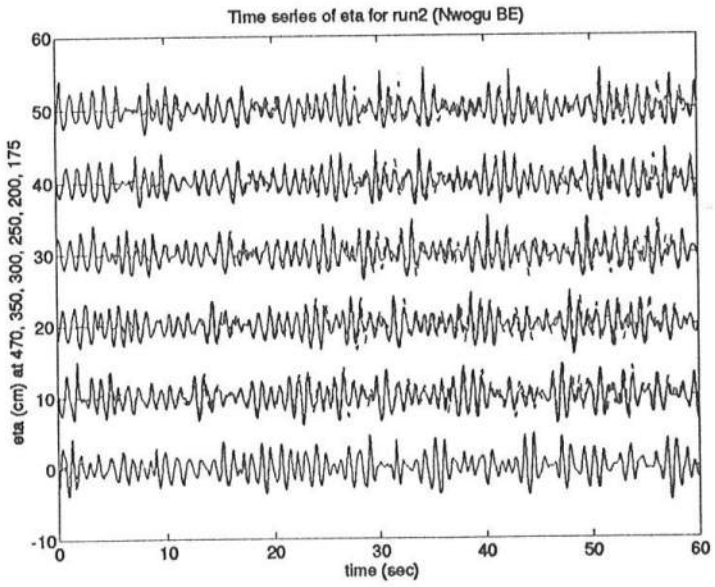

Figure 2: Comparison of time series of surface elevation for run2: model (- - -); data (——)

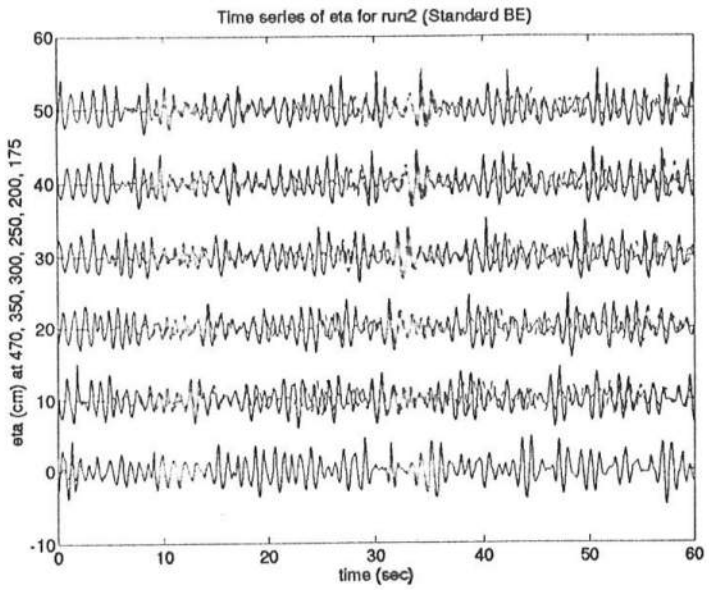

Figure 3: Comparison of time series of surface elevation for run2 using standard Boussinesq equations: model (- - -); data (——)

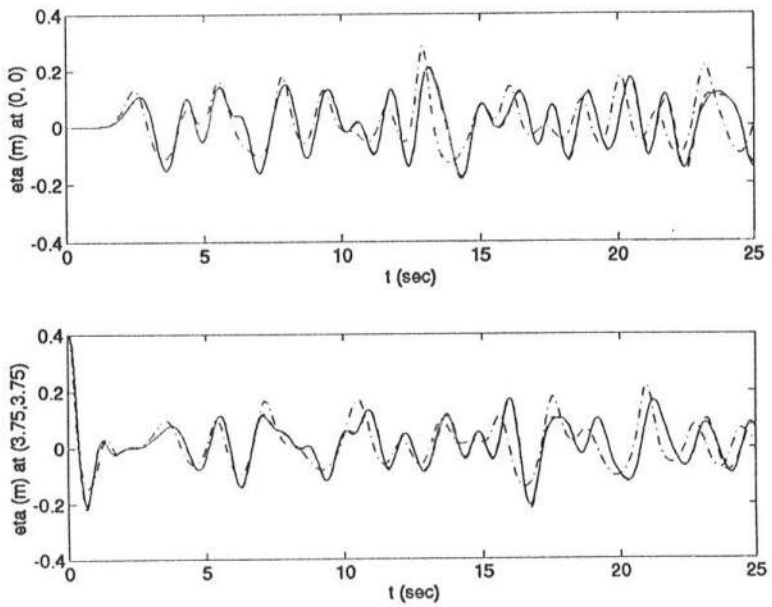

Figure 4: Comparison of solutions for initial Gaussian elevation in square box. Nonlinear (dash-dot line), linear numerical (dashed line) and linear analytical (solid line) solutions.

PARABOLIC AND ANGULAR SPECTRUM MODELLING OF A FULLY NONLINEAR EXTENDED BOUSSINESQ EQUATION

James M. Kaihatu and James T. Kirby
Center for Applied Coastal Research, Department of Civil Engineering,
University of Delaware, Newark, DE 19716

ABSTRACT

In this study we formulate two frequency domain models of a fully nonlinear extended Boussinesq equation (Kirby and Wei, 1994). Because we use triad interactions between frequency components to treat the nonlinear terms, we must truncate the equations to $O(\delta\mu^2)$, where δ is the nonlinearity parameter and μ the dispersion parameter. This truncation still retains dispersion in the nonlinear terms, which Kirby and Wei (1994) show is important for proper energy transfer in the deep water limit. The first model, a small-angle parabolic representation of these equations, is developed and compared to the experimental data of Whalin (1971). It agrees well with the data and performs better than the Kadomtsev-Petviashvili (KP) model of Liu, *et al.* (1985) which has nondispersive Green's Law shoaling. We then formulate an angular spectrum version of these equations, in which we assume longshore periodicity as well as time periodicity, and couple both frequency and longshore wavenumber modes via triad interactions.

INTRODUCTION

For problems of nonlinear wave propagation, models of the standard Boussinesq equations of Peregrine (1967) do well in their regions of validity ($kh \ll 1$, where k is the wavenumber and h the water depth). Numerous examples of these models appear in the literature, either in time domain (e.g., Rygg 1988), or frequency domain (Freilich and Guza 1984; Liu, *et al.* 1985; Kirby 1990) formats. Unfortunately, errors in the prediction of wave celerity and shoaling become evident in intermediate or deep water, primarily due to the inadequacy of the linear dispersion relation and the shoaling mechanisms inherent in these standard

Boussinesq equation models. If we look specifically at the "consistent model" of Freilich and Guza (1984), we see that the shoaling mechanism is Green's Law:

$$\left(\frac{a}{a_0}\right) = \left(\frac{h}{h_0}\right)^{\frac{1}{4}} \tag{1}$$

which is a monotonic increase in wave amplitude a with a decrease in depth. Other standard Boussinesq models may have at most an $O((kh)^2)$ correction to this relation, insufficient for intermediate or deep water.

Recently there have been several attempts to overcome this limitation while still working within the Boussinesq format. Witting (1984) formulated a one-dimensional Boussinesq-type equation for constant depth; it had a linear dispersion relation in the form of a rational polynomial with a free parameter. This free parameter was tuned to match the dispersion relation from linear theory from shallow to deep water. Madsen, et al. (1991) and Nwogu (1993) formulated two-dimensional Boussinesq models with similar dispersion relations. Madsen and Sørensen (1993) and Chen and Liu (1993) have developed frequency domain versions of Madsen, et al. (1991) and Nwogu (1993), respectively. All show improved dispersion characteristics in deeper water than the standard Boussinesq equation is valid for.

One probable criticism of many of these models is the order of truncation. They are truncated to $O(\delta, \mu^2)$, where $\delta(= a/h)$ is the nonlinearity parameter and $\mu(= kh)$ the dispersion parameter. This discounts any dispersion effects in the nonlinear terms, which may affect (for example) the accuracy of nonlinear energy transfer at the deep water limit. Kirby and Wei (1994) extended Nwogu's formulation to a fully nonlinear extended Boussinesq equation by assuming $\delta = O(1)$. They showed that these equations gave transfer functions for a random second-order sea which agree exactly with those of Stokes theory save for the differences in calculating wavenumbers. In this study we use these fully nonlinear equations in the frequency domain.

FREQUENCY DOMAIN FORMULATION

The derivation of the fully nonlinear extended Boussinesq equations can be found in Kirby and Wei (1994). We wish to make use of triad interactions in the frequency domain while retaining dispersive effects in the nonlinear terms; thus we need to truncate the system to $O(\delta\mu^2)$. These truncated equations of continuity and momentum are, respectively:

$$\eta_t + \nabla\cdot((h+\eta)\nabla\phi_\alpha) + \nabla\cdot[(h+\eta)\nabla(z_\alpha\nabla\cdot(h\nabla\phi_\alpha))] + (h+\eta)\nabla\left(\frac{z_\alpha^2}{2}\nabla^2\phi_\alpha\right)$$
$$+\nabla\cdot\left(\frac{1}{2}h^2\nabla(\nabla\cdot(h\nabla\phi_\alpha))\right) - \nabla\cdot\left(\frac{1}{6}h^3\nabla(\nabla^2\phi_\alpha)\right) = O(\delta^2\mu^2, \delta^3\mu^2, \mu^4) \tag{2}$$

$$\phi_{\alpha t} + g\eta + \left[(z_\alpha - \eta)\nabla\cdot(h\nabla\phi_{\alpha t}) + \frac{1}{2}z_\alpha^2\nabla^2\phi_{\alpha t}\right] + \frac{1}{2}(\nabla\phi_\alpha)^2$$
$$+\nabla\phi_\alpha\cdot(\nabla z_\alpha\nabla\cdot(h\nabla\phi_\alpha)) + \nabla\phi_\alpha\cdot(z_\alpha\nabla(\nabla\cdot(h\nabla\phi_\alpha)) \quad (3)$$
$$+\nabla\phi_\alpha\cdot(z_\alpha\nabla z_\alpha\nabla^2\phi_\alpha) + \frac{1}{2}\nabla\phi_\alpha\cdot z_\alpha^2\nabla(\nabla^2\phi_\alpha) + \frac{1}{2}(\nabla\cdot(h\nabla\phi_\alpha))^2 = O(\delta^2\mu^2, \delta^3\mu^2, \mu^4)$$

where η is the free surface elevation, ϕ_α is the velocity potential at an arbitrary elevation z_α in the water column, ∇ is the differential operator in the two horizontal dimensions (x, y), and α is a nondimensional parameter related to z_α by:

$$\alpha = \left(\frac{z_\alpha^2}{2h^2} + \frac{z_\alpha}{h}\right) \quad (4)$$

Neglecting dispersive effects in the nonlinear terms in (2) and (3) recovers the equations of Chen and Liu (1993).

The linear dispersion relation associated with (2) and (3) is:

$$C^2 = gh\left(\frac{1-(\alpha+\frac{1}{3})(kh)^2}{1-\alpha(kh)^2}\right) \quad (5)$$

and the group velocity is:

$$C_g = \frac{\partial\omega}{\partial k} = C\left[1 - \frac{(kh)^2}{3}\left(\frac{1}{(1-\alpha(kh)^2)\left(1-\left(\alpha+\frac{1}{3}\right)(kh)^2\right)}\right)\right] \quad (6)$$

Nwogu (1993) used a least-squares technique to fit (5) to the dispersion relation from linear theory in the range $0 \leq \frac{h}{L_o} \leq 0.5$, where L_o is the deep water wavelength. He found the optimal value of α to be -0.390, yielding a z_α of $-0.53h$. Chen and Liu (1993) performed a least-squares best fit of both (5) and (6), yielding a refined value of $\alpha = -0.3855$ with the corresponding $z_\alpha = -0.522h$. We use this refined α in our study. The reader is referred to Nwogu (1993) and Chen and Liu (1993) for further details on how well (5) and (6) match full linear theory.

In order to transform the equations to the frequency domain, it is necessary to assume periodicity in time for both η and ϕ_α:

$$\eta = \sum_{n=1}^{\infty}\frac{\hat{\eta}_n}{2}e^{-in\omega t} + c.c. \quad (7)$$

$$\phi_\alpha = \sum_{n=1}^{\infty}\frac{\hat{\phi}_{\alpha n}}{2}e^{-in\omega t} + c.c. \quad (8)$$

and use triad resonant interactions between the frequency components to treat the nonlinear terms. We then use the resulting time-periodic momentum equation to relate $\hat{\phi}_{\alpha n}$ to $\hat{\eta}_n$ and substitute this into the time-periodic continuity equation to eliminate $\hat{\eta}_n$. This will give us a single time-periodic evolution equation for $\hat{\phi}_{\alpha n}$. We can then use the time-periodic momentum equation to find $\hat{\eta}_n$. These equations are not written out here.

PARABOLIC MODEL

We wish to formulate a series of parabolic evolution equations for the amplitudes of $\hat{\phi}_{\alpha n}$ and $\hat{\eta}_n$, one for each frequency component, which are then coupled by the triad resonant interactions used for the nonlinear terms. We assume the following form for $\hat{\phi}_{\alpha n}$ and $\hat{\eta}_n$:

$$\hat{\phi}_{\alpha n} = A_n(x,y)e^{i\int k_n(x,y)dx} \tag{9}$$

$$\hat{\eta}_n = B_n(x,y)e^{i\int k_n(x,y)dx} \tag{10}$$

where A_n and B_n are slowly-varying functions of x. Substituting these expressions into the time-periodic equations, making use of the parabolic approximation:

$$A_{nxx} \ll 2iA_{nx} \tag{11}$$

and using a reference phase function (Kirby and Dalrymple 1983) to factor out the y-dependent part of the phase function:

$$A_n = a_n e^{i(\int \overline{k}_{no}(x)dx - \int k_n(x,y)dx)} \tag{12}$$

$$B_n = b_n e^{i(\int \overline{k}_{no}(x)dx - \int k_n(x,y)dx)} \tag{13}$$

(where $\overline{k}_{no}$ is a y-averaged wavenumber) yields:

$$\begin{aligned} &\left(\zeta_n + -2\left[\alpha + \frac{1}{3}\right]k_n^2h^3\right)a_{nyy} + \left(1 + \frac{n^2\omega^2 z_\alpha}{g} - \tau_n k_n^2 h^2\right)h_y a_{ny} \\ &+2ik_n\left(\zeta_n - 2k_n^2h^3\left[\alpha+\frac{1}{3}\right]\right)a_{nx} - 2\left(k_n\zeta_n - 2\left[\alpha+\frac{1}{3}\right]k_n^3h^3\right)(\overline{k}_{no}-k_n)a_n \\ &+i(k_n\zeta_n - \tau_n k_n^3h^2)h_x a_n + i\left(\zeta_n - 6\left[\alpha+\frac{1}{3}\right]\right)k_{nx}a_n \\ &-\frac{i\omega}{4g}\left(\sum_{l=1}^{n-1} Ra_l a_{n-l}e^{i\int(\overline{k}_{lo}+\overline{k}_{n-lo}-\overline{k}_{no})dx} + 2\sum_{l=1}^{N-n} Sa_l^* a_{n+l}e^{i\int(\overline{k}_{n+lo}-\overline{k}_{lo}-\overline{k}_{no})dx}\right) = 0 \end{aligned} \tag{14}$$

where

$$\zeta_n = h + \frac{n^2\omega^2h^2\alpha}{g} \tag{15}$$

$$\tau_n = 1 + 5\alpha + \sqrt{1+2\alpha} \tag{16}$$

$$\begin{aligned} R = (n-l)k_l^2 + 2nk_lk_{n-l} + lk_{n-l}^2 - \\ \alpha h^2[(n-l)k_l^4 + 2nk_l^3k_{n-l} + nk_l^2k_{n-l}^2 + 2nk_lk_{n-l}^3 + lk_{n-l}^4] \\ -nh^2\frac{(n-l)^2 + l(n-l) + l^2}{l(n-l)}k_l^2k_{n-l}^2 \end{aligned} \tag{17}$$

$$S = (n+l)k_l^2 - 2nk_lk_{n+l} - lk_{n+l}^2 - \alpha h^2[(n+l)k_l^4 - 2nk_l^3k_{n+l} + nk_l^2k_{n+l}^2 - 2nk_lk_{n+l}^3 - lk_{n_l}^4] + nh^2\frac{(n+l)^2 - l(n+l) + l^2}{l(n+l)}k_l^2k_{n+l}^2 \tag{18}$$

and the asterisk denotes the complex conjugate. From the a_n we can calculate the b_n (the amplitudes of the free surface elevation) from:

$$b_n = \frac{in\omega}{g}\alpha h^2 a_{nyy} + \frac{in\omega z_\alpha}{g}h_y a_{ny} - \frac{2n\omega\alpha h^2 k_n}{g}a_{nx} - \frac{2in\omega\alpha h^2 k_n}{g}(\bar{k}_{no} - k_n)a_n - \frac{n\omega z_\alpha k_n}{g}h_x a_n - \frac{n\omega\alpha h^2}{g}k_{nx}a_n + \frac{in\omega}{g}(1 - \alpha k_n^2 h^2)a_n + \frac{1}{4g}\left(\sum_{l=1}^{n-1} R' a_l a_{n-l} e^{i\int(\bar{k}_{lo}+\bar{k}_{n-lo}-\bar{k}_{no})dx} - 2\sum_{l=1}^{N-n} S' a_l^* a_{n+l} e^{i\int(\bar{k}_{n+lo}-\bar{k}_{lo}-\bar{k}_{no})dx}\right) \tag{19}$$

where:

$$R' = k_l k_{n-l} - \alpha h^2\left(k_l k_{n-l}^3 + k_l^3 k_{n-l}\right) - h^2\frac{(n-l)^2 + l(n-l) + l^2}{l(n-l)}k_l^2 k_{n-l}^2 \tag{20}$$

$$S' = k_l k_{n+l} - \alpha h^2\left(k_l k_{n+l}^3 + k_l^3 k_{n+l}\right) - h^2\frac{(n+l)^2 - l(n+l) + l^2}{l(n+l)}k_l^2 k_{n+l}^2 \tag{21}$$

The linear terms of (14) and (19) are essentially identical to Chen and Liu (1993) with slight differences due to the choice of a y-averaged wavenumber in the reference phase function. We use the Crank-Nicholson method to discretize the equations, employing iteration to center the nonlinear terms.

COMPARISON TO EXPERIMENT OF WHALIN (1971)

Whalin (1971) conducted a series of experiments to investigate harmonic generation and the limits of linear refraction theory. He ran initially sinusoidal waves over a topographical lens and measured the amplitudes of the first three harmonics at various locations down the centerline of the tank. The reader is referred to Whalin (1971) for the details of the experiments.

We will restrict ourselves to the 2 second experimental case; this gives a kh value of 0.73 for the fundamental harmonic, which may test the limits of standard Boussinesq theory. The three initial wave amplitudes for this wave period are $a_o = 0.75cm$, $1.06cm$ and $1.49cm$. We compare the resulting free surface amplitudes of the present parabolic model, the parabolic model of Chen and Liu (1993) and the parabolic Kadomtsev-Petviashvili (KP) model of Liu, *et al.* (1985) to Whalin's data. The KP model is a weakly two-dimensional form of the standard Boussinesq equations and has Green's Law shoaling; thus we expect it to compare

relatively poorly to the other two models. We only show comparisons for $a_o = 0.75cm$ and $a_o = 1.49cm$; the case $a_o = 1.06cm$ shows similar agreement to data. Figures 1 and 2 show the comparisons to Whalin's data. We see that, while the present parabolic model and the model of Chen and Liu (1993) compare reasonably well to the data, the KP model overshoals the fundamental and second harmonic for both cases. In the case of the third harmonic, it can be seen that neither model compares especially well to the data. This may be due to the fact that $\frac{h}{L_o} = 0.66$ in the deep portion of the tank for this harmonic, which is well beyond the limit of validity for Green's Law shoaling and also beyond the calibration range for (5) and (6). Generally, it can be seen that the present model compares to data as well or better than the Chen and Liu (1993) model. This is particularly evident in the second harmonic. The added dispersiveness in the nonlinear shoaling process can be seen in the second and third harmonics, as the present model does not shoal as fast as the model of Chen and Liu (1993).

ANGULAR SPECTRUM MODEL

The parabolic model of the previous section performs well in situations where the angle of incidence is small. In instances where this is not the case, however, the parabolic approximation breaks down rapidly. Angular spectrum modelling (e.g., Kirby 1990) involves no assumption about angle of approach, and so is theoretically valid for any angle of incidence.

The essential assumption in the angular spectrum approach is periodicity in the longshore (y) direction. We thus assume the following forms for η and ϕ_α in (2) and (3):

$$\phi_\alpha = \sum_{m=-M}^{M} \sum_{n=1}^{N} \frac{A_n^m(x)}{2} e^{i(\int k_n \tilde{\gamma}_n^m dx + m\lambda y - n\omega t)} + c.c. \tag{22}$$

$$\eta = \sum_{m=-M}^{M} \sum_{n=1}^{N} \frac{B_n^m(x)}{2} e^{i(\int k_n \tilde{\gamma}_n^m dx + m\lambda y - n\omega t)} + c.c. \tag{23}$$

where the longshore wavenumber λ is

$$\lambda = k \sin\theta \tag{24}$$

and

$$\tilde{\gamma}_n^m = (1 - (\frac{m\lambda}{k_n})^2)^{1/2} = \cos\theta \tag{25}$$

and use triad interactions for the λ modes as well as the frequency modes in the nonlinear terms. This yields:

$$\begin{aligned} 2ik_n\tilde{\gamma}_n^m \left(\zeta_n - 2k_n\tilde{\gamma}_n^m h^3(\alpha + \frac{1}{3})\xi_n^m\right) A_{nx}^m + ik_n\tilde{\gamma}_n^m \left(1 + \frac{n^2\omega^2 z_\alpha}{g} - h^2\tau_n\xi_n^m\right) h_x A_n^m \\ + i\left(\zeta_n - 6k_n^2\tilde{\gamma}_n^{m2}(\alpha + \frac{1}{3})h^3 - 2m^2\lambda^2(\alpha + \frac{1}{3})h^3\right)(k_n\tilde{\gamma}_n^m)_x A_n^m \\ - \frac{i\omega}{4g}\left(\sum_{l=1}^{n-1}\sum_{p=-M}^{M} IA_l^p A_{n-l}^{m-p} e^{i\Theta} + 2\sum_{l=1}^{N-n}\sum_{p=-M}^{M} JA_l^{p*} A_{n+l}^{m+p} e^{i\Upsilon}\right) = 0 \end{aligned} \tag{26}$$

and

$$B_n^m = \frac{in\omega}{g}\left(1-\alpha h^2\xi_n^m\right)A_n^m - \frac{n\omega z_\alpha k_n\tilde{\gamma}_n^m}{g}h_x A_n^m - \frac{n\omega\alpha h^2}{g}(k_n\tilde{\gamma}_n^m)_x A_n^m \quad (27)$$
$$-\frac{2n\omega\alpha h^2 k_n\tilde{\gamma}_n^m}{g}A_{nx}^m + \frac{1}{4g}\left(\sum_{l=1}^{n-1}\sum_{p=-M}^{M} I' A_l^p A_{n-l}^{m-p} e^{i\Theta} - 2\sum_{l=1}^{N-n}\sum_{p=-M}^{M} J' A_l^{p*} A_{n+l}^{m+p} e^{i\Upsilon}\right)$$

where

$$\Theta = \int (k_l\tilde{\gamma}_l^p + k_{n-l}\tilde{\gamma}_{n-l}^{m-p} - k_n\tilde{\gamma}_n^m)dx \quad (28)$$

$$\Upsilon = \int (k_{n+l}\tilde{\gamma}_{n+l}^{m+p} - k_l\tilde{\gamma}_l^p - k_n\tilde{\gamma}_n^m)dx \quad (29)$$

$$\xi_n^m = (k_n^2\tilde{\gamma}_n^{m2} + m^2\lambda^2) \quad (30)$$

and I,J,I' and J' are complicated interaction coefficients. (ζ_n and τ_n were defined in the previous section.) Given $2M+1$ longshore wavenumber modes and N frequency modes, we model $(2M+1)\times N$ ordinary differential equations. We will employ a second-order Euler differencing scheme with iteration for the nonlinear term, and intend to show model-data comparisons during the conference presentation.

CONCLUSIONS

In this paper we transformed the fully nonlinear extended Boussinesq equations of Kirby and Wei (1994) in the frequency domain. First we truncate the system to $O(\delta\mu^2)$ so that triad resonant interaction can be utilized while still maintaining dispersion in the nonlinear terms. Then we developed a set of small-angle parabolic evolution equations for the amplitudes of the velocity potential ϕ_α and the free surface η. The model compares well to data. We then employed the additional assumption of longshore periodicity and derived the angular spectrum version of the governing equations. This model overcomes the small angle restriction of the parabolic model. Future work will consist of the application of this angular spectrum model to simulate experimental cases. We also intend to use the model to investigate certain physical processes in wavefield evolution, such as directional interaction.

ACKNOWLEDGEMENTS

This work was supported by a National Science and Engineering Graduate Fellowship from the Office of Naval Research (JMK) and by University Research Initiative Grant No. DAAL-03-92-G0116 from the Army Research Office (JTK).

REFERENCES

Chen, Y., and Liu, P. L-F. 1993. Modified Boussinesq equations and associated parabolic models for wave propagation. Center for Applied Coastal Engineering, University of Delaware, Research Report CACR-93-06, Newark, DE.

Freilich, M.H., and Guza, R.T. 1984. Nonlinear effects on shoaling surface gravity waves. *Philosophical Transactions of the Royal Society of London*, A311, pp. 1-41.

Kirby, J.T. 1990. Modelling shoaling directional wave spectra in shallow water. *Proceedings of the 22nd International Conference on Coastal Engineering*, Delft, Vol. 1, pp. 109-121.

Kirby, J.T., and Dalrymple, R.A. 1983. A parabolic equation method for the combined refraction-diffraction of Stokes waves by mildly-varying topography. *Journal of Fluid Mechanics*. Vol. 136, pp. 453-466.

Kirby, J.T., and Wei, G. 1994. Derivation and properties of a fully-nonlinear, extended Boussinesq model. *International Symposium on Waves - Physical and Numerical Modelling*, Vancouver (to appear).

Liu, P. L-F., Yoon, S.B., and Kirby, J.T. 1985. Nonlinear refraction-diffraction of waves in shallow water. *Journal of Fluid Mechanics*, Vol. 153, pp. 185-201.

Madsen, P.A., Murray, R., and Sørensen, O.R. 1991. A new form of the Boussinesq equations with improved linear dispersion characteristics. *Coastal Engineering*, Vol. 15, pp. 371-388.

Madsen, P.A., and Sørensen, O.R. 1993. Bound waves and triad interactions in shallow water. *Ocean Engineering*, Vol. 20, no. 4, pp. 359-388.

Nwogu, O. 1993. Alternative form of Boussinesq equations for nearshore wave propagation. *Journal of Waterway, Port, Coastal, and Ocean Engineering*, ASCE, Vol. 119, no. 6, pp. 618-638.

Peregrine, D.H. 1967. Long waves on a beach. *Journal of Fluid Mechanics*, Vol. 27, pp. 815-827.

Rygg, O.B. 1988. Nonlinear refraction-diffraction of surface waves in intermediate and shallow water. *Coastal Engineering*, Vol. 12, pp. 191-211.

Whalin, R.W. 1971. The limit of application of linear wave refraction theory in a convergence zone. U.S. Army Engineer Waterways Experiment Station, Research Report H-71-3, Vicksburg, MS.

Witting, J.M. 1984. A unified model for the evolution of nonlinear water waves. *Journal of Computational Physics*, Vol. 56, pp. 203-236.

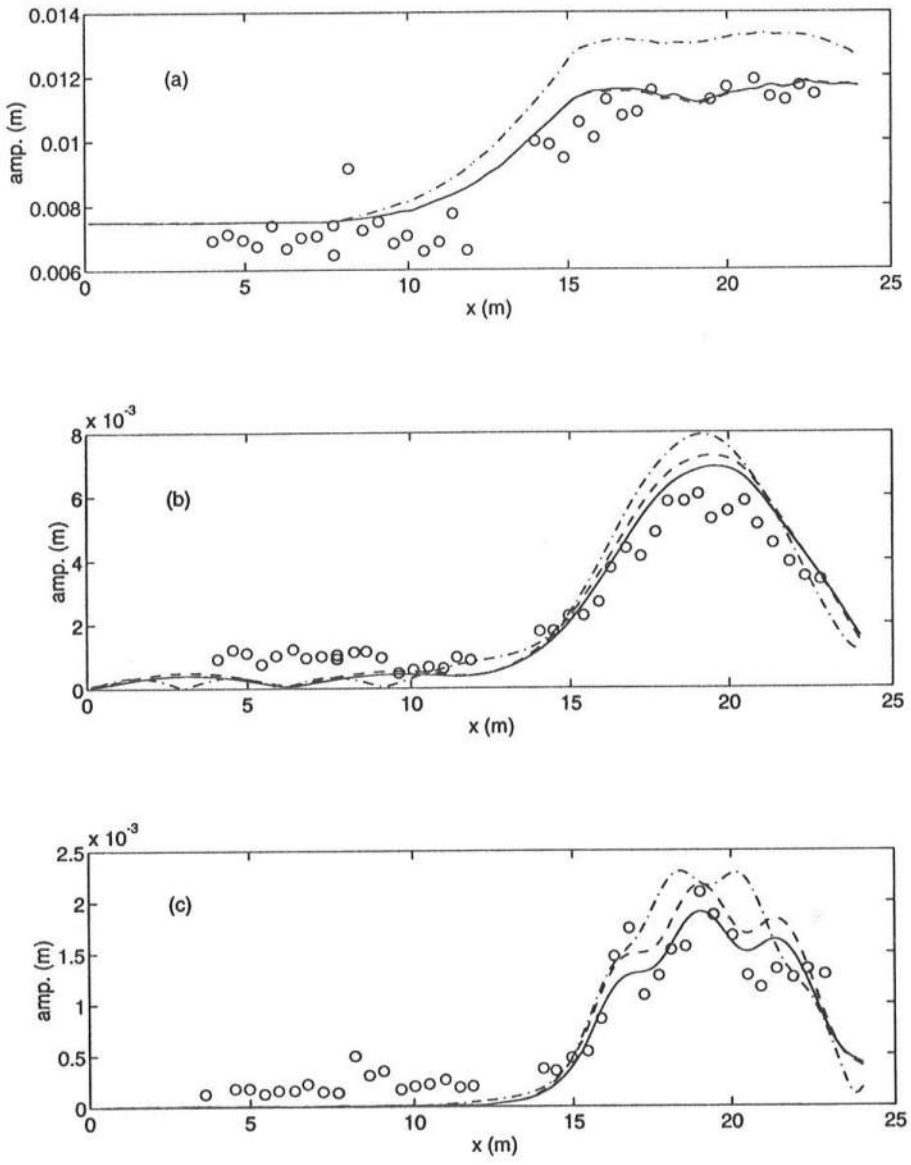

Figure 1: Comparison to Whalin (1971) with $a_o = 0.75cm$. Data (o) vs. present model (—), model of Chen and Liu (1993) (- - -), model of Liu, et al. (1985) (-.-): (a) first harmonic; (b) second harmonic; (c) third harmonic.

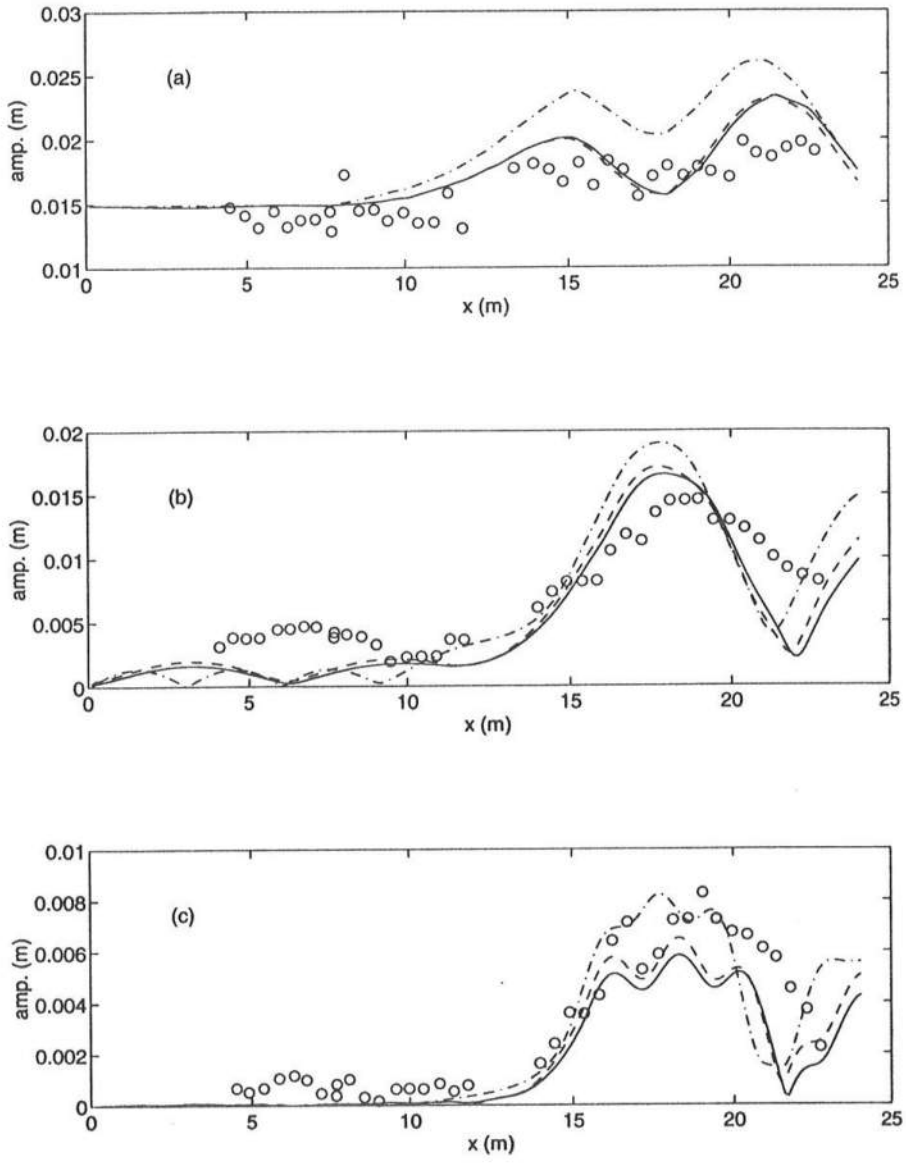

Figure 2: Comparison to Whalin (1971) with $a_o = 1.49cm$. Data (o) vs. present model (—), model of Chen and Liu (1993) (- - -), model of Liu, et al. (1985) (-.-): (a) first harmonic; (b) second harmonic; (c) third harmonic.

A TIME-DEPENDENT MILD-SLOPE EQUATION MODEL FOR BREAKING WAVES

Changhoon Lee and James T. Kirby
Center for Applied Coastal Research, Department of Civil Engineering,
University of Delaware, Newark, DE 19716

ABSTRACT

We develop a time-dependent mild-slope equation model for breaking waves by constructing a model for the energy loss based on a bore analogy and including it in the time-dependent mild-slope equation developed by Radder and Dingemans (1985). The parameter for the energy dissipation rate γ was calibrated against experimental data for one-dimensional monochromatic waves (Horikawa and Kuo, 1966) and was found to be in the range of 0.4 to 0.9. The model is applied here to cases with two-dimensional monochromatic waves (Vincent and Briggs, 1989) and also to cases with one-dimensional random waves (Mase and Kirby, 1992). The more general problem of two-dimensional random waves is described in the presentation.

INTRODUCTION

The combined refraction and diffraction of water waves on a slowly varying bottom was studied by Berkhoff (1972) using the mild-slope equation:

$$\nabla \cdot (CC_g \nabla \hat{\phi}) + k^2 CC_g \hat{\phi} = 0 \tag{1}$$

where C and C_g are phase and group velocities of a wave with local frequency ω, wavenumber k, and $\hat{\phi}$ is the velocity potential at the mean water surface $z = 0$ with time harmonic term extracted. Berkhoff's equation (1) is applicable only to monochromatic waves.

A time-dependent mild-slope equation was first developed by Smith and Sprinks (1975) by means of Green's second identities applied to the velocity potential. The model equation is

$$\frac{\partial^2 \tilde{\phi}}{\partial t^2} - \nabla \cdot (\bar{C}\bar{C}_g \nabla \tilde{\phi}) + (\bar{\omega}^2 - \bar{k}^2 \bar{C}\bar{C}_g)\tilde{\phi} = 0 \tag{2}$$

where $\bar{C}$ and $\bar{C}_g$ are phase and group velocities, respectively, of a narrow-banded wave with carrier frequency $\bar{\omega}$, wavenumber $\bar{k}$, and $\tilde{\phi}$ is the velocity potential at the mean water surface $z = 0$.

A system of time-dependent mild-slope equations was also derived based on the Hamiltonian theory of water waves by Radder and Dingemans (1985). The model equations are

$$\frac{\partial \eta}{\partial t} = -\nabla \cdot (\frac{\bar{C}\bar{C}_g}{g} \nabla \tilde{\phi}) + \frac{(\bar{\omega}^2 - \bar{k}^2 \bar{C}\bar{C}_g)}{g} \tilde{\phi} = F(\tilde{\phi}) \tag{3}$$

$$\frac{\partial \tilde{\phi}}{\partial t} = -g\eta \tag{4}$$

The water surface elevation η may be elimated from (3) and (4) in order to obtain Smith and Sprinks' equation (2).

There has been a recent interest in applying time-dependent forms of the mild-slope wave equation to the modelling of irregular seas in intermediate depth water. Kirby *et al.* (1992) presented a number of computations using the time-dependent mild-slope equations (3) and (4). They studied the propagation of wave groups in order to verify the linear dispersive properties of the model, and then tested the model against several existing data sets, including the wave focusing experiments by Berkhoff *et al.* (1982) (regular waves) and Vincent and Briggs (1989) (regular and irregular waves). At the same time, Kubo *et al.* (1992) developed a model with similar intent but a different governing equation and applied it to a number of examples of interest.

Battjes and Janssen (1978) used a bore analogy to study irregular wave breaking, where the probability of the occurrence of breaking is estimated by Rayleigh distribution with an upper cut-off. Thornton and Guza (1983) used observed wave distributions in estimating the probability of the occurrence of breaking. Both of these methods are statistical in nature. Svendsen (1984) developed a dimensionless energy dissipation rate which depends on both wave height to water depth ratio and wave crest elevation to wave height ratio. Kubo *et al.* (1992) used Isobe's (1987) wave breaking model which was developed to overcome linear model's deficiency in applying to surf zone and which is applicable only for the bottom of uniform slope.

In this presentation, we extend the model of Radder and Dingemans (1985) to include surf zone wave breaking effects. We proceed by constructing a model for the energy loss in a breaking wave based on a bore analogy, as was done in a number of previous studies.

DERIVATION OF MODEL EQUATIONS

Considering the geometry of a hydraulic jump, we write the upstream and downstream water depths h_1 and h_2 as $h_1 \simeq (h - |\eta|)$ and $h_2 \simeq (h + |\eta|)$ where h is still water depth and $|\eta|$ is the wave amplitude. The head loss caused by wave breaking can be estimated as

$$h_L \simeq \frac{[(h + |\eta|) - (h - |\eta|)]^3}{4(h + |\eta|)(h - |\eta|)} = 2|\eta| \frac{(\frac{|\eta|}{h})^2}{1 - (\frac{|\eta|}{h})^2} \tag{5}$$

If the energy loss caused by wave breaking is included in the linear dynamic free surface boundary condition (4), we obtain the following equation

$$\frac{\partial \tilde{\phi}}{\partial t} = -g\eta - D_b\tilde{\phi} = G(\eta, \tilde{\phi}) \tag{6}$$

where the energy dissipation rate D_b is related to the head loss by

$$D_b = \frac{gh_L}{|\tilde{\phi}|} = 2\gamma\bar{\omega}\frac{(\frac{|\eta|}{h})^2}{1-(\frac{|\eta|}{h})^2} \tag{7}$$

where we use the relation

$$\frac{|\eta|}{|\tilde{\phi}|} \simeq \frac{\bar{\omega}}{g} \tag{8}$$

and where γ is a calibration factor of order one. The energy dissipation rate is proportional to the carrier wave frequency and is also approximately proportional to the square of wave height to water depth ratio.

Dally *et al.* (1985) found, from Horikawa and Kuo's (1966) experimental data, that the wave height of the breaking wave attenuates until it reaches a stable wave height, which lies between 0.35 and 0.40 times the water depth. We use the idea of the wave recovery in our model, in order to model the effects of wave breaking in waves propagating over bars and other isolated features.

The energy dissipation rate depends on whether the wave is locally breaking or non-breaking. Even if the wave height to water depth ratio is locally below the breaking criterion, wave breaking still continues if the wave is breaking and the wave height to water depth ratio is above the recovery criterion. The breaking waves can be traced by finding the wave velocities in x and y directions as

$$\begin{aligned} C_x &= \frac{\bar{\omega}}{\bar{k}\cos\theta} \\ C_y &= \frac{\bar{\omega}}{\bar{k}\sin\theta} \end{aligned} \tag{9}$$

where the propagation direction θ can be found by

$$\theta = \begin{cases} +\arctan(\frac{\frac{\partial\eta}{\partial y}}{\frac{\partial\eta}{\partial x}}); & \text{propagating in positive } x \text{ direction} \\ -\arctan(\frac{\frac{\partial\eta}{\partial y}}{\frac{\partial\eta}{\partial x}}); & \text{propagating in negative } x \text{ direction} \end{cases} \tag{10}$$

For the random waves, we separate the whole frequency spectrum into several components with narrow band widths. At each time we compute the water surface elevations of each component. We add all the water surface elevations of each component to get the wave height. If it is determined that wave breaking occurs, the energy dissipation rates D_b are computed differently at different components by using different carrier wave frequencies $\bar{\omega}$, so at higher frequency component there would be more energy dissipations than at the lower frequency component. The propagation directions and the velocities of the breaking waves are obtained at each component to trace the breaking waves. If the wave height to water

depth ratio drops below the the recovery criterion, the wave breaking stops and no energy dissipation would occur.

The sudden increase of the energy dissipation rate at the breaking point causes high frequency noise in the solution, so we smooth the dissipation rate by averaging several adjacent point values with slightly different weight.

The fourth order Adams-Bashforth-Moulton predictor-corrector method is used to discretize (3) and (6). In the predictor step, we have

$$\begin{aligned} \eta^{n+1} &= \eta^n + \frac{\Delta t}{24}\{55F^n - 59F^{n-1} + 37F^{n-2} - 9F^{n-3}\} \\ \tilde{\phi}^{n+1} &= \tilde{\phi}^n + \frac{\Delta t}{24}\{55G^n - 59G^{n-1} + 37G^{n-2} - 9G^{n-3}\} \end{aligned} \tag{11}$$

and in the corrector step, we have

$$\begin{aligned} \eta^{n+1} &= \eta^n + \frac{\Delta t}{24}\{9F^{n+1} + 19F^n - 5F^{n-1} + F^{n-2}\} \\ \tilde{\phi}^{n+1} &= \tilde{\phi}^n + \frac{\Delta t}{24}\{9G^{n+1} + 19G^n - 5G^{n-1} + G^{n-2}\} \end{aligned} \tag{12}$$

where the superscript n denotes the time step. If the errors between predicted and corrected values are small enough, we proceed to next time step; otherwise, we repeat correcting until we get small errors.

PARABOLIC APPROXIMATIONS

For monochromatic breaking waves, if the deviation of the waves from the main direction is small and there is no reflection, the parabolic approximations can be used with minor errors but with more efficiency. The sudden increase of the energy dissipation rate D_b at the breaking point does not cause any disturbance to upstream waves in parabolic approximations.

We extract the harmonic term with the wavenumber k_0 from the velocity potential $\hat{\phi}$ as

$$\hat{\phi}(x,y) = \check{\phi}(x,y)e^{i\int k_0 dx} \tag{13}$$

where $k_0(x)$ represents some weighted average of $k(x,y)$ along y-direction. From the assumption of mild slope of $O(\delta^2)$, we get the parabolic mild-slope equation for monochromatic breaking waves:

$$\frac{\partial}{\partial y}(CC_g\frac{\partial \check{\phi}}{\partial y}) + 2ik_0CC_g\frac{\partial \check{\phi}}{\partial x} + \{(k^2 - k_0^2)CC_g + i(\frac{\partial}{\partial x}(k_0CC_g) + \omega^2 D_b)\}\check{\phi} = 0 \tag{14}$$

where the energy dissipation rate D_b is

$$D_b = 2\gamma\omega\frac{(\frac{\omega}{gh}|\check{\phi}|)^2}{1 - (\frac{\omega}{gh}|\check{\phi}|)^2} \tag{15}$$

The propagation direction of the breaking waves can be found from velocity potential $\check{\phi}$ with error of $O(\delta^2)$ as

$$\theta = \arctan(\frac{\frac{\partial \check{\phi}}{\partial y}}{\frac{\partial \check{\phi}}{\partial x}}) = \arctan(\frac{\frac{\partial \check{\phi}}{\partial y}}{ik_0\check{\phi}}) \tag{16}$$

The Crank-Nicolson method is used to discretize the two-dimensional parabolic equation (14).

For one-dimensional case, equation (14) becomes

$$2k_0CC_g\frac{\partial \check{\phi}}{\partial x} + \{\frac{\partial}{\partial x}(k_0CC_g) + \omega^2 D_b\}\check{\phi} = 0 \tag{17}$$

A modified Euler predictor-corrector method is used to discretize equation (17).

CALIBRATION OF PARAMETERS FOR WAVE BREAKING MODEL

We apply the parabolic model (17) to several cases with experimental data in order to calibrate the parameter for energy dissipation rate γ, the breaking criterion $(H/h)_b$, and the recovery criterion $(H/h)_r$.

Horikawa and Kuo (1966) conducted two types of experiment inside surf zone. The first type of experiment was done for horizontal bottom to determine the reformed wave height after the stop of breaking. The resulting data was used by Dally *et al.* (1985) to determine the recovery criterion $(H/h)_r$ in which the breaking stops. The incident waves broke on a 1/5 sloping bottom and then propagated to the elevated horizontal bottom. The second type of experiment was done for sloping bottom to reveal the influence of bottom slope on the wave transformation inside the surf zone.

For the first case, we considered the experiments with a horizontal bottom of water depth $h_c = 15\ cm$, a wave period $T = 1.0\ sec$, and a ratio of wave height to wavelength in deep water $H_0/L_0 = 0.065 - 0.100$. The value of $(H/h)_b$ is found to be in the range of 0.63 to 0.89 with increasing trend with increasing value of H_0/L_0, while the value of $(H/h)_r$ is found to be in the range of 0.35 to 0.41 with no particular trends (See Figure 1 (a)). The optimum value of γ was chosen to be in the range of 0.4 to 0.9 with increasing trend with increasing value of H_0/L_0 (See Figure 1 (b)). Figure 1 (c) shows the comparison of the wave height attenuations with different values of γ (0.8, 0.9, 1.0) against the experimental data for the case with $H_0/L_0 = 0.100$, $(H/h)_b = 0.89$, $(H/h)_r = 0.37$. Figure 1 (d) shows the energy dissipation rate normalized by wave frequency for the case with $H_0/L_0 = 0.100$, $(H/h)_b = 0.89$, $(H/h)_r = 0.37$, $\gamma = 0.9$.

For the second case, we considered the experiments with bottom slope $s = 1/65$, a wave period $T = 1.6\ sec$, and a ratio of wave height to wavelength in deep water $H_0/L_0 = 0.065$. The value of $(H/h)_b$ is found to be in the range of 0.69 to 0.86 with decreasing trend with increasing value of H_0/L_0 (See Figure 2 (a)). The value of $(H/h)_r$ is fixed to be 0.35. The optimum value of γ was chosen in the range of 0.4 to 0.8 with decreasing trend with increasing value of H_0/L_0 (See Figure 2 (b)). Figure 2 (c) shows the comparison of the wave height

attenuations with different values of γ (0.3, 0.4, 0.5) against the experimental data for the case with $H_0/L_0 = 0.065$, $(H/h)_b = 0.69$, $(H/h)_r = 0.35$. Figure 2 (d) shows the dissipation rate D_b for the case with $H_0/L_0 = 0.065$, $(H/h)_b = 0.69$, $(H/h)_r = 0.35$, $\gamma = 0.4$.

At the wave breaking point, the model underpredicted wave height due to nonlinear effects which are dominant at the breaking point, while the model used is linear. The energy dissipation rate decreased until the water depth of about 0.6 times the water depth at breaking point and then it increased exponentially to the zero depth. This phenomenon was also found in terms of H/h in Horikawa and Kuo's experiments (1966). It is noticable that the value of γ increases with increasing value of $(H/h)_b$. The relation between $(H/h)_b$ and γ is described as

$$\gamma = 1.6805(H/h)_b - 0.7078 \tag{18}$$

with regression coefficient 0.50.

APPLICATIONS TO MONOCHROMATIC AND RANDOM WAVES

In order to dissipate wave energy at downwave boundaries, we presently use a sponge layer at the downwave boundary. Equation 6 is modified to

$$\frac{\partial \tilde{\phi}}{\partial t} = -g\eta - (D_b + D_s)\tilde{\phi} \tag{19}$$

where

$$D_s = \begin{cases} 0, & x \le x_{sponge} \\ \omega(\frac{e^{F^n}-1}{e-1}), & x \ge x_{sponge} \end{cases} \tag{20}$$

$$F = \frac{x - x_{sponge}}{x_{max} - x_{sponge}}, \tag{21}$$

and the sponge length x_{sponge} is specified as 2.5 times the initial wave length (monochromatic waves) or as 2.5 times the longest initial wave length (random waves).

Vincent and Briggs (1989) presented a number of experiments for waves with a combination of monochromatic, narrow-banded or broad-banded frequency spectra and unidirectional, narrow-banded or broad-banded directional spreads.

We apply to the case with a monochromatic unidirectional wave (M3) of a wave height $H = 13.50\ cm$ and a wave period $T = 1.3\ sec$. We select the parameters for wave breaking as $(H/h)_b = 0.78$, $(H/h)_r = 0.35$, $\gamma = 0.6$. The grid size is $\Delta x = \Delta y = 0.1905m$ and time step is $\Delta t = T/80\ sec$ which gives a maximum Courant number of 0.18. The average wave heights are computed between $t = 17.7125\ sec$ and $t = 39\ sec$.

Figure 3 shows that the computed normalized wave heights are not close to the measured data. The computed breaking waves propagated from the shoal to section 4 but only along the center line of wave propagation with narrow width; while, the data show that wave breaking happens widely around the center line of wave propagation.

Mase and Kirby (1992) conducted experiments on one-dimensional random waves shoaling over a plane beach of slope 1/20. The random waves were simulated with a Pierson-Moskowitz spectrum with peak frequency (f_p) of 0.6 Hz and 1.0 Hz, referred as Case 1 and Case 2, respectively. The dominant wave breaking type seen in Case 1 was plunging, while in Case 2 spilling breakers were dominant.

We consider Case 1 here. The sampling interval is 0.04 *sec* and total number of sampling values used is 4096. The incoming energy with extremely low frequencies cannot be absorbed in the sponge layer, while the values of η and $\tilde{\phi}$ with extremely high frequencies cannot be resolved numerically in space and in time. So, the spectrum of 2 percent lowest and highest frequencies were excluded in order to get reasonable solutions. The remaining 96 percent the sepctral density of water surface elevations recorded at depth of 47 *cm* was separated into four components with equal energies. We use a weighted average of the frequencies in each frequency component to determine the representative frequency used to compute the model coefficients for each component. We select the parameters for wave breaking as $(H/h)_b = 0.78$, $(H/h)_r = 0.35$, $\gamma = 1$. The grid size is $\Delta x = 0.04m$ and time step is $\Delta t = 0.0025$ *sec* which gives a maximum Courant number of 0.12. From the chosen grid spacings, the minimum ratio of wavelength to spatial grid size is 6.75. Variances of water surface elevation are computed between $t = 24.4725$ *sec* and $t = 160$ *sec*.

Figure 4 (a) shows the water surface elevations and the wave height to water depth ratio at $t = 160$ *sec*. Figure 4 (b) shows the energy dissipation rate normalized by the highest wave frequency 9.89 sec^{-1} at $t = 260$ *sec* for each frequency component. In Figure 4 (b) the energy dissipation rate at the sponge layer, which starts from 9 m from the corner, is included. Figure 4 (c) shows the comparison of computed and measured normalized water surface elevations at twelve gauge points.

The dissipation rate of the lowest frequency component is the smallest yielding the highest normalized wave heights, while the dissipation rate of the highest frequency component is the largest yielding the lowest normalized wave heights. In surf zone, in reality, the super-harmonics and sub-harmonics of the waves cause the increase of the energy at the high and low frequencies, respectively.

The computed wave heights at depth of 47 *cm* are found to be 3 percent larger than the measured wave heights which can be explained by the fact that the wave reflection occurs from the sudden increase of the energy dissipations in surf zone. The computed wave heights are normalized by the computed wave heights at 47 *cm* deep. The assumed energy dissipation parameter $\gamma = 1$ was found not enough to dissipate the energy in surf zone.

Acknowledgement

This work was supported by the Office of Sea Grant (Grant No. NA/6GR0162-01, Project R/OE-13) and the U.S. Army Research Office (Grant No. DAAL-03-92-G0116). The U.S. Government is authorized to produce and distribute reprints for government purposes, notwithstanding any copyright notation that may appear hereon.

REFERENCES

Berkhoff, J. C. W., (1972) "Computation of combined refraction-diffraction", *Proceedings of the 13th Coastal Engineering Conference*, Vancouver, 471-490.

Battjes, J. A. & J. P. F. M. Janssen, (1978) "Energy loss and set-up due to breaking of random waves", *Proceedings of the 16th Coastal Engineering Conference*, New York, 569-587.

Berkhoff, J. C. W., N. Booij & A. C. Radder, (1982) "Verification of numerical wave propagation models for simple harmonic linear waves", *Coastal Engineering*, 6, 255-279.

Dally, W. R., R. G. Dean & R. A. Dalrymple, (1985) "Wave-height variation across beaches of arbitrary profile", *J. of Geophysical Research*, 90, 11917-11927.

Horikawa, K. & C.-T. Kuo, (1966) "A study on wave transformation inside surf zone", *Proceedings of the 10th Coastal Engineering Conference*, New York, 217-233.

Isobe, M., (1987) "A parabolic equation model for transformation of irregular waves due to refraction, diffraction and breaking", *Coastal Engineering in Japan*, 30, 38-48.

Kirby, J. T., C. Lee & C. Rasmussen, (1992) "Time-dependent solutions of the mild-slope wave equation", *Proceedings of the 23rd International Conference on Coastal Engineering*, Venice, 391-404.

Kubo, Y., Y. Kotake, M. Isobe & A. Watanabe, (1992) "Time-dependent mild-slope equation for random waves", *Proceedings of the 23rd International Conference on Coastal Engineering*, Venice, 419-431.

Mase H. & J. T. Kirby, (1992) "Hybrid frequency-domain KdV equation for random wave transformation", *Proceedings of the 23rd International Conference on Coastal Engineering*, Venice, 474-487.

Radder, A. C. & M. W. Dingemans, (1985), "Canonical equations for almost periodic, weakly nonlinear gravity waves", *Wave Motion*, 7, 473-485.

Smith, R. & T. Sprinks, (1975) "Scattering of surface waves by a conical island", *J. of Fluid Mechanics*, 72, 373-384.

Svendsen, I. A., (1984) "Wave heights and set-up in a surf zone", *Coastal Engineering*, 8, 303-329.

Thornton E. B. & R. T. Guza, (1983) "Transformation of Wave Height Distribution", *J. of Geophysical Research*, 88, 5925-5938.

Vincent, C. L. & M. J. Briggs, (1989) "Refraction and diffraction of irregular waves over a mound", *J. of Waterway, Port, Coastal, and Ocean Engineering*, 115, 269-284.

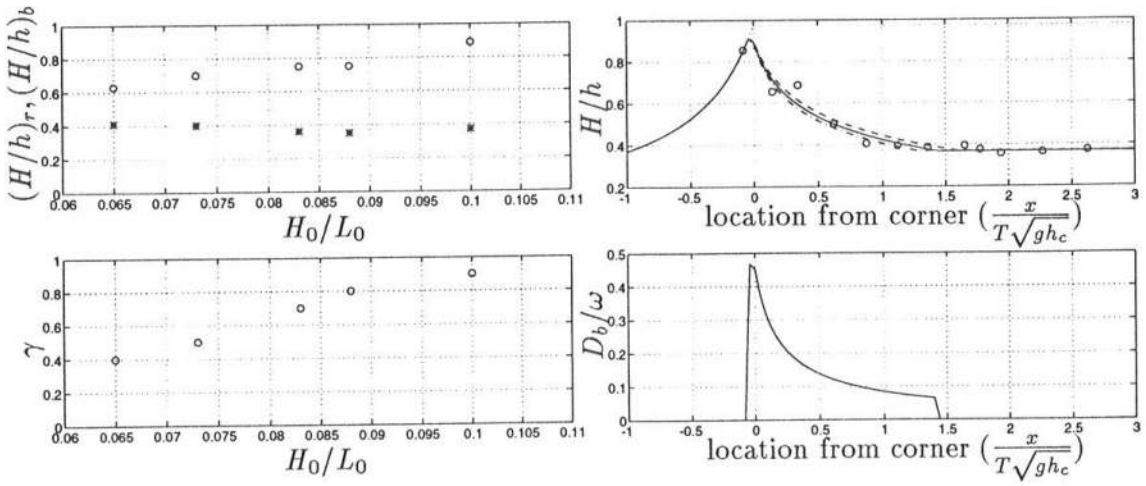

Figure 1: calibration of wave breaking parameters for horizontal bottom with $T = 1$ *sec*, $h_c = 15$ *cm* (a) $\circ$: $(H/h)_b$, $*$: $(H/h)_r$, (b) γ, (c) attenuation of H/h with different values of γ for $H_0/L_0 = 0.100$, $(H/h)_b = 0.89$, $(H/h)_r = 0.37$ (dashed line: $\gamma = 0.8$, solid line: $\gamma = 0.9$, dash-dotted line: $\gamma = 1.0$, dotted line: shoaling coefficient), (d) D_b/ω for $H_0/L_0 = 0.100$, $(H/h)_b = 0.89$, $(H/h)_r = 0.37$, $\gamma = 0.8$

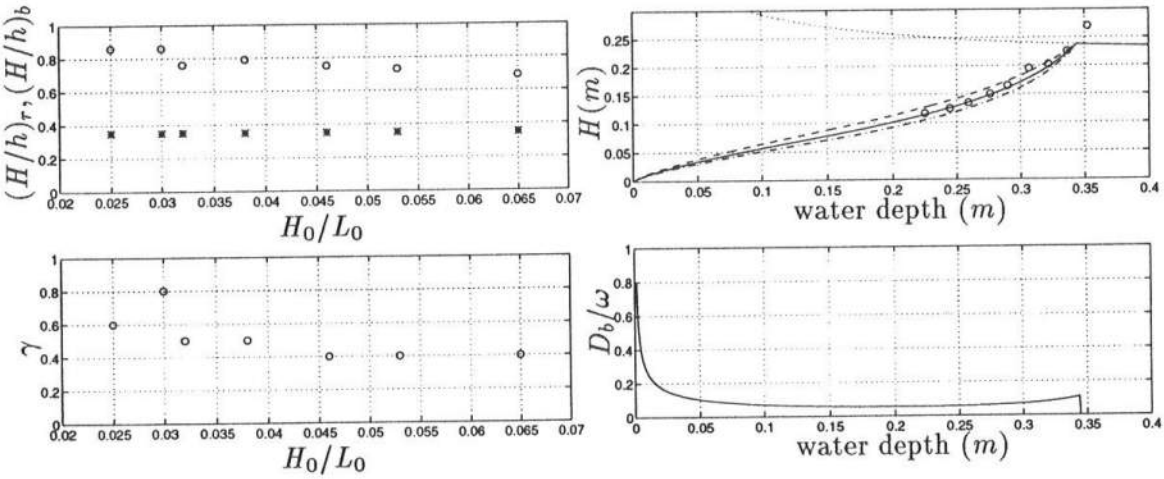

Figure 2: calibration of wave breaking parameters for sloping bottom with $s = 1/65, T = 1.6$ *sec* (a) $\circ$: $(H/h)_b$, $*$: $(H/h)_r$, (b) γ, (c) attenuation of H with different values of γ for $H_0/L_0 = 0.065$, $(H/h)_b = 0.69$, $(H/h)_r = 0.35$ (dashed line: $\gamma = 0.3$, solid line: $\gamma = 0.4$, dash-dotted line: $\gamma = 0.5$, dotted line: shoaling coefficient), (d) D_b/ω for $H_0/L_0 = 0.065$, $(H/h)_b = 0.69$, $(H/h)_r = 0.35$, $\gamma = 0.4$.

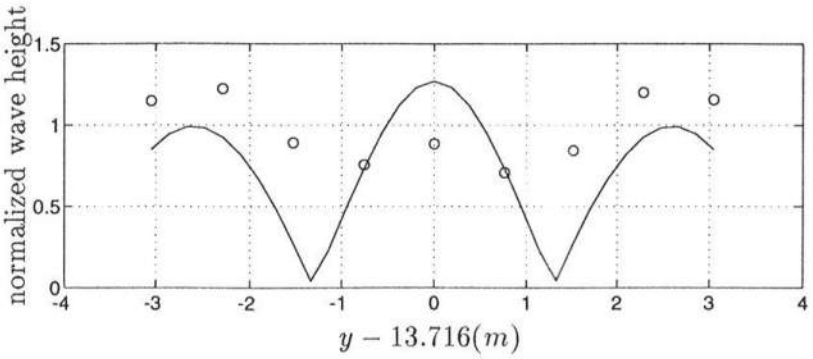

Figure 3: measured and computed normalized wave heights along section 4 (o: measured data, solid line: computed results).

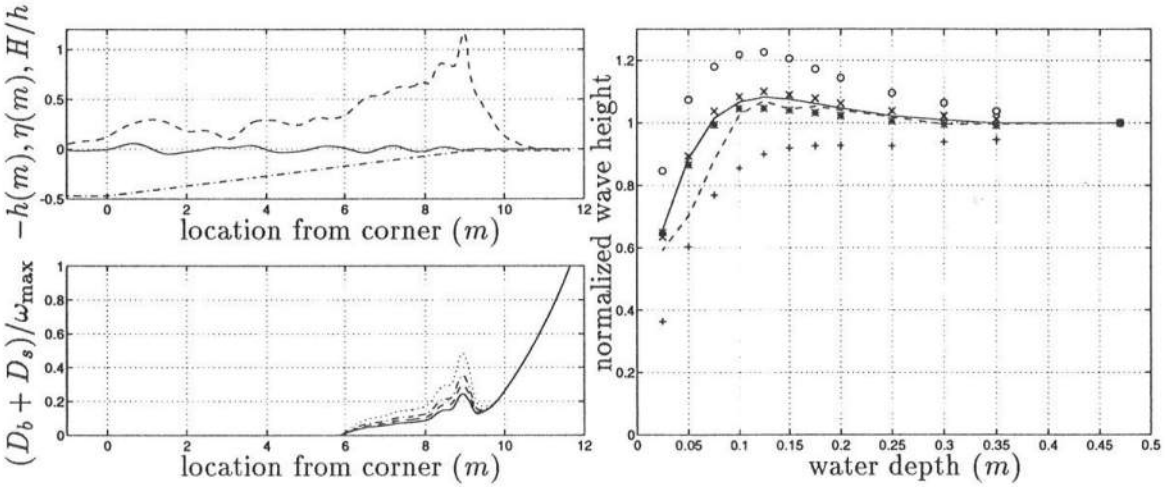

Figure 4: (a) solid line: η, dashed line: H/h, dash-dotted line: $-h$ at $t = 260$ *sec.* (b) $(D_b + D_s)/\omega_{max}$ (solid line: first frequency component, dashed line: second frequency component, dash-dotted line: third frequency component, dotted line: fourth frequency component), (c) normalized wave heights (dashed line: measured data, solid line: whole frequency component, o: first frequency component, $*$: second frequency component, $\times$: third frequency component, $+$: fourth frequency component).

COMPARISON OF MODIFIED BOUSSINESQ AND FULLY NONLINEAR POTENTIAL MODELS FOR SHOALING SOLITARY WAVES

Stephan T. Grilli and Ravishankar Subramanya
Dept. of Ocean Engng., University of Rhode Island, Narragansett, RI 02882.

and

James T. Kirby and Ge Wei
Center for Applied Coastal Research, University of Delaware, Newark, DE 19716.

ABSTRACT

An existing modified Boussinesq model (MBM), with improved linear dispersion characteristics, and a newly developed fully nonlinear version of the same model (FNBM), are used to compute shoaling of solitary waves over a slope. Computational results are compared to results of a fully nonlinear potential flow model (FNPF) that provides a reference solution. Results with the FNBM show significant improvement in accuracy as compared to the solution with the MBM. The FNBM is found to perform better, particularly for waves close to breaking, in predicting wave shape, height, and particle velocity. Although well predicted in the FNBM, except close to breaking, wave celerity is slightly better predicted in the MBM.

INTRODUCTION

Dispersion properties of standard Boussinesq models (BM) have recently been improved by expressing the equations as a function of the horizontal velocity at an arbitrary distance z_α below the still water level (Nwogu, 1993). When using $z_\alpha = -0.53h$, the optimal value, Nwogu showed that the corresponding modified (or extended) Boussinesq model (MBM) can approximate the linear dispersion relationship over a much larger range of water depth than the standard Boussinesq equations. Using his model, Nwogu was able to accurately calculate surface elevations in intermediate water, up to large wave steepness, for the shoaling of periodic waves over a gentle slope.

Nonlinear properties of the MBM, however, are essentially identical to those of a standard model of identical truncation order (i.e., usually of first-order). Kirby and Wei (1994) recently extended the MBM to full nonlinearity in the free surface boundary conditions. This fully nonlinear Boussinesq model (FNBM) conserves the dispersion properties of the MBM while accounting for nonlinear effects to all orders. Notice, however, that as with standard Boussinesq models the horizontal velocity in the FNBM is still quadratic as a function of depth z (which becomes a limitation, the deeper the water).

In parallel with the development of weakly nonlinear or fully nonlinear BM's and their application to wave shoaling, another approach has been increasingly successful for computing wave shoaling up to breaking over a sloping bottom. It is based on solving the fully nonlinear potential flow equations (FNPF) in the vertical plane, for an arbitrary bottom topography and for arbitrary incident waves (Grilli *et al.* 1989; Grilli 1993). Grilli *et al.* (1994) used such a FNPF model to calculate shoaling of solitary waves over a gentle slope. Comparing their computations to laboratory experiments over a 1:35 slope, they showed that surface elevations could be calculated to within 1% of the measurements, up to and beyond the theoretical breaking point for which the wave has a vertical tangent on the front face. Svendsen *et al.* (1994), using new adaptive regridding techniques by Grilli and Subramanya (1994), were able to accurately compute characteristics and kinematics of breaker jets for solitary waves, up to impact of the jets on the free surface.

FNPF models, hence, provide a "numerically exact" solution of the fundamental equations, which Boussinesq models only solve approximately, that also appears to model the physics quite well. FNPF models, however, are computationally expensive, even in their two-dimensional formulation, and their extension to three dimensions appears even more prohibitive. Approximate models like BM's, on the other hand, although limited in accuracy by both their truncation error and their inability to handle overturning waves, are only one-dimensional (for the two-dimensional problem) and, therefore, are much more computationally efficient than FNPF models.

It is thus desirable to assess the accuracy of computations with the BM's versus the FNPF reference solution, for the important case of wave shoaling over a slope. In this presentation, the FNPF model by Grilli *et al.* (1989), with the latest numerical improvements by Grilli and Subramanya (1994), is used to assess the accuracy of both a computationally improved version of the MBM by Nwogu (1993), developed by Wei and Kirby (1994), and the FNBM by Kirby and Wei (1994), for the shoaling of solitary waves over a plane slope. Solitary waves are used as incident waves both for simplicity, since they do not require using an absorbing beach in the model (see Subramanya and Grilli, 1994), and because of the recent experimental validation of the FNPF calculations for solitary wave shoaling and breaking over a slope (Grilli, *et al.* 1994).

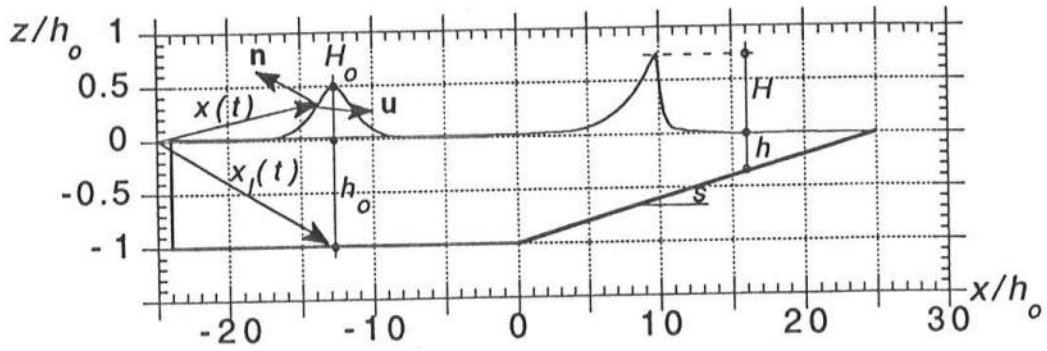

Figure 1: Definition sketch for both the FNPF computations and for the Boussinesq models.

NUMERICAL MODELS

Fully nonlinear potential model

Equations for the FNPF model are briefly listed in the following. Details can be found in Grilli *et al* (1989) and in Grilli (1993). The velocity potential $\phi(\boldsymbol{x},t)$ is used to represent inviscid irrotational 2D flows in the vertical plane (x,z) and the velocity is defined by, $\boldsymbol{u} = \nabla\phi = (u,w)$ (Fig. 1). Continuity equation in the fluid domain $\Omega(t)$ with boundary $\Gamma(t)$ is a Laplace's equation for the potential,

$$\nabla^2\phi = 0 \qquad \text{in } \Omega(t) \tag{1}$$

Using the free space Green's function, $G(\boldsymbol{x},\boldsymbol{x}_l) = -(1/2\pi)\log|\,\boldsymbol{x}-\boldsymbol{x}_l\,|$, and second Green's identity, equation (1) transforms into the Boundary Integral Equation (BIE),

$$\alpha(\boldsymbol{x}_l)\phi(\boldsymbol{x}_l) = \int_{\Gamma(\boldsymbol{x})}[\frac{\partial\phi}{\partial n}(\boldsymbol{x})G(\boldsymbol{x},\boldsymbol{x}_l) - \phi(\boldsymbol{x})\frac{\partial G(\boldsymbol{x},\boldsymbol{x}_l)}{\partial n}]\,d\Gamma(\boldsymbol{x}) \tag{2}$$

in which $\boldsymbol{x} = (x,z)$ and $\boldsymbol{x}_l = (x_l,z_l)$ are position vectors for points on the boundary, $\boldsymbol{n}$ is the unit outward normal vector, and $\alpha(\boldsymbol{x}_l)$ is a geometric coefficient. Equation (2) is solved by a Boundary Element Method, using a set of collocation nodes on the boundary and higher-order elements to interpolate in between the collocation nodes. Integrals in (2) are evaluated numerically and the resulting algebraic system of equations is assembled and solved for the equivalent discretized problem.

Along the stationary bottom Γ_b, and on other fixed boundaries of the domain, like Γ_{r2}, a no-flow condition is prescribed as,

$$\frac{\partial\phi}{\partial n} = 0 \qquad \text{on } \Gamma_b \text{ and } \Gamma_{r2} \tag{3}$$

Waves can be generated in the model by simulating a piston wavemaker motion on the "open sea" boundary of the computational domain, $\Gamma_{r1}(t)$, or by specifying the potential and

the elevation of the incident wave directly on the free surface. For incident solitary waves, an exact solution of the fully nonlinear equations, obtained using Tanaka's (1986) method, is used as initial wave and introduced directly on the free surface.

On the free surface $\Gamma_f(t)$, ϕ satisfies the kinematic and dynamic boundary conditions,

$$\frac{D\boldsymbol{r}}{Dt} = (\frac{\partial}{\partial t} + \boldsymbol{u}\cdot\nabla)\boldsymbol{r} = \boldsymbol{u} = \nabla\phi \qquad \text{on } \Gamma_f(t) \tag{4}$$

$$\frac{D\phi}{Dt} = -gz + \frac{1}{2}\nabla\phi\cdot\nabla\phi - \frac{p_a}{\rho} \qquad \text{on } \Gamma_f(t) \tag{5}$$

respectively, with $\boldsymbol{r}$, the position vector on the free surface, g the gravitational acceleration, z the vertical coordinate, p_a the pressure at the free surface, assumed zero in the applications, and ρ the fluid density. Free surface boundary conditions (4) and (5) are integrated in time based on two second-order Taylor series expansions, for ϕ and $\boldsymbol{r}$, expressed in terms of a time step Δt and of the Lagrangian time derivative, D/Dt. Trajectories of individual free surface particles—identical to nodes of the BEM discretization—are thus calculated based on these Taylor series. The time step is automatically selected in the model, based on a mesh Courant number, to ensure optimal accuracy and stability of computations. In the applications, spatial and temporal discretizations were selected for the errors on wave volume and energy to stay to within 0.05% during most of the wave propagation (see Grilli and Subramanya, 1994, for details of typical discretizations, numerical parameters, and computational errors for solitary wave shoaling in shallow water).

Modified Boussinesq models

BM's are derived based on the fully nonlinear potential flow equations (1)-(5), expressed in nondimensional form using two parameters, $\delta = a/h_o$, which represents nonlinearity, and $\mu^2 = (k_o h_o)^2$, which represents dispersion, in which a is a reference amplitude and k_o a reference wave number (see Kirby and Wei, 1994).

An equation expressing volume flux conservation is obtained by integrating the continuity, bottom boundary, and kinematic free surface boundary, conditions (1)-(4) over z, from $-h$ to $\delta\eta$, as,

$$\frac{\partial\eta}{\partial t} + \nabla\cdot\mathrm{M} = 0; \qquad \mathrm{M} = \int_{-h}^{\delta\eta}\nabla\phi dz \tag{6}$$

In which η is the surface elevation, h is the local depth, and M is the volume flux. Equation (6) is valid for all BM's provided M has the required expression.

The dynamic free surface boundary condition (Bernoulli) (5) is then used to obtain a momentum equation. Defining, $\boldsymbol{u}_\alpha = \nabla\phi|_{z_\alpha}$ (the velocity at depth z_α), and retaining terms to $O(\mu^2)$ and to all orders in δ gives a fully nonlinear version of the Boussinesq model

(FNBM), with volume flux,

$$\begin{aligned} \mathrm{M} &= (h+\delta\eta)\left[\boldsymbol{u}_\alpha + \mu^2\left\{\left[\frac{1}{2}z_\alpha^2 - \frac{1}{6}(h^2 - h\delta\eta + (\delta\eta)^2)\right]\nabla(\nabla\cdot\boldsymbol{u}_\alpha)\right.\right. \\ &\quad \left.\left. + \left[z_\alpha + \frac{1}{2}(h-\delta\eta)\right]\nabla(\nabla\cdot(h\boldsymbol{u}_\alpha))\right\}\right] + O(\mu^4) \end{aligned} \tag{7}$$

and momentum equation,

$$\boldsymbol{u}_{\alpha t} + \delta(\boldsymbol{u}_\alpha\cdot\nabla)\boldsymbol{u}_\alpha + \nabla\eta + \mu^2\mathrm{V}_1 + \delta\mu^2\mathrm{V}_2 = O(\mu^4) \tag{8}$$

where,

$$\begin{aligned} \mathrm{V}_1 &= \frac{1}{2}z_\alpha^2\nabla(\nabla\cdot\boldsymbol{u}_{\alpha t}) + z_\alpha\nabla(\nabla\cdot(h\boldsymbol{u}_{\alpha t})) \\ &\quad -\nabla\left[\frac{1}{2}(\delta\eta)^2\nabla\cdot\boldsymbol{u}_{\alpha t} + \delta\eta\nabla\cdot(h\boldsymbol{u}_{\alpha t})\right] \end{aligned} \tag{9}$$

$$\begin{aligned} \mathrm{V}_2 &= \nabla\left[(z_\alpha - \delta\eta)(\boldsymbol{u}_\alpha\cdot\nabla)(\nabla\cdot(h\boldsymbol{u}_\alpha)) + \frac{1}{2}(z_\alpha^2 - (\delta\eta)^2)(\boldsymbol{u}_\alpha\cdot\nabla)(\nabla\cdot\boldsymbol{u}_\alpha)\right] \\ &\quad +\frac{1}{2}\nabla\left[(\nabla\cdot(h\boldsymbol{u}_\alpha) + \delta\eta\nabla\cdot\boldsymbol{u}_\alpha)^2\right] \end{aligned} \tag{10}$$

The modified Boussinesq model (MBM) of Nwogu (1993) is recovered by neglecting terms of $O(\mu^4, \delta\mu^2)$ in (7)-(10).

In both the MBM and the FNBM versions of the equations, $z_\alpha = -0.531h$ is used in order to obtain dispersion properties closest to the linear dispersion relation. Equations (6)-(10) are solved for both BM's, using an efficient fourth-order predictor-corrector scheme (Wei and Kirby, 1994).

Wei and Kirby (1994) derived the solitary wave solution for the MBM and showed that it slightly differs from the standard (sech^2) Boussinesq solitary wave. For the FNBM, the solitary wave solution is numerically obtained by propagating a Boussinesq solitary wave over a long distance of propagation over constant depth, until it stabilizes in shape and height. These respective solitary wave solutions are used as initial waves for the present application with both BM's.

APPLICATIONS

The shoaling of solitary waves is calculated over a 1:35 slope using the FNPF, MBM, and FNBM models. The computational domain has a constant depth region h_o for $x < 0$ and the slope starts at $x = 0$ (Fig. 1). Since little differences exist in the wave celerities calculated in the three models for the propagation of a solitary wave over constant depth, incident waves were synchronized in the models when their crest reaches the toe of the slope, i.e., initial time $t' = t\sqrt{g/h_o} = 0$ for $x' = x/h_o = 0$.

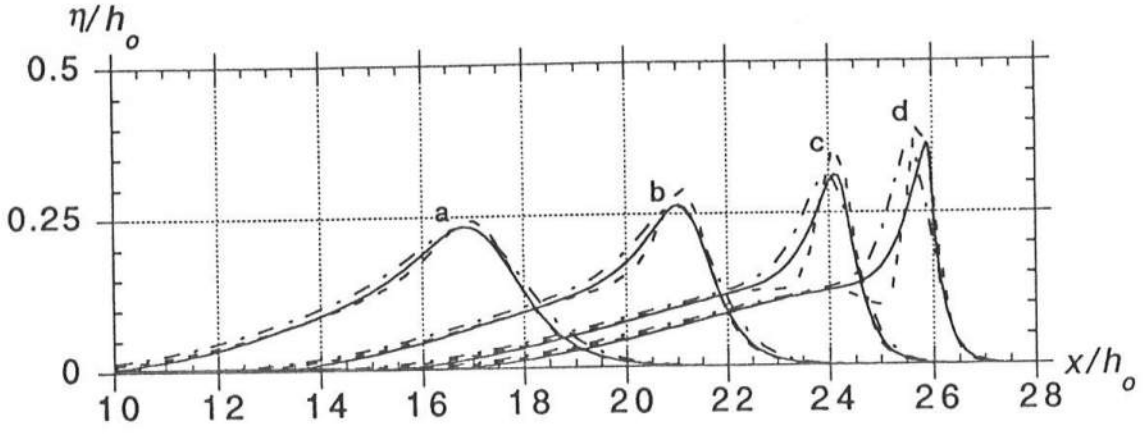

Figure 2: Comparison between FNPF (——), MBM (- - - - -), and FNBM (— - —) results for the shoaling of a solitary wave on a 1:35 slope, with $H'_o = 0.2$ and t' = a : 16.243; b : 22.640; c : 24.032; d : 25.936. The last FNPF profile corresponds to the theoretical breaking point for which the wave front face has a vertical tangent.

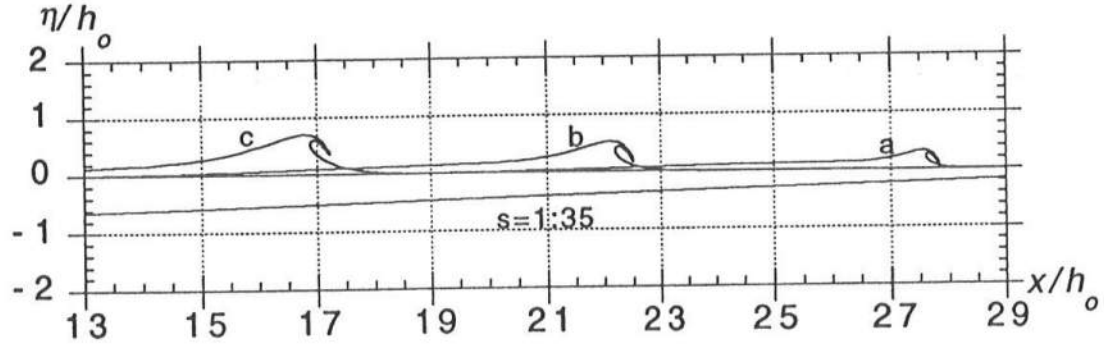

Figure 3: Last computed FNPF (——) wave profiles for the shoaling of solitary waves on a 1:35 slope, with H'_o = a : 0.20; b : 0.40; and c : 0.60, and t' = a : 27.829; b : 19.038; and c : 13.096.

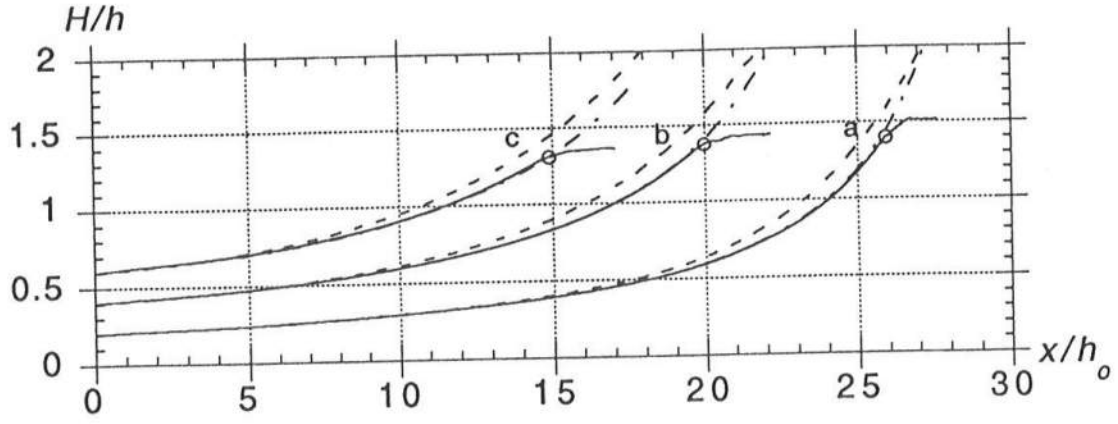

Figure 4: Comparison between FNPF (——), MBM (- - - - -), and FNBM (— - —) shoaling rates, H/h, on a 1:35 slope, for solitary waves with H'_o = a : 0.20; b : 0.40; and c : 0.60. Symbols (o) denote location of the breaking point in the FNPF calculations, for which the wave has a vertical tangent on the front face.

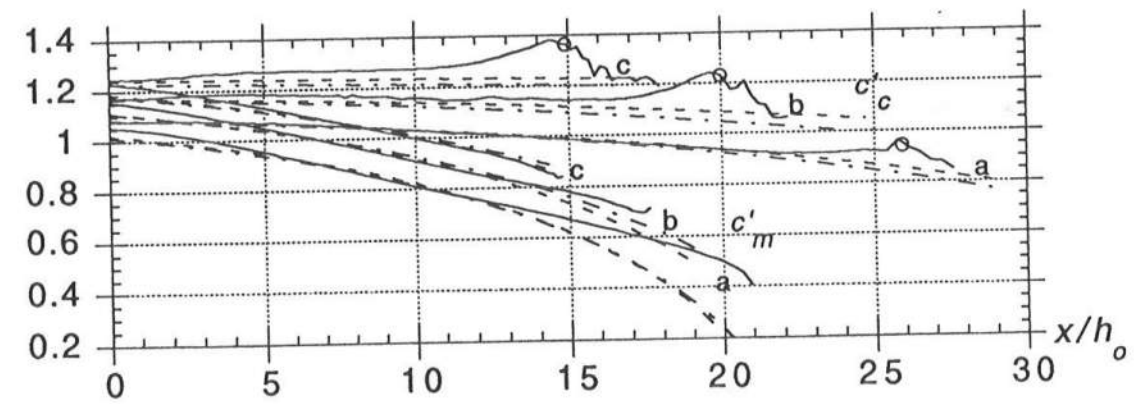

Figure 5: Same comparison as in Fig. 4 for the wave crest celerity c'_c (upper curves) and the celerity of the center of mass c'_m (lower curves).

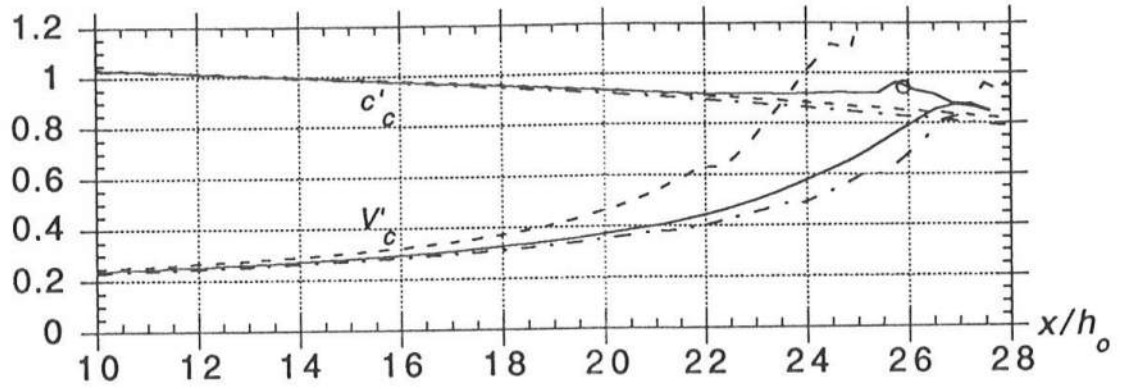

Figure 6: Same comparison as in Fig. 4 for the wave crest celerity c_c' and the particle velocity at the crest V_c', for an incident solitary wave with $H_o' = 0.20$.

Fig. 2 shows a comparison of four wave profiles computed with all three models for an incident solitary wave with height $H_o' = H_o/h_o = 0.20$. The first profile (a) corresponds to the waves being at a location roughly half way up the slope. Wave asymmetry is not too pronounced yet and one can see that, except for the height in the MBM, both BM solutions agree quite well with the FNPF solution. Notice that, although it closely matches the wave height calculated in the FNPF model, the FNBM solution exhibits slightly larger amplitudes on both sides of the crest, i.e., a slightly larger initial wave volume. This indicates that the initial FNBM solitary wave is a little wider than the other two initial waves.

The last profile (d) in Fig. 2 corresponds to the theoretical breaking point in the FNPF model, for which the wave has a vertical tangent in the front face. This breaking point was found by Grilli *et al.* (1994) to also closely correspond to measured breaking location and characteristics, under well controlled laboratory experiments. Breaking thus occurs in Fig. 2 for $t' = 25.94$ at $x_b' = 25.90$, and with a breaking index $H_b/h_b = 1.402$. Results show that, with both the MBM and the FNBM models, the waves travel almost at the right speed in the early shoaling, but too slowly in the upper slope region ($x' > 24$). With the MBM, the wave significantly overshoals as compared to the FNPF results, particularly in the upper slope region, and a spurious secondary trough is predicted behind the main crest for $x' > 24$. With the FNBM, however, both overshoaling and spurious trough are almost non-existent (at least for this slope).

Similar computations were carried out for larger waves (H_o' =0.40 and 0.60) using all three models. With the FNPF model, large scale overturning of the crest occurred in all three cases (plunging breaking) and computations were interrupted when the breaker jet impacted the free surface (Fig. 3; and see Svendsen *et al.*, 1994, for more information about breaker characteristics). Using the BM's, computed wave profiles were qualitatively similar, up to the breaking point, to those obtained with $H_o' = 0.20$. Results for the relative wave height, H/h, computed with all three models, are given in Fig. 4 as a function of x' (symbols (o) mark the FNPF breaking point). At the breaking point, wave height is overpredicted by 13-17% with the MBM, whereas little or no overprediction occurs with the FNBM. Beyond the

the theoretical breaking point, wave height growth is unbounded in both BM's. Fig. 4 also shows that, with the MBM, wave overshoaling mostly occurs in the region of high nonlinearity (i.e., high H/h) closer to the breaking point. This is likely due to insufficient nonlinear effects in the MBM and seems to be well corrected in the FNBM. It is worth mentioning that, when using the original numerical algorithm by Nwogu (1993) (and not the present improved predictor-corrector method), the MBM gives a much worse prediction for the wave height, with discrepancies of up to 55% at the breaking point, as compared to the FNPF results.

Shoaling of the same solitary waves as in Fig. 4 was also calculated with the three models, for both milder (1:100) and steeper (1:15, 1:8) slopes. Results, not reported here, while confirming the general trend in Fig. 2 and 4, exhibit larger discrepancies between the surface elevation and the wave height predictions with both BM's, and the FNPF results. It seems, hence, that the FNBM works at best for an average slope on the order of 1:35.

Wave celerities were calculated for the three incident wave heights, H_o' =0.2, 0.4, and 0.6, using all three models. The corresponding incident wave celerity $c_o' = c_o/\sqrt{gh_o}$ is almost identical in all three models. Results are reported in Fig. 5, for both the crest celerity calculated as $c_c' = \frac{dx_c}{dt}/\sqrt{gh_o}$, as a function of crest location x_c', and for the celerity of the wave center of mass c_m', as a function of the center of mass location (i.e., slightly behind the crest). Results show that both BM's slightly underpredict the wave crest celerity as compared to the FNPF results, for most of the shoaling propagation, with a larger discrepancy close to the breaking point. This was already observed in Fig. 2 for $H_o' = 0.2$. Similar discrepancies also occur for c_m'. In fact, although its dispersion characteristics should be identical to those of the MBM, the FNBM, here, gives a slightly worse celerity prediction than the MBM. This could be due to the slight difference in incident solitary wave profiles.

Particle velocities at the crest, V_c', calculated in all three models for $H_o' = 0.2$ are compared in Fig. 6, where corresponding crest celerities have also been reproduced from Fig. 5. The FNPF model predicts, as expected, that $V_c' \geq c_c'$ at breaking (in fact slightly beyond the breaking point). The particle velocity at the crest in the MBM starts diverging from the FNPF solution, about half way up the slope, whereas the particle velocity in the FNBM stays quite close to the FNPF prediction with a maximum discrepancy of 16% at the breaking point. In fact, despite the discrepancies at breaking in the FNMB, $V_c' = c_c'$ (i.e., breaking) roughly occurs at the same location as for the FNPF model. This observation is also true for the other tested slopes (not reported here).

CONCLUSIONS

Computational results using a MBM and a FNBM were compared to a FNPF reference solution, for the shoaling of solitary waves over a slope. Results with the FNBM show significant improvement in accuracy as compared to the solution with the MBM. The FNBM is found to perform better, particularly for waves close to breaking, in predicting wave shape, height, and particle velocity. Although well predicted in the FNBM, except close to

More results will be presented during the conference that confirm these conclusions.

Acknowledgements

SG and RS acknowledge support for this work of the NRL-SSC, grant N00014-94-1-G607, from the Department of the Navy, Office of the Chief of Naval Research. JK and GW acknowledge support of the University Research Initiative grant DAAL 03-92-G-0116 from the Army Research Office. The information reported in this work does not necessarily reflect the position of the Government.

REFERENCES

Grilli, S., 1993, "Modeling of Nonlinear Wave Motion in Shallow Water." Chapter 3 in *Computational Methods for Free and Moving Boundary Problems in Heat and Fluid Flow* (eds. L.C. Wrobel and C.A. Brebbia), pps. 37-65, Computational Mechanics Publication, Elsevier Applied Sciences, London, UK.

Grilli, S., Skourup, J., and Svendsen, I.A., 1989, "An Efficient Boundary Element Method for Nonlinear Water Waves." *Engineering Analysis with Boundary Elements,* **6**(2), 97-107.

Grilli, S.T. and R. Subramanya, 1994, "Numerical Modeling of Wave Breaking Induced by Fixed or Moving Boundaries." *Journal of Computational Physics* (submitted).

Grilli, S.T., Subramanya, R., Svendsen, I.A., and Veeramony, J., 1994, "Shoaling of Solitary Waves on Plane Beaches." *J. of Waterway Port Coastal and Ocean Engng.,* (in press).

Kirby, J.T. and Wei G., 1994, "Derivation and Properties of a Fully Nonlinear Extended Boussinesq Model", this conference.

Nwogu, O., 1993, "An alternative form of the Boussinesq equations for nearshore wave propagation", *J. Waterway, Port, Coastal and Ocean Engineering*, **119**(6), 618-638.

Svendsen, I.A., Grilli, S.T., and Subramanya, R., 1994, "Breaking Criterion and Breaking Patterns for Solitary Waves on Beaches." *J. of Waterway Port Coastal and Ocean Engng.,* (submitted).

Subramanya, R. and Grilli, S.T., 1994, "Kinematics and Integral Properties of Fully Nonlinear Waves Shoaling over a Slope", this conference.

Tanaka, M., 1986, "The Stability of Solitary Waves." *Phys. Fluids,***29**(3), 650-655.

Wei, G. and J.T. Kirby, 1994, "A Time-dependent Numerical Code for Extended Boussinesq Equations." *J. of Waterway Port Coastal and Ocean Engng.,* (submitted).

VELOCITY STRUCTURE IN IG WAVES

Ib A. Svendsen[1] and Uday Putrevu[2]

ABSTRACT

The vertical structure of the velocity profiles in infragravity waves is analyzed. It is shown that while the velocity under free IG waves does not vary significantly with the vertical coordinate, the velocity under forced IG waves has a substantial vertical structure. The dispersion coefficient (caused by the vertical variations of the velocities in steady currents and infragravity waves) which is an important part of the lateral mixing in the nearshore region is found to have substantial temporal variations and an increased mean value.

1 INTRODUCTION

Recent field observations have shown that there is significant energy present at infragravity frequencies in the surf-zone. In some cases, the energy at infragravity frequencies exceeds the energy present at the short wave frequencies (Wright *et al.* 1982, Guza & Thornton 1982). Herbers *et al.* (1992) measured the infragravity energy outside the surf-zone and found it to be much higher than the predictions of bound long waves created by the short wave motion observed at the same time. They concluded that infragravity waves generated in the nearshore region and radiated out are frequently the dominant source of energy in the infragravity band (see also Elgar *et al.* 1992).

Though several mechanisms have been proposed for the generation of infragravity waves, the dominating mechanism in the nearshore region is probably associated with the wave breaking.

Symonds *et al.* (1982) and Schaffer & Svendsen (1988) proposed such mechanisms for the generation of infragravity waves in the surf-zone and particularly studied the breaking

[1]Center for Applied Coastal Research, Department of Civil Engineering,University of Delaware, Newark, DE 19716, U.S.A.

[2]NorthWest Research Associates, P.O. Box 3027, Bellevue, WA 98009, U.S.A.

of wave groups. Symonds *et al.* assumed that since the individual waves in a group have different wave heights they will break at different locations thereby causing a time variation of the break point position, and that all the groupiness of the incident wave field is destroyed by the breaking process. The lack of groupiness in the surf-zone implies that no further long wave generation takes place so that all the long wave motion inside the surf-zone consists entirely of free long waves.

Schaffer & Svendsen (1988) considered the other extreme assuming that all the waves in a group broke at a fixed location. This implies that the group structure of the incident wave field is completely transmitted into the surf-zone. Their results showed that the groups of broken waves continue the generation of long waves at the group period, and the long wave motion in the surf-zone becomes a combination of free and forced long waves.

In the present paper we consider a situation where the short waves in the surf zone show a wave height variation (groupiness) due to the presence of different wave components.

At first glance one would expect that, since the infragravity waves are long waves, the horizontal particle velocities in the waves would be largely uniform over depth. This actually also turns out to be true for cases where the long wave motion predominantly consists of free long waves with no or very little local long wave generation. However, if the short wave motion in the surf zone shows even a moderate variation (10% in the case of regular wave groups considered here), the horizontal velocities in the long wave motion have a very strong variation over depth.

The basic equations and boundary conditions for the problem are outlined in Section 2. Section 3 presents a brief description of the solution and Section 4 gives numerical results that illustrate the nature of the possible flow situations, conclusions are offered in Section 5.

2 GOVERNING EQUATIONS

For simplicity, we limit the analysis to the case of 2D surf-beats (no along-shore variation) generated by periodic wave groups on a gently sloping plane beach. Furthermore, we restrict ourselves to shallow water so that the pressure variation in the long waves is hydrostatic under the free surface. We also note that in the short-wave-averaged approach used here, the infragravity wave motion is equivalent to a time varying current. The appropriate equations can therefore be deduced from the general equations derived by Svendsen & Lorenz (1989). Under the conditions indicated, the depth variations of the cross-shore component of the short-wave-averaged velocity is governed by

$$\frac{\partial U}{\partial t} - \frac{\partial}{\partial z}\left(\nu_t \frac{\partial U}{\partial z}\right) = -g\frac{\partial \bar{\zeta}}{\partial x} - \overline{u_w \frac{\partial u_w}{\partial x}} \tag{1}$$

Here the turbulent stresses have been parameterized by an eddy viscosity ν_t, $U(x,z,t)$ represents the shore-wave-averaged velocities, u_w represents the short wave induced velocity component in the cross-shore (x) direction. In (1) and all subsequent equations, an overbar denotes a quantity averaged over a short wave period, $\bar{\zeta}$ is the short-wave-averaged free surface elevation (equivalent to the surface elevation in the infragravity waves superposed on the steady set-up).

Eq. (1) represents an extension to the time varying situation for the usual equations governing the undertow and longshore currents, and hence requires boundary conditions similar to what has been used for example for undertow models. We restrict ourselves to periodic infragravity motions and thereby eliminate the need for initial conditions.

As one boundary condition, we relate the bottom shear stress to the velocity profile

$$\rho \nu_t \frac{\partial U}{\partial z}\Big)_{z=-h_0} = \tau_b \tag{2}$$

and assume that the bed shear stress is related to the near bottom velocity $U_b = U(z = -h_0)$ by

$$\tau_b = \frac{1}{2}\rho f_w u_0 U_b \tag{3}$$

where f_w is a friction factor and u_0 is the amplitude of the near bottom short-wave induced oscillatory velocity. (2) and (3) lead to the following boundary condition for the velocity profile (Svendsen & Hansen 1988)

$$\nu_t \frac{\partial U}{\partial z}\Big)_{z=-h_0} = \frac{1}{2} f_w u_0 U_b \tag{4}$$

For the steady case, most undertow solutions specify the depth integrated volume flux Q as a second boundary condition. Normally, that will also be the appropriate condition for the unsteady case we are looking at here. This requires, however, that we determine Q and $\bar{\zeta}$ either from a 2D numerical model (see e.g. List, 1992) or from an analytical solution for the long wave pattern (see e.g. Symonds *et al.* (1982) or Schaffer & Svendsen (1988)). In the present paper, this complication is avoided by using as the second boundary condition the shear stress τ_s at the mean water level. This τ_s is related to the derivative of the velocity profile by

$$\tau_s = \rho\, \nu_t \frac{\partial U}{\partial z} \tag{5}$$

which thus constitutes the second boundary condition for (1).

3 SOLUTION PROCEDURE

All shore-wave-averaged quantities f in the surf-zone are written as

$$f(x,z,t) = f_0(x,z) + f_1(x,z,t) \tag{6}$$

where the subscript 0 and 1 refer to the steady and unsteady (infragravity) parts respectively. Thus, for example, the steady set-up $\overline{\zeta_0}$ corresponds to the set-up caused by the mean short-wave motion, the unsteady part $\overline{\zeta_1}$ to the surface elevation in the infragravity wave motion. The same applies to the velocity U and the surface shear stress τ_s.

Substituting (6) into (1) and separating into steady and unsteady parts by assuming $T_{\text{group}} \gg T_{\text{short}}$ leads to

$$\frac{\partial}{\partial z}\left(\nu_t \frac{\partial U_0}{\partial z}\right) = g\frac{d\overline{\zeta_0}}{dx} + \left(\overline{u_w \frac{\partial u_w}{\partial x}}\right)_0 \tag{7}$$

and

$$\frac{\partial U_1}{\partial t} - \frac{\partial}{\partial z}\left(\nu_t \frac{\partial U_1}{\partial z}\right) = -g\frac{d\overline{\zeta_1}}{dx} - \left(\overline{u_w \frac{\partial u_w}{\partial x}}\right)_1 \tag{8}$$

The corresponding boundary conditions are

At mean water level ($z = \overline{\zeta_0}$)

$$\nu_t \frac{\partial U_0}{\partial z} = \frac{\tau_{s,0}}{\rho} \tag{9}$$

$$\nu_y \frac{\partial U_1}{\partial z} = \frac{\tau_{s,1}}{\rho} \tag{10}$$

At the bottom ($z = -h_0$)

$$\nu_t \frac{\partial U_0}{\partial z} = \frac{1}{2} f_w \, u_0 U_{0b} \tag{11}$$

$$\nu_t \frac{\partial U_1}{\partial z} = \frac{1}{2} f_w u_0 U_{1b} \tag{12}$$

Equation (7) subject to (9) and (11) is the usual undertow problem inside the surf-zone. The solution to this problem has been analyzed extensively in the literature and will be assumed known and not discussed further here. We will concentrate on solving (8) subject to (10) and (12) which means determining the vertical variation of the velocity for infragravity wave motion.

In (10) the term $\tau_{s1}(x,t)$ in the surface boundary condition represents the time and space variation above the mean water level of the radiation stress due to the wave height variation (groupiness). In (8), the $\overline{(u_w \partial u_w/\partial x)_1}$ term represents the equivalent variation of the radiation stress between the bottom and the mean water level. Hence, both these terms are in phase with the short wave height variation. In contrast, the $\partial\overline{\zeta_1}/\partial x$ term in (8) represents the surface elevation gradient in the long wave motion which, in general, will not be in phase with (or even phase locked to) the short wave height variation because it consists of the sum of the bound long wave motion (which is phase locked) and the free long wave motion (which can have any phase relative to the short wave variation).

The solution is developed by assuming each of the variables U_1, ζ_1, $\tau_{s,1}$ and $\overline{\left(u_w \frac{\partial u_w}{\partial x}\right)_1}$ have in principle the form

$$F(x,z,t) = F_i(x,z)\exp(-i\omega t) \tag{13}$$

though F_i for $\overline{\left(u_w \frac{\partial u_w}{\partial x}\right)_1}$ is assumed independent of z. The complex F_i includes the phase of each variable.

If we define the parameter

$$\beta = \sqrt{\frac{\omega}{2\nu_t}}$$

then the results for U_1 become (after extensive algebra)

$$U_1 = \frac{F_a}{\omega}\left\{\cos(\omega t) + \frac{\sqrt{2}T_s\beta}{\rho F_a}F_2(z)\cos\left[\omega t - \phi_B - \phi_{z2}(z)\right]\right.$$
$$\left. + \frac{f_w u_0}{2\nu_t\beta}\frac{\omega}{F_a}U_{1b}F_3(z)\cos\left[\omega t - \phi_D - \phi_3(z)\right]\right\} \qquad (14)$$

In the above $t = 0$ is chosen to correspond to the time when the entire right hand side of (8) attains its maximum, the value of which is termed F_a. (For details, see Putrevu & Svendsen (1993) which also gives the values of the other parameters in (14)).

4 RESULTS

4.1 Velocity Profiles

An analysis of (14) reveals that essentially there are three important parameters that influence the solution. They are βh, $T_s\beta/\rho F_a$ and δ. Here T_s is the amplitude of the (oscillatory) shear stress, τ_{s1}, of the mean water surface. This shear stress represents the surface part of the variation in radiation stress caused by variations in short wave height. τ_{s1} is phase shifted relative to the flow created by the sum of the total long wave motion and the radiation stress variation between bottom and mean water surface (the right hand side of (1) (RHS), which represents the forcing), and δ is a measure of that phase shift. Since RHS is assumed depth uniform, this part of the flow is depth uniform.

The effect of τ_{s1} is to modify the flow created by the RHS of (1). This modification is equivalent to an oscillatory (surface) boundary layer with a thickness parameter β^{-1}. Hence, the parameter $(\beta h)^{-1}$ measure over how large a fraction of the water depth the flow is modified by the surface boundary layer. And, in fact, $(\beta h)^{-1}$ also measures the vertical scale of influence of the bottom shear stress, $\tau_{b,1}$. In view of the relatively complicated solution (14) for the temporal variation of the vertical profiles, the most illustrative approach for examining the results is to select two typical situations and choose values of the three parameters based on a quantitative estimate of their magnitude in those two situations.

The first of the two situations considered in the following represents a short wave motion in the surf zone with virtually no variation in wave height. This means there is no generation of infragravity motion in the surf zone, all long wave motion is free wave motion incident from somewhere else. In consequence, T_s is very small, and F_a is dominated by the $\partial\bar{\zeta}_1/\partial x$ of the free long wave motion ($T_s\beta/\rho F_a = 0.01$). With realistic estimates of ν_t ($0.01h\sqrt{gh}$) and a group period of $T\sqrt{g/h} = 100$ we get $\beta h = O(1)$. Hence the effect of the surface as well as the bottom shear stresses cover nearly the entire depth.

The resulting flow is the sum of the steady undertow U_0 and an almost depth uniform U_1 (Fig. 1): The infragravity part of the total velocity is almost constant over depth as one should expect. This also implies that the value of δ, the phase between the depth uniform forcing (free long wave) and the surface shear stress, makes no difference.

In the second situation, there is a moderate modulation of the mean short wave height of $\pm$ 10%. Whereas this does not change F_a significantly, T_s is now noticeable and $T_s\beta/\rho F_a = 2$.

The phase angle δ can take any value because the infragravity wave is reflected from the shoreline and hence essentially is a standing wave, whereas the short wave motion and its variation propagates toward the shore. Thus different values of δ may simply occur at different positions.

As Figs. 2a–2d show the resulting velocity profiles are very different from the depth uniform motion normally associated with long waves. The four parts of this figure corresponds to $\delta = 0,\ \pi/3,\ 2\pi/3$ and π respectively. It is seen that there are even times where significant velocities occur in opposite directions at the surface and the bottom at the same time.

4.2 Dispersive Mixing

On a long straight coast it has been found that the primary source of lateral mixing is caused by cross-shore transfer of longshore momentum (see Svendsen & Putrevu 1994). This dispersive mixing is provided by the cross shore circulation and is usually 20–50 times stronger than the lateral mixing caused by breaker turbulence. The mixing coefficient D_c is given by

$$D_c = \frac{1}{h}\int_{-h_0}^{\bar{\zeta}} U \int_z^{\bar{\zeta}} \frac{1}{\nu_t} \int_{-h_0}^{z} U dz dz dz \tag{15}$$

where U is the undertow velocity. In the situations studied here where U changes substantially with time (15) results in an equivalent time variation of D_c. Figure 3 shows the variation of D_c over a long wave period for the case analyzed in Fig. 2. The constant value of $D_c \approx 0.2$ represents the value of D_c for the average (i.e. steady undertow) profile. The other curves are for each of the four situations in Fig. 2. It is clear that not only is there a noticeable variation of D_c over a long wave period, but the mean value is also much larger than in the steady case with the same mean cross-shore circulation.

5 SUMMARY AND CONCLUSIONS

In this paper we have presented an analysis of the vertical variation of the particle velocity in periodic infragravity motion.

For the case of surf-beat due to normally incident wave groups on a long beach, an analytical solution was presented for the velocity profiles for a combination of free and forced infragravity waves. Combined with the steady undertow profile inside the surf-zone this represents the long wave and current velocity inside the surf-zone.

The results show that the vertical structure of the velocity profiles depends strongly on whether the infragravity waves are predominately free waves or a combination of free and forced waves.

Under free infragravity waves, the velocity profiles show relatively minor variations over depth and are generally in line with what one expects in long waves. Forced infragravity velocity profiles, on the other hand, show substantial vertical structure.

The dispersion coefficient which controls the cross-shore distribution of the longshore infragravity velocity field was shown to have substantial variation over the period of the infragravity waves and was found also to have a substantial spatial variation across the surf-zone.

6 ACKNOWLEDGEMENTS

This work is a result of research sponsored partly by NOAA Office of Sea Grant, Department of Commerce, under Grant No. NA86AA-D-SG040 (Project No. R/OE-6; and partly by the U.S. Army Research Office, University Research Initiative under contract P- 32686-GS-AAS.

7 REFERENCES

Elgar, S., Herbers, T.H.C., Okihiro, M., Oltman-Shay, J. and Guza, R.T. 1992. Observations of infragravity waves. *Journal of Geophysical Research*, 97, pp. 15573–15577.

Guza, R.T. and Thornton, E.B. 1982. Swash oscillations on a natural beach. *Journal of Geophysical Research*, 87, pp. 483–491.

Herbers, T.H.C., Elgar, S., Guza, R.T. and O'Reilly, W.C. 1992. Infragravity frequency motions on the shelf. *Proceedings of the 23rd Coastal Engineering conference*, pp. 846–859.

Howd, P.A., Oltman-Shay, J. and Holman, R.A. 1981. Wave variance partitioning in the trough of a barred beach. *Journal of Geophysical Research*, 96, pp. 12781–12795.

List, J.H. 1992. A model for the generation of two dimensional surf beat. *Journal of Geophysical Research*, 97, C4, pp. 5623–5635.

Oltman-Shay, J. and Guza, R.T. 1987. Infragravity edge wave observations on two California beaches. *Journal of Physical Oceanography*, 17, pp. 644–663.

Putrevu, U. and Svendsen, I.A. 1992. A mixing mechanism in the nearshore. *Proceedings of the 23rd Coastal Engineering Conference*, pp. 2758–2771.

Putrevu, U. and Svendsen, I.A. 1993. Infragravity velocity profiles in the surf-zone. *Submitted for publication.*

Schaffer, H.A. and Svendsen, I.A. 1988. Surf beat generation on a mild slope beach. *Proceedings of the 21st International Conference on Coastal Engineering*, pp. 1058–1072.

Svendsen, I.A. and Lorenz, R.S. 1989. Velocities in combined undertow and longshore currents. *Coastal Engineering*, 13, pp. 55–79.

Svendsen, I.A. and Putrevu, U. 1994. Nearshore mixing and dispersion. *Proceedings of the Royal Society, London*, A445, pp. 1–16.

Symonds, G., Huntley, D.A. and Bowen, A.J. 1982. Two dimensional surf-beat: Long wave generation by a time-varying break point. *Journal of Geophysical Research*, 87, pp. 492–498.

Wright, L.D., Guza, R.T. and Short, A.D. 1982. Dynamics of a high energy dissipative surf-zone. *Marine Geology*, 45, pp. 41–62.

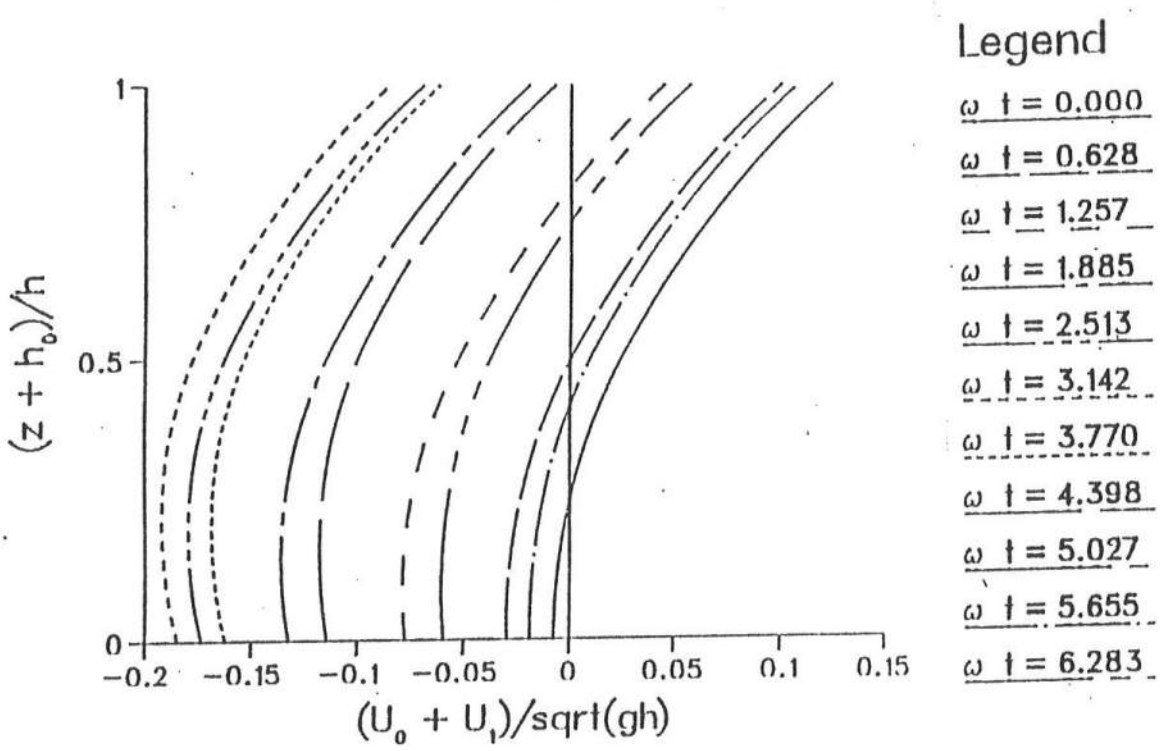

Figure 1: Total short wave averaged velocity field inside the surf-zone for $\sqrt{2T_s\beta/\rho F_a}$= 0.01, $\beta h = 1.5$ and $F_a/(\omega\sqrt{gh}) = 0.1$. This corresponds to a case with little short wave variability in the surf zone. Hence the local generation of long wave energy is small and the infragravity waves are almost exclusively free long waves.

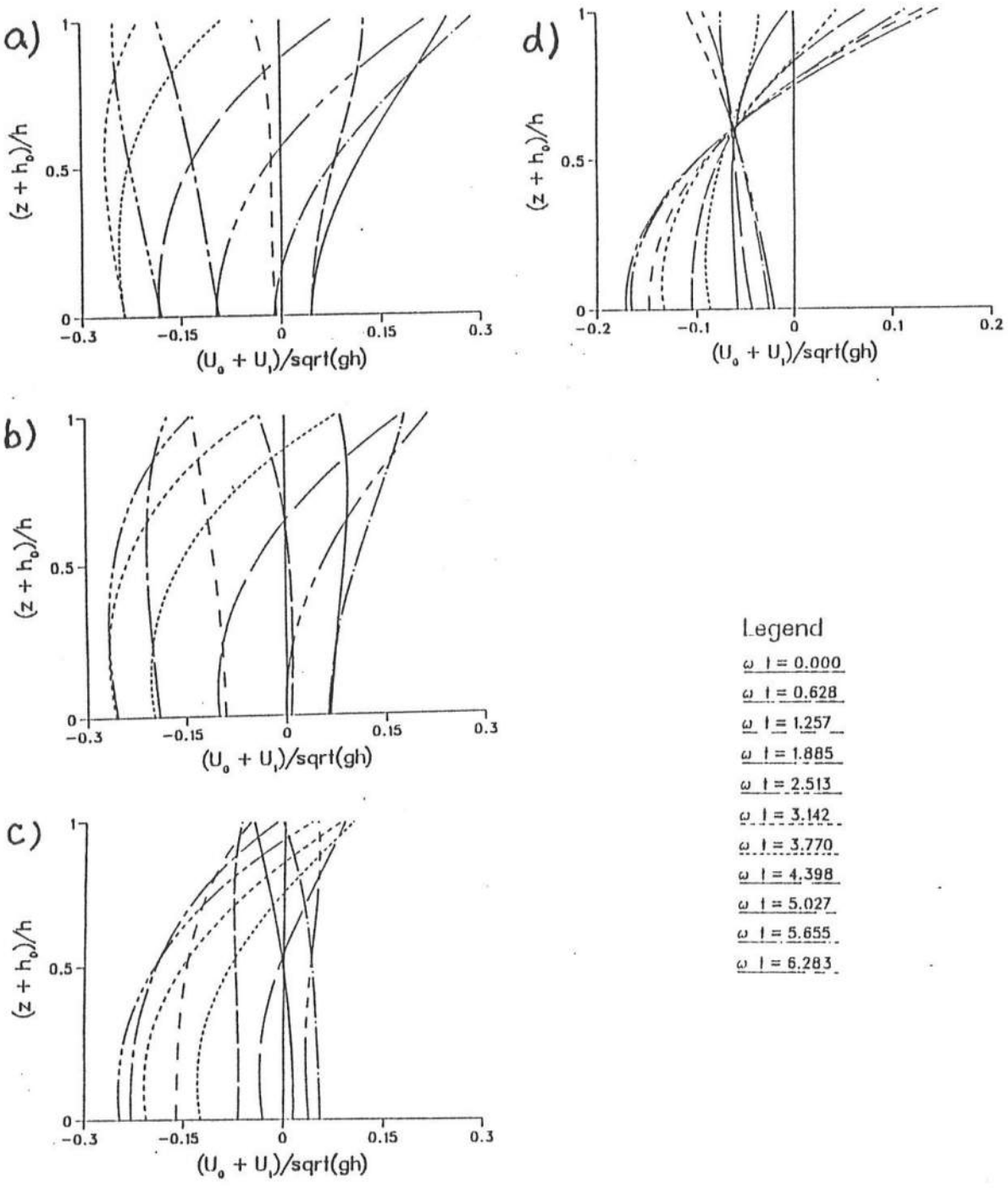

Figure 2: Total short wave averaged velocity field inside the surf- zone for $\sqrt{2}T_s\beta/(\rho F_a) = 2$, $\beta h = 1.5$ and $F_a/(\omega\sqrt{gh}) = 0.1$. This corresponds to a case with about $\pm$ 10% variation in short wave height inside the surf zone and a moderate incident free long wave motion. The total infragravity wave is a combination of free and boundary waves. (a-d) show the velocity profiles over a long wave period for different phase angles between the total long wave motion and the variation of the short wave height.

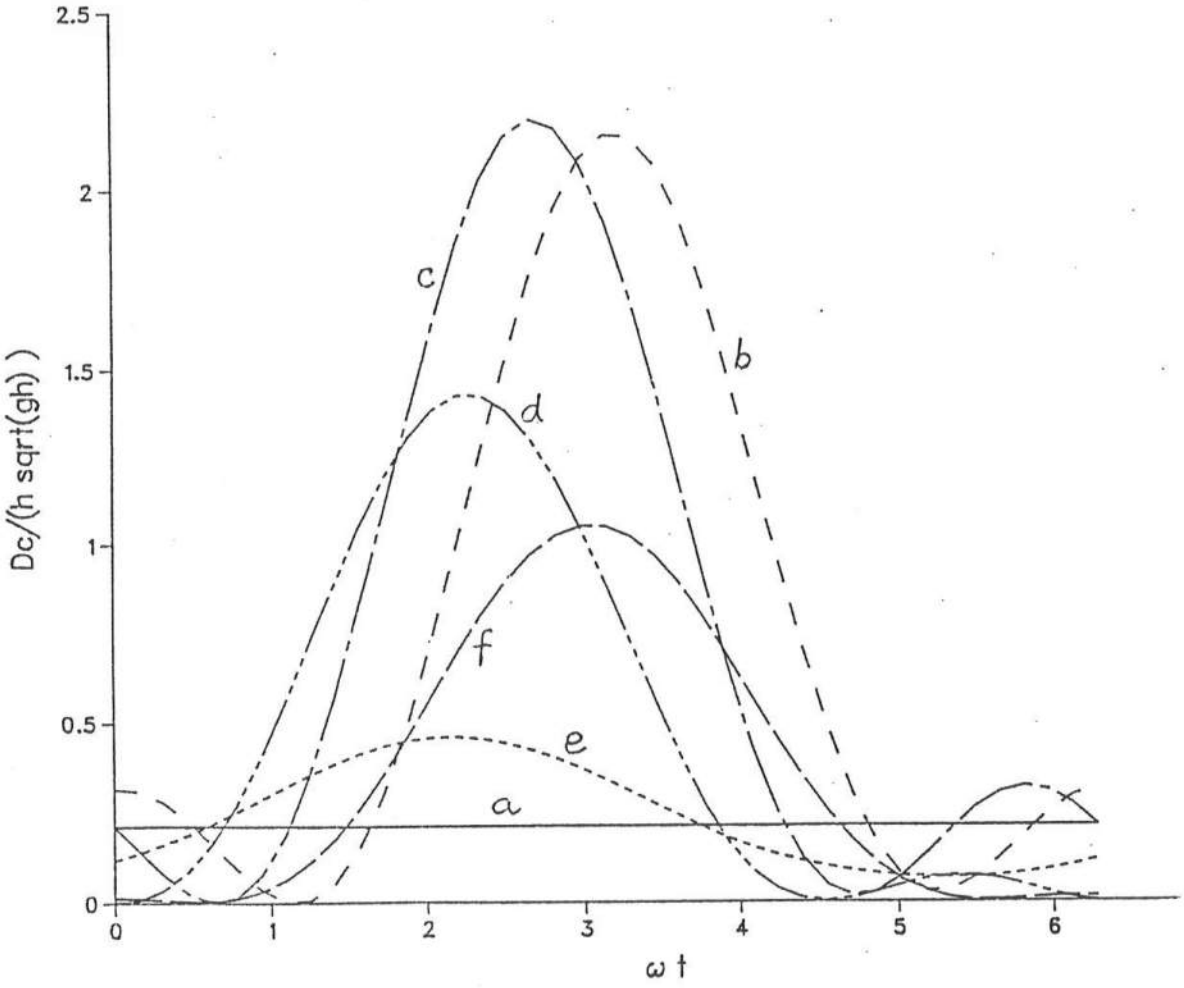

Figure 3: Temporal variation of the dispersion coefficient: a) Dispersion coefficient due to steady undertow; b) Dispersion coefficient due to velocity profiles of figure 2a; c) Dispersion coefficient due to velocity profiles of figure 2b; d) Dispersion coefficient due to velocity profiles of figure 2c; and e) Dispersion coefficient due to velocity profiles of figure 2d; f) Dispersion coefficient corresponding to profiles in Figure 1.

NUMERICAL MODELLING OF SOLITARY WAVE BREAKING, RUNUP AND REFLECTION

Entin A. Karjadi and Nobuhisa Kobayashi
Center for Applied Coastal Research
University of Delaware
Newark, DE 19716, USA

ABSTRACT

A numerical model for breaking solitary waves is developed by expanding the available one-dimensional time-dependent model which has been used succesfully to predict regular and irregular wave dynamics on slopes. For an efficient comparison of the expanded model with a large number of available laboratory tests on smooth uniform slopes, the dimensionless parameters involved in the problem are identified using the normalized governing equations and incident solitary wave profile. The representative solitary wave period and associated surf similarity parameter are introduced to examine the similarity and difference between solitary and regular waves. The breaking, runup and reflection of solitary and regular waves are qualitatively similar in terms of the surf similarity parameter. For given surf similarity parameter, breaking solitary wave runup is definitely larger than breaking regular wave runup which is affected by the interaction between wave uprush and downrush. The expanded numerical model is shown to be capable of predicting the normalized wave runup as a function of the surf similarity parameter.

INTRODUCTION

Solitary wave runup has been studied in relation to coastal flooding and damages caused by tsunamis, whereas regular and irregular wave runup has been investigated for the design of coastal structures against wind waves. Although these two problems are related, separate empirical and numerical methods are generally used to predict wave runup partly because solitary waves do not have specific wave periods.

Kobayashi and Watson (1987) developed a numerical model based on the nonlinear shallow water wave equations. This model has been used succesfully to predict regular wave dynamics on slopes. This model is expanded herein for solitary waves by introducing a rep-

resentative solitary wave period on the basis of the normalized solitary wave profile. The representative wave period and associated surf similarity parameter are then used to facilitate the comparisons of the characteristics of solitary and regular waves.

An emphasis is placed on runup of breaking solitary waves since runup of nonbreaking solitary waves is better understood theoretically (*e.g.*, Synolakis, 1987a) and may be predicted well by numerical models based on potential flow theory. Moreover, unlike Hunt's formula for predicting runup of breaking monochromatic waves on smooth uniform slopes (Battjes, 1974; Ahrens and Martin, 1985), no general empirical formula exists for breaking or broken solitary wave runup.

Numerical models based on potential flow theory are not applicable to broken waves. Boussinesq wave models such as a Lagrangian finite-element model (Zelt, 1991), which include nonhydrostatic pressure correction, may be used to predict runup of broken solitary waves if the effects of wave breaking and bottom friction are included empirically. However, it is not obvious whether the nonhydrostatic pressure correction based on the potential flow assumption of weakly nonlinear and relatively long waves is really valid for broken solitary waves. In any case, the present numerical model is probably the simplest time-dependent, one-dimensional model for predicting the nonlinear breaking or broken solitary waves characteristics on the slopes.

To assess the capability of the expanded numerical model, comparisons are made with the laboratory data of breaking solitary wave runup (Synolakis, 1987a). The model with a limited calibration of the bottom friction factor is shown to be in good agreement with the data. In terms of the surf similarity parameter the characteristics of the computed solitary wave breaking, decay and reflection are shown to be qualitatively similar to those of regular waves (Battjes, 1974).

NUMERICAL MODEL

Governing Equations

The numerical model developed herein is based on the depth-integrated continuity and horizontal momentum equations (Kobayashi and Watson, 1987). The two-dimensional coordinate system is defined as follows: x' = horizontal coordinate taken to be positive in the landward direction with $x' = 0$ at the toe of a smooth slope with a constant angle θ' from the horizontal; z' = vertical coordinate taken to be positive upward with $z' = 0$ at the still water level (SWL). The prime indicates the dimensional variables. The instantaneous free surface is located at $z' = \eta'$, and the instantaneous water depth is denoted by h'. The smooth uniform slope is located at $z' = (x' \tan\theta' - d_t')$ in which d_t' = water depth below SWL at the toe of the slope. Assuming the vertical pressure distribution to be approximately hydrostatic, the governing equations may be expressed as

$$\frac{\partial h'}{\partial t'} + \frac{\partial}{\partial x'}(h'u') = 0 \tag{1}$$

$$\frac{\partial}{\partial t'}(h'u') + \frac{\partial}{\partial x'}(h'u'^2) = -gh'\frac{\partial \eta'}{\partial x'} - \frac{\tau_b'}{\rho} \tag{2}$$

where t' = time; u' = depth-averaged horizontal velocity; τ_b' = bottom shear stress; ρ = fluid density that is assumed constant; and g = gravitational acceleration. The bottom shear stress may be expressed as

$$\tau_b' = \frac{1}{2} f' |u'| u' \tag{3}$$

where f' = bottom friction factor which is assumed constant.

The following dimensionless variables and parameters are introduced to normalize (1) and (2):

$$t = \frac{t'}{T'}; x = \frac{x'}{T'\sqrt{gH'}}; u = \frac{u'}{\sqrt{gH'}}; z = \frac{z'}{H'}; h = \frac{h'}{H'} \tag{4}$$

$$\eta = \frac{\eta'}{H'}; d_t = \frac{d_t'}{H'}; \sigma = T'\sqrt{\frac{g}{H'}}; \theta = \sigma \tan\theta'; f = \frac{1}{2}\sigma f' \tag{5}$$

where T' = representative wave period and H' = incident solitary wave height at $x = 0$; σ = ratio between the horizontal and vertical length scales; θ = normalized gradient of the slope; and f = normalized bottom friction factor. The present numerical model assumes that $\sigma^2 \gg 1$ and $(\cot\theta')^2 \gg 1$ (Kobayashi and Wurjanto, 1992). In terms of the normalized coordinate system, the smooth uniform slope is located at $z = (\theta x - d_t)$ for $x \geq 0$. Substitution of (4) and (5) into (1) and (2) yields

$$\frac{\partial h}{\partial t} + \frac{\partial}{\partial x}(hu) = 0 \tag{6}$$

$$\frac{\partial}{\partial t}(hu) + \frac{\partial}{\partial x}(hu^2 + \frac{1}{2}h^2) = -\theta h - f|u|u \tag{7}$$

Eqs. (6) and (7) are solved numerically in the time domain to obtain the variations of h and u with respect to t and x for given θ and f (Kobayashi and Karjadi, 1993).

The surf similarity parameter ξ, which has been used successfully to describe the characteristics of regular waves on uniform slopes (Battjes, 1974), is given by $\xi = \theta/\sqrt{2\pi}$ and proportional to the normalized slope gradient θ. The normalization of (1) and (2) using T' and H' clearly shows that ξ expresses the normalized slope effect in (7).

Solitary Wave Profile and Representative Wave Period

Solitary wave theory corresponds to cnoidal wave theory as the Ursell parameter U_r approaches infinity. In the numerical model, the normalized incident solitary wave profile $\eta_i(t)$ at $x = 0$ is derived by normalizing the dimensional solitary wave profile using (4) and (5) and is given by (Kobayashi and Karjadi, 1993)

$$\eta_i(t) = \text{sech}^2[K(t - t_c)] \quad \text{for } t \geq 0 \tag{8}$$

with

$$K = \frac{\sqrt{3}\,\sigma}{2\,d_t}\left(1 + \frac{1}{d_t}\right)^{\frac{1}{2}} \tag{9}$$

in which t_c = normalized arrival time of the solitary wave crest such that $\eta_i = 1$ at $t = t_c$; and K = solitary wave parameter.

In order to estimate the representative wave period T', the unit duration $(t_c - 0.5) \leq t \leq (t_c + 0.5)$ about the crest arrival time t_c may be selected such that $\eta_i(t) \geq \delta_i$ in this unit duration where δ_i is a small parameter. Substituting this requirement into (9) yields K as a function of δ_i

$$K = 2\, ln \left(\sqrt{\frac{1}{\delta_i}} + \sqrt{\frac{1}{\delta_i} - 1} \right) \tag{10}$$

which yields $K = 3.64, 4.36$ and 5.99 for $\delta_i = 0.1, 0.05$ and 0.01, respectively. For given d_t, K given by (9) is proportional to σ defined in (5) and hence the representative wave period T'. The computed results for $\delta_i = 0.1, 0.05$ and 0.01 in the report of Kobayashi and Karjadi (1993) have indicated that the choice of δ_i does not effect the essential results presented hereafter for $\delta_i = 0.05$. The crest arrival time t_c in (8) is taken as $t_c = 1$ since (8) yields $\eta_i(t = 0) = 0.00066$ for $t_c = 1$ and $\delta_i = 0.05$. The initial time $t = 0$ may hence be regarded as the time when the incident solitary wave arrives at $x = 0$. In addition, the computed temporal variations starting from the initial time $t = 0$ can be interpreted easily. In summary, $\eta_i(t)$ given by (8) with $t_c = 1$ and $K = 4.36$ ($\delta_i = 0.05$) is the same for any solitary wave, and σ computed using (9) is used to estimate T' for given d_t.

Computer Program

Kobayashi and Karjadi (1993) developed a computer program called SBREAK to solve (6) and (7) numerically. The incident solitary wave at the seaward boundary of the computation domain given by (8) needs to be specified as input. The variations of h and u are computed as a function of t and x starting from $t = 0$ when no wave action is present in the region $x \geq 0$. The normalized reflected wave profile $\eta_r(t)$ at the toe of the slope is computed from the characteristics advancing seaward (Kobayashi *et al.*, 1987).

The computation duration is taken to be long enough to simulate at least the entire process of wave uprush and the resulting runup. The numerical method as well as the seaward and landward boundary conditions are the same as those used by Kobayashi *et al.* (1987). The dimensionless parameter involved in this problem are $\xi = \theta/\sqrt{2\pi}, d_t$ and $f = 0.5\sigma f'$ where σ is given by (9). Alternatively, ξ, d_t and f' are selected as the three independent parameters since the assumption of constant f' for given slope roughness has been satisfactory in previous applications (Kobayashi *et al.*, 1987, 1989).

COMPARISON WITH AVAILABLE DATA

To assess the capability of the expanded numerical model, comparisons are made with the breaking solitary wave data of Synolakis (1987a). For his experiments the assumption of $\sigma^2 \gg 1$ is valid as long as d_t is larger than about 2, for which the incident solitary waves at the toe of the slope are non-breaking (Kobayashi and Karjadi, 1993). If d_t becomes much larger than unity, the dispersive effects neglected in the present model may not be negligible in the region between the toe of the slope and the point of wave breaking. This is one of the reasons that the numerical model is compared herein with only the breaking solitary wave data of Synolakis (1987a).

Synolakis (1987a) conducted a series of laboratory experiments using a uniform slope of $\cot\theta' = 19.85$ constructed of aluminum panels with a hydraulically smooth surface. The wave generator produced near-perfect solitary waves. The wave heights in the constant depth region measured by resistance-type wave gages are assumed herein to be the same as the incident solitary wave heights H' at the toe of the slope. The runup gage consisted of array of capacitance probes whose tips were 1 mm from the bottom surface. The measured maximum runup R' may hence be assumed to correspond to the maximum value of η' at the location where the instantaneous physical water depth $h' = 1$ mm. The computed normalized runup $R = R'/H'$ has been shown to be not very sensitive to this water depth (Kobayashi and Karjadi, 1993).

Synolakis (1987a) tabulated 77 tests with $d_t = 1.58-200, \sigma = 6.22-1004, R = 1.28-4.56$ and $\xi = 0.125 - 20.2$ for which the assumption of $\sigma^2 \gg 1$ made in the numerical model is satisfied. In his experiments, breaking on the slope occurred during backwash when $d_t < 22.7$ ($\xi < 2.25$) and during uprush when $d_t < 18.2$ ($\xi < 1.79$). These conditions are similar to the conditions of $\xi \lesssim 2.3$ for regular wave breaking (Battjes, 1974) which is affected by both uprush and backwash. For 43 tests, wave breaking occurred on the slope during wave uprush.

The use of the surf similarity parameter for solitary waves allows the comparisons between solitary and monochromatic waves. Hunt's empirical formula gives the relation between R and ξ for breaking monochromatic waves on smooth uniform slopes (Battjes, 1974; Ahrens and Martin, 1985)

$$R = \xi = \frac{\sigma \tan\theta'}{\sqrt{2\pi}} \quad \text{for } 0.1 \lesssim \xi \lesssim 2.3 \tag{11}$$

The dimensionless parameters associated with the numerical model indicate that the normalized runup R for solitary waves depends on ξ and d_t for given slope roughness. The surf similarity parameter ξ includes the effects of both $\tan\theta'$ and σ where σ depends on d_t in view of (9) and (10) for given δ_i. The normalized runup of breaking solitary waves on smooth uniform slopes may be assumed to be a function of ξ only provided that the normalized water depth at the toe, d_t, is sufficiently large and its direct effect on R is negligible. The relationship between R and ξ fitted to the 43 tests for solitary wave breaking during uprush is expressed as (Kobayashi and Karjadi, 1994)

$$R = 2.955\xi^{0.395} \quad \text{for } 0.125 \leq \xi \leq 1.757 \tag{12}$$

The empirical formula (12) is as good as the formula $R = 1.109 d_t^{0.418}$ proposed by Synolakis (1987a) for his breaking solitary wave data. The advantage of (12) is that it may not be limited to the 1:19.85 smooth slope only.

The numerical model is compared with 9 tests out of 43 tests of Synolakis(1987a) for breaking solitary wave runup. The 9 tests are selected to represent the range of parameters for the 43 tests, *i.e.*, $d_t = 1.58 - 17.9, \sigma = 6.22 - 87.4, \xi = 0.125 - 1.757$, and $R = 1.28 - 3.70$. Two values of the bottom friction factor $f' = 0.01$ and $f' = 0.005$ are assumed. The value of $f' = 0.01$ was the lower bound for the plywood slope used by Kobayashi and Watson (1987). The aluminum slope used by Synolakis (1987a) must have had a smaller friction factor since it was smoother than plywood. As expected, the value of $f' = 0.01$ slightly underpredicts the normalized runup R. The value of f' is then reduced to $f' = 0.005$ in the hope of better agreement. The measured and computed values of R with $f' = 0.01$ and $f' = 0.005$ are

shown in Table 1 as a function of ξ, together with the empirical formula $R = 2.955\xi^{0.395}$ where Hunt's formula for breaking regular wave runup is given by $R = \xi$. Table 1 shows that the values of $f' = 0.01$ and $f' = 0.005$ give the approximate lower and upper bounds of the 43 measured R, respectively. As a result, the value of $f' = 0.006$ or 0.007 should give very good agreement with the data. Table 1 also indicates that for given surf similarity parameter, breaking solitary wave runup definitely larger than breaking regular wave runup which is affected by the interaction between regular wave uprush and downrush on the slope. Comparisons of the computed results using $f' = 0.01$ and $f' = 0.005$ show that the reflected wave profile η_r at the toe of the slope is affected very little by f' and that the increase of f' reduces wave runup noticeably.

As an example, the computed results for test 32 with $\xi = 0.591$ and $f' = 0.005$ are discussed briefly in the following. Figs. 1 and 2 show the spatial variations of the maximum, mean and minimum values of the normalized free surface elevation η and the normalized depth-averaged velocity u, respectively. The spatial variation of the maximum normalized free surface elevation, $\eta_{\max}$, seaward of the still water shoreline is qualitatively similar to the analyzed data presented by Synolakis and Skjelbreia (1993). In the wave uprush zone landward of the still water shoreline, the water depth below the approximately straight envelope of $\eta_{\max}$ decreases gradually. Near the still water shoreline, the computed velocities of uprushing and downrushing water are very large and the mean velocity is negative as has been shown for monochromatic waves by Kobayashi *et al.* (1989). To examine the solitary wave evolution on the uniform slope, the spatial variations of the computed free surface elevation η and the depth-averaged velocity u are plotted at $t = 1$ to $t = 8$ in Fig. 3. The incident solitary wave appears to be breaking at $t = 2$. At $t = 4$, the tip of uprushing water moves upslope while the rest of the water flows seaward. The maximum runup occurs around $t = 4.5$. Wave breaking during the downrush is apparent at $t = 6$.

To elucidate the effects of the surf similarity parameter ξ on the solitary wave dynamics on uniform slopes, the computed results for $\xi = 0.125$ (test 23), 0.591 and 1.757 (test 40) using $f' = 0.005$ are plotted in the same figures. The computed incident and reflected wave profiles at $x = 0$ are plotted in Fig. 4. The spatial variation of the normalized maximum free surface elevation $\eta_{\max}$ corresponding to the envelope of the solitary wave crest is plotted in Fig. 5. Fig. 4 shows that the increase of ξ leads to the increase in the magnitude of wave reflection which is qualitatively similar to the reflection of breaking regular waves (Battjes, 1974). Fig. 4 also shows the decrease of wave reflection duration with the increase of ξ. The temporal variations of reflected waves are similar to the measured variations presented by Synolakis (1987b). Fig. 5 shows that the region of wave decay becomes narrower as ξ is increased. It is apparent in Fig. 5 that the normalized slope gradient θ increases with the increase of ξ.

CONCLUSIONS

Introduction of a representative solitary wave period has been shown to allow the development of the one-dimensional time-dependent numerical model for breaking solitary waves by expanding the existing model for regular and irregular waves on slopes. The modified numerical model has been shown to be capable of predicting breaking or broken solitary wave

runup with a limited calibration of the bottom friction factor. The surf similarity parameter for solitary waves on slopes is shown to be useful in interpreting the breaking solitary wave characteristics in comparison with the regular wave characteristics.

ACKNOWLEDGEMENT

This study was supported by the National Science Foundation under Grant No. BCS-9111827.

REFERENCES

Ahrens, J.P. and Martin, F.T. (1985). "Wave runup formulas for smooth slopes." *J. Wtrway. Port Coast. and Oc. Engrg.*, ASCE, 111(1), 128-133.

Battjes, J.A. (1974). "Surf similarity." *Proc.* 14^{th} *Coast. Engrg. Conf.*, ASCE, 1, 466-480.

Kobayashi, N., DeSilva, G.S. and Watson, K.D. (1989). "Wave transformation and swash oscillations on gentle and steep slopes." *J. Geophys. Res.*, 94(C1), 951-966.

Kobayashi, N. and Karjadi, E.A. (1993). "Documentation of computer program for predicting long wave runup." *Res. Rpt. CACR-93-03*, Ctr. for Applied Coast. Res., Univ. of Delaware, Newark, DE.

Kobayashi, N. and Karjadi, E.A. (1994). "Surf similarity parameter for breaking solitary wave runup." *J. Wtrway. Port Coast. and Oc. Engrg.*, ASCE (in press).

Kobayashi, N., Otta, A.K. and Roy, I. (1987). "Wave reflection and runup on rough slopes." *J. Wtrway. Port Coast. and Oc. Engrg.*, ASCE, 113(3), 282-298.

Kobayashi, N. and Watson, K.D. (1987). "Wave reflection and runup on smooth slopes." *Proc. Coast. Hydrodynamics*, ASCE, 548-563.

Kobayashi, N. and Wurjanto, A. (1992) "Irregular wave setup and runup on beaches." *J. Wtrway. Port Coast. and Oc. Engrg.*, ASCE, 118(4), 368-386.

Synolakis, C.E. (1987a). "The runup of solitary waves." *J. Fluid Mech.*, 185, 523-545.

Synolakis, C.E. (1987b). "The runup and reflection of solitary waves." *Proc. Coast. Hydrodynamics*, ASCE, 533-547.

Synolakis, C.E. and Skjelbreia, J.E. (1993). "The evolution of the maximum amplitude of solitary waves on plane beaches." *J. Wtrway. Port Coast. and Oc. Engrg.*, ASCE, 119(3), 323-342.

Zelt, J.A. (1991). "The runup of nonbreaking and breaking solitary waves." *J. Coast. Engrg.*, 15, 205-246.

Table 1: Measured and Computed Normalized Runup for 9 Tests.

Test No	ξ	$R = 2.955\xi^{0.395}$	Computed R		Measured R
			$f' = 0.01$	$f' = 0.005$	
7	0.181	1.50	1.28	1.48	1.43
15	1.076	3.04	2.86	3.21	3.00
18	0.298	1.83	1.62	1.87	1.85
21	0.328	1.90	1.70	1.95	1.78
23	0.125	1.30	1.12	1.29	1.33
32	0.591	2.40	2.22	2.55	2.42
37	1.300	3.28	3.13	3.46	3.44
39	1.507	3.48	3.30	3.63	3.51
40	1.757	3.69	3.47	3.84	3.70

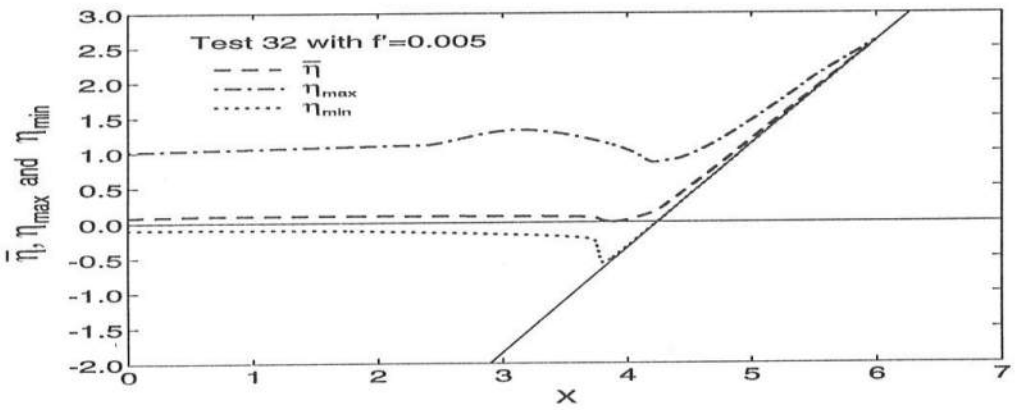

Figure 1: Spatial Variations of Maximum, Mean and Minimum Values of Normalized Free Surface Elevation η for Test 32 with $f' = 0.005$.

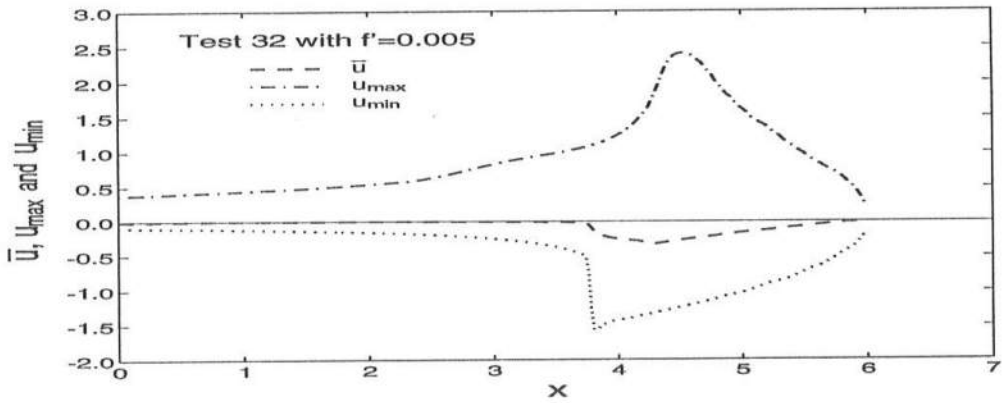

Figure 2: Spatial Variations of Maximum, Mean and Minimum Values of Normalized Depth-Averaged Velocity u for Test 32 with $f' = 0.005$.

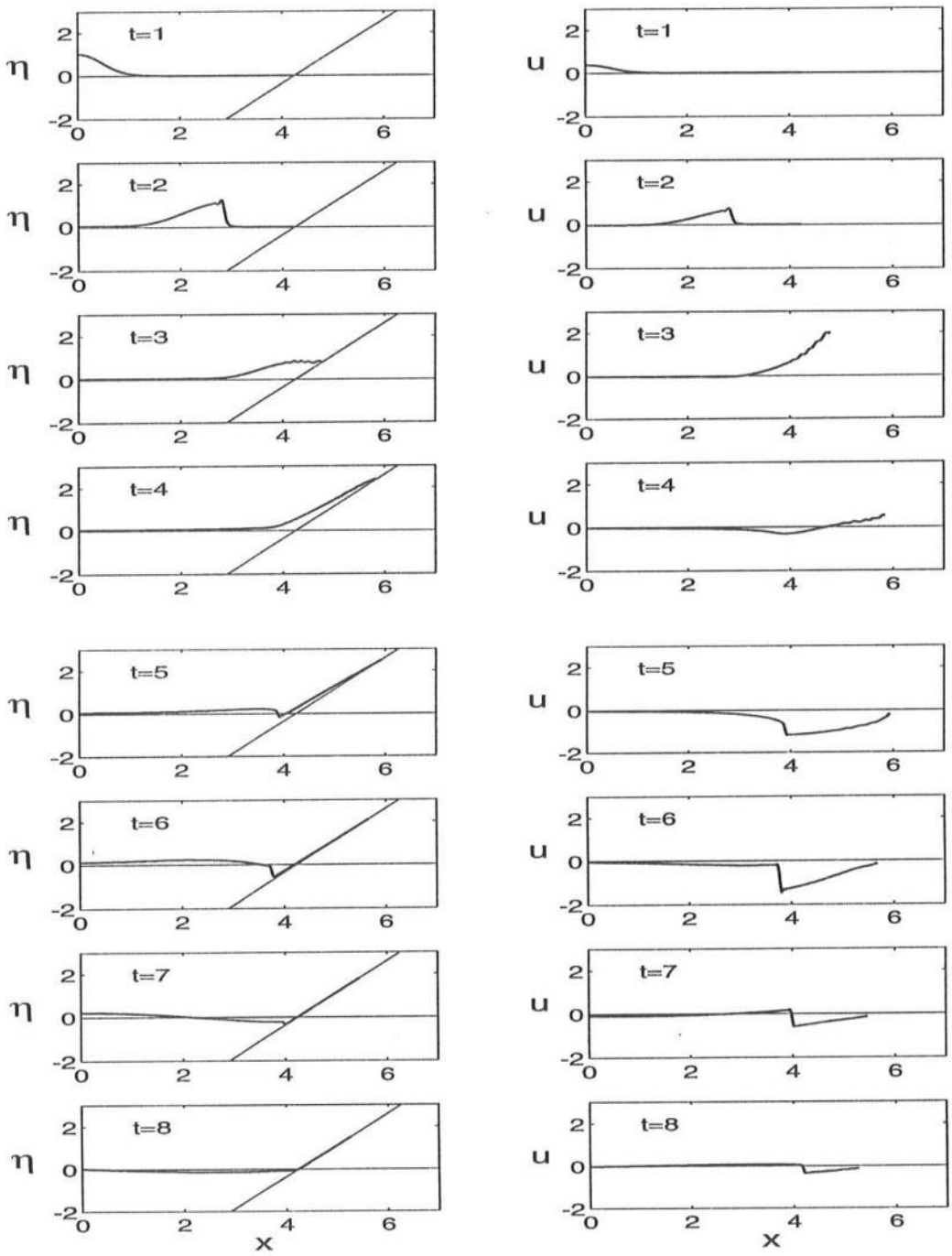

Figure 3: Spatial and Temporal Variations of Normalized Free Surface Elevation η and Depth-Averaged Velocity u for Test 32 with $f' = 0.005$.

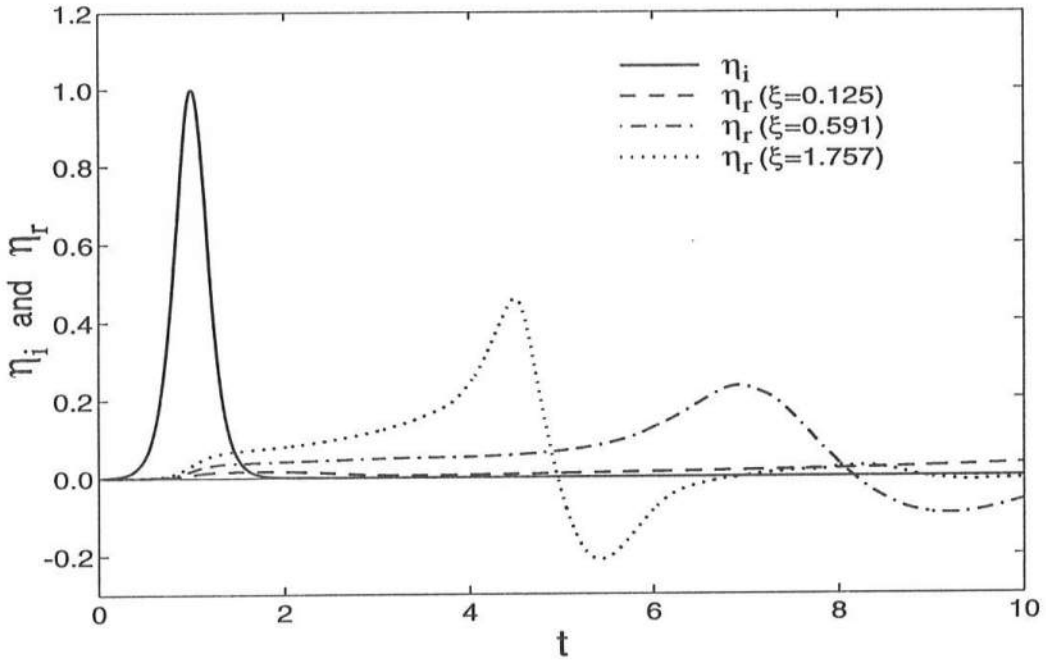

Figure 4: Specified Incident Solitary Wave Profile $\eta_i(t)$ and Computed Reflected Wave Profiles $\eta_r(t)$ at $x = 0$ for $\xi = 0.125, 0.591$ and 1.757.

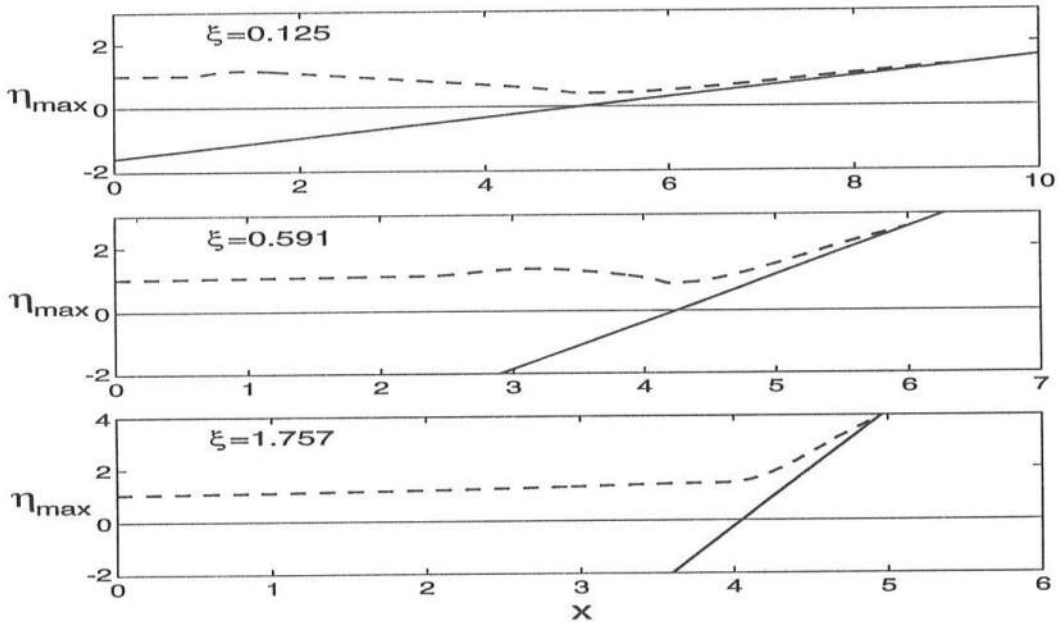

Figure 5: Spatial Variations of Maximum Normalized Free Surface Elevation η_{max} for $\xi = 0.125, 0.591$ and 1.757.

FLOODING OF ROADWAY BETWEEN BAYS DUE TO STORM SURGE AND TIDE

Bradley D. Johnson, Nobuhisa Kobayashi
Center for Applied Coastal Research, University of Delaware
Newark, DE 19716, U.S.A.

and

Keith D. Watson
Coastal Engineering Section, U.S. Army Corps of Engineers
Philadelphia District, Philadelphia, PA 19107-3390, U.S.A.

ABSTRACT

A numerical model for a network of one-dimensional channels is applied to predict flooding of a roadway between relatively small bays due to storm surge and spring tide through an inlet. A small-scale experiment for steady flow over an obstacle was conducted to assess whether a simple term for flow contraction and expansion added to the standard one-dimensional momentum equation is appropriate or not for vertical contraction and expansion. The numerical model with the contraction-expansion coefficient $K = 0.5$ is shown to be capable of predicting the overall free surface variations over the obstacle, although it does not predict well the free surface dip at the crest of the obstacle and the computed discharge may not be very accurate. The numerical model with $K = 0.5$ is then applied to predict the stillwater elevations at the existing and raised roadways for different storms. The computed results indicate that the raised Roadway will not increase the essentially horizontal stillwater elevations in the vicinity of the roadway as a dam in a river might. The computed peak stillwater elevations are compared with limited available data.

INTRODUCTION

For large-scale phenomena such as storm surge and tides, physical modelling is generally expensive and difficult due to scale effects. Numerical models calibrated using field data are hence widely used to simulate large-scale phenomena. However, large-scale numerical models

may not predict local hydraulic phenomena very accurately as compared to physical modelling. As a result, a hybrid approach based on numerical and physical modelling together with field data may be employed to make the best use of available modelling techniques and solve practical problems. Such a hybrid approach is used herein to investigate flooding of a roadway between two bays where one bay is connected to an ocean through an inlet.

Delaware State Route 54, which is simply called the Roadway hereafter, runs between Little Assawoman Bay in Delaware and Assawoman Bay, which are called the North and South Bays, respectively, for brevity. The South Bay is connected to the Atlantic Ocean through the inlet at Ocean City, Maryland as shown in Fig. 1. A relatively narrow connection, called the Ditch, exists between the North and South Bays. The entire area along the Roadway between the North and South Bays is low with an elevation of less than 1 m above the mean sea level. Although the Roadway is supposed to be an evacuation route for the residents along the Roadway and the Atlantic shoreline, even minor storms flood the Roadway, rendering it impassable.

One of the Roadway improvement alternatives considered by the Delaware Department of Transportation is to raise the elevation of the Roadway with fill and a new pavement. The frequency and duration of no vehicle passage on the raised Roadway during storms needs to be predicted to determine an appropriate elevation of the raised Roadway. One of the major concerns of the residents along the Roadway is whether the raised Roadway would increase the stillwater elevations during storms in a manner similar to the backwater effect behind a dam in a river. To address these hydraulic problems, the stillwater elevations on the existing and raised Roadways need to be predicted and compared for storms of different recurrence intervals and different elevations of the raised Roadway.

NUMERICAL MODEL

Because the relatively small bay system shown in Fig. 1 may be regarded as a network of one-dimensional channels, the following one-dimensional continuity and momentum equations without lateral flow and wind (e.g., French, 1985; Amein and Kraus, 1991) may be adopted:

$$\frac{\partial A}{\partial t} + \frac{\partial Q}{\partial x} = 0 \tag{1}$$

$$\frac{\partial Q}{\partial t} + \frac{\partial}{\partial x}\left(\frac{Q^2}{A}\right) = -gA\left[\frac{\partial \eta}{\partial x} + \frac{|Q|Q}{C^2} + \frac{K}{2g}\frac{\partial}{\partial x}\left(\frac{Q}{A}\right)^2\right] \tag{2}$$

with

$$C = \sum_{j=1}^{M} \frac{\alpha}{n_j} A_j R_j^{2/3} \tag{3}$$

in which t = time; x = horizontal coordinate following the channel alignment; A = cross-sectional area; Q = discharge; g = gravitational acceleration; η = water surface elevation which is assumed to be horizontal in the direction normal to the x-axis; C = conveyance; and K = contraction-expansion coefficient. The conveyance C, based on the Manning formula for a composite cross section with M subsections of different roughness and depths, is given by (3) with $\alpha = 1$ for SI units and $\alpha = 1.49$ for English units in which n_j, A_j and R_j are the Manning coefficient, area and hydraulic radius of subsection j, respectively. The mass

conservation equation based on Q and the continuity of the water surface elevation η are applied at each junction of channels. Eqs. (1) and (2) with (3) are solved using the weighted four-point implicit finite difference method employed by Amein and Kraus (1991) together with appropriate initial and boundary conditions.

EXPERIMENT

In order to assess whether the numerical model based on (1) and (2) with a constant value of K can predict the converging and diverging flows over an obstacle such as the Roadway, a steady flow experiment was conducted in a horizontal flume, which was 5 m long, 7.6 cm wide and 25 cm high. An available triangular obstacle was used in the experiment. The triangular obstacle was 5cm high and 37.5 cm long at its base. The side slopes were 1:1.8 and 1:5.7. Three tests were conducted: no obstacle in the flume, with the steeper 1:1.8 slope of the obstacle facing upstream, and the steeper slope of the obstacle facing downstream. The bottom of the flume turned out to be somewhat irregular and could not be used as the datum; therefore the horizontal stillwater level of approximately 8 cm depth in the flume was used as the horizontal datum. At 28 horizontal locations within the fully developed flow region, a point page was used to measure the steady free surface and bottom elevations relative to the datum. The errors of the elevation measurements were estimated to be $\pm$ 0.01 cm. The measured free surface and bottom elevations for the three tests are shown in Fig. 2 where the horizontal coordinate $x = 0$ is located at a distance of 2.2 m from the flume entrance. The relatively small free surface variations are enlarged in Fig. 2 to discern the water level increase upstream of the triangular obstacle and the water level dip in the vicinity of its crest. The discharge measured by a flow meter was $Q = 1.0\ \ell/s$ for the three tests.

For the numerical computation, the measured steady free surface elevations at $x = 0$ and $x = 260$ cm are specified as the upstream and downstream boundary conditions. The measured steady free surface elevations and discharge in the computation domain $0 < x < 260$ cm are specified as the initial conditions of the time-dependent numerical model so as to obtain the steady flow solution corresponding to the specified boundary conditions in an efficient manner. The computed and measured steady free surface elevations and discharge are compared to assess the degree of the agreement. The test with no obstacle in the flume was used to estimate the value of n in this specific experiment so as to separate the frictional effect from the effect of the flow contraction and expansion. Fig. 3 shows the computed and measured free surface variations for this test with $K = 0$. The computed free surface variations for $n = 0.01$, 0.005 and 0.003 are very similar to that shown in Fig. 3 for $n = 0.002$ partly because the measured free surface elevations at $x = 0$ and $x = 260$ cm are specified as the boundary conditions. The computed steady discharge is $Q = 0.23$, 0.45, 0.79 and 1.07 ℓ/s, respectively, in comparison with the measured discharge $Q = 1.0\ \ell/s$. Consequently, $n = 0.002$ is used for the other two tests for the flow contraction and expansion.

The typical values of $K \simeq 0.5$ for both contraction and expansion recommended by Amein and Kraus (1991) may be reasonable for large-scale horizontal contraction and expansion but it is not certain whether $K \simeq 0.5$ is reasonable for vertical contraction and expansion of the flow such as the Roadway would produce. The computed and measured free surface variations

for the tests with the steeper 1:1.8 slope of the triangular obstacle facing downstream and upstream are shown in Figs. 4 and 5 for $K = 0.5$, respectively. The computed free surface variations and discharge are not very sensitive to K in the vicinity of $K = 0.5$. The computed discharge for the test shown in Fig. 4 is $Q = 0.79$, 0.85 and 0.91 for $K = 0.6$, 0.5 and 0.4, respectively. For the test shown in Fig. 5, $Q = 0.57$, 0.62 and 0.62 ℓ/s for $K = 0.5$, 0.4 and 0.3. The computed discharge for these values of K is smaller than the measured discharge 1 ℓ/s. Figs. 4 and 5 indicate that the constant value of $K = 0.5$ yields reasonable agreement between the computed and measured free surface variations except for the dip in the vicinity of the sharp crest of the triangular obstacle. The free surface dip for an obstacle with a rounded crest may not be as pronounced as those shown in Figs. 4 and 5. In summary, these limited comparisons suggest that $K \simeq 0.5$ may be used as a first approximation for predicting the overall free surface variations over an obstacle, although the details of the free surface variations may not be predicted well, and the computed discharge may not be very accurate. The calibration of K for different obstacle shapes and orientations may somewhat improve the agreement between the computed and measured results but the last term on the right hand side of (2) added to the standard one-dimensional momentum equation may be too simple and crude to describe the detailed converging and diverging flows over an obstacle such as the Roadway.

STILLWATER ELEVATIONS ON EXISTING AND RAISED ROADWAYS

The numerical model based on (1) and (2) with $K = 0.5$ is applied to the bay system shown in Fig. 1, which is represented by 35 cross sections, 7 channels and 3 junctions. The length between node 1 and the North Bay is approximately 71,000 ft (22,000 m). The Roadway is located at node 32. The bathymetry at each cross section is specified as input. It is easy to account for the wetting and drying of subsections at each cross section in the one-dimensional model. The values of n_j for subsections are taken to be 0.02 for deep areas, 0.025 for shallow areas, and 0.035 for areas covered with vegetation. The boundary conditions of zero discharge is assumed at the landward end nodes where fresh water inflow is negligible. At node 1 seaward of the Ocean City Inlet, the temporal variation of the water surface elevation η is specified as input. The computation is initiated as a cold start and the initial conditions are taken as a horizontal water surface and zero discharge at $t = 0$. To account for the initial transition, the computation is started from the measured spring tide at node 1 before storm surge is added to the spring tide as explained below. Using the available storm tide data (Ho et al., 1976), 10 synthetic hydrographs at node 1 due to the measured spring tide and estimated storm surge of 40 and 60 hr durations are developed to represent the 10, 20, 50, 100 and 500 yr storms with two different temporal variations. The stillwater elevation used hereafter is the water surface elevation in the absence of waves above the mean sea level (the National Geodetic Vertical Datum of 1929). It is noted that the length unit in the following figures is in feet (1 ft = 0.305 m) for the convenience of users of these figures. Fig. 6 shows the specified temporal variations of the stillwater elevation at node 1 for the 50 yr storm where the 40 and 60 hr durations of the storm surge are in the intervals $t = 35$–75 hr and $t = 25$–85 hr, respectively. The peak stillwater elevation at node 1 in Fig. 6 occurs at $t = 55$ hr and is the same for both 40 and 60 hr durations.

Five different cross sections at node 32 are examined to represent the existing Roadway

and raised Roadways with the minimum elevations of 3.5, 4.0, 4.5 and 5.0 ft. The temporal variation of the stillwater elevation at node 32 is computed for these 5 cross sections at node 32 driven by each of the 10 synthetic hydrographs at node 1. Fig. 7 shows the temporal variations of the stillwater elevation at node 32 corresponding to the 50 yr storm at node 1 for the existing Roadway and the Roadway raised to a minimum elevation of 5 ft as depicted in Fig. 8. The 50 yr storm hydrograph used to drive the system at node 1 is depicted in Fig. 6. The water depth in the Ditch, shown in Fig. 8, is 6 ft below the mean sea level. It is noted that both sides of the Ditch are high because of abutments for the bridge spanning the waterway. Fig. 7 and the other computed results for 10, 20, 100 and 500 yr storms indicate that the stillwater elevation at node 32 is practically the same for the existing Roadway and the raised Roadways with the minimum elevations of 3.5, 4.0, 4.5 and 5.0 ft. This is because the stillwater elevation in the vicinity of the Roadway is essentially horizontal for storm surge and tides whose horizontal length scale is much larger than the length of the flooded Roadway. On the other hand, Fig. 7 and the other computed results indicate that for the storm with the same peak stillwater elevation at node 1, the increase of the storm surge duration from 40 hr to 60 hr does result in a slight increase of the stillwater elevation at node 32.

Fig. 9 shows the peak stillwater elevations as a function of the horizontal distance from node 1 along the main channel as depicted in Fig. 1 for the 10, 20, 50 and 100 yr storms with 40 and 60 hr durations. The computed peak stillwater elevations along the main channel are practically the same for the existing Roadway and the Roadways raised to a minimum elevation of 3.5, 4.0, 4.5 and 5.0 ft. The peak stillwater elevations computed for the 500 yr storm are not shown in Fig. 9 because breaching of the barrier island separating the Atlantic Ocean and the Bays may occur during the 500 yr storm and increase the peak stillwater elevations in the Bays. In the absence of breaching of the barrier island, the peak stillwater elevations decrease rapidly in the vicinity of the Ocean City Inlet and remain almost the same in the South and North Bays for each storm with a specified duration. For the same peak stillwater elevations at node 1, the 60 hr storm surge increases the peak stillwater elevation at node 32 by about 0.3 ft in comparison to the 40 hr storm surge. There is little historical storm surge data for the Bays. For the 1991 Halloween Storm, the peak elevation recorded at the NOAA tide gage at Ocean City, Maryland was 5.5 ft, while the Delaware Department of Natural Resources and Environmental Control reported a peak elevation of 4.0 ft in the North Bay. The recurrence interval associated with this storm was considered to be about 10 yr. The computed results for the 10 yr storm shown in Fig. 9 are at least qualitatively consistent with this limited data.

CONCLUSIONS

The numerical model for a network of one-dimensional channels is applied to examine flooding of the Roadway between the Bays due to storm surge and tides through the Ocean City Inlet. A small-scale experiment for steady flow over an obstacle was conducted to assess the capability of the numerical model based on a constant contraction-expansion coefficient K. The numerical model with $K = 0.5$ is shown to be capable of predicting the overall free surface variation over the obstacle, although the detailed free surface variation and discharge may not be predicted very accurately. The numerical model with $K = 0.5$ is then applied

to predict the stillwater elevations at the existing and raised Roadways for different storms. The computed results indicate that the raised Roadway with the minimum elevation of 5 ft or less will not increase the essentially horizontal stillwater elevations in the vicinity of the Roadway such as a dam located on a sloping channel bottom might. The computed peak stillwater elevations seem to be consistent with limited available data but need to be verified using more comprehensive and quantitative data.

ACKNOWLEDGEMENTS

This study is supported by the Delaware Department of Transportation. The U.S. Army Corps of Engineers, Philadelphia District and the firm Rummel · Klepper & Kahl provided necessary information for this study.

REFERENCES

Amein, M. and N.C. Kraus, 1991. DYNLET1: Dynamic implicit numerical model of one-dimensional tidal flow through inlets. **Tech. Rept. CERC-91-10**, Coast. Engrg. Res. Ctr., Vicksburg, Mississippi.

French, R.H., 1985. *Open-Channel Hydraulics*, McGraw-Hill, New York, NY.

Ho, F.P., R.J. Tracey, V.A. Myers, and N.S. Foat, 1976. Storm tide frequency analysis for the open coast of Virginia, Maryland and Delaware. *NOAA Tech. Memo. NWS HYDRO-32*, NOAA, NWS, Office of Hydrology, U.S. Dept. of Commerce, Silver Spring, Maryland.

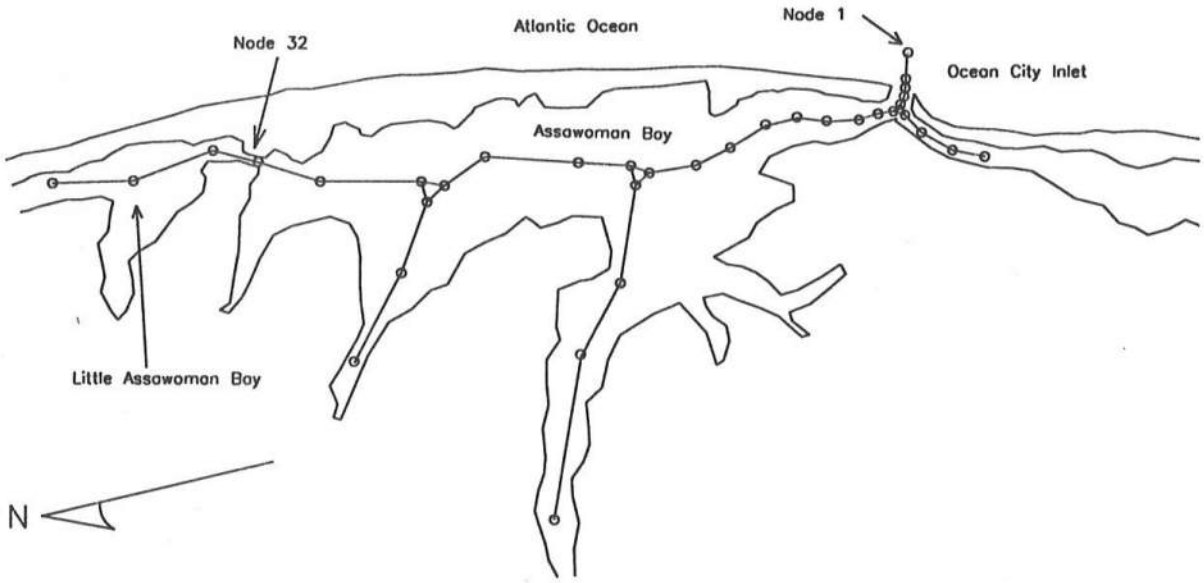

Figure 1: Flooding of Delaware Route 54 at node 32 between Little Assawoman Bay and Assawoman Bay due to Storm Surge and Tide through Ocean City Inlet, Maryland.

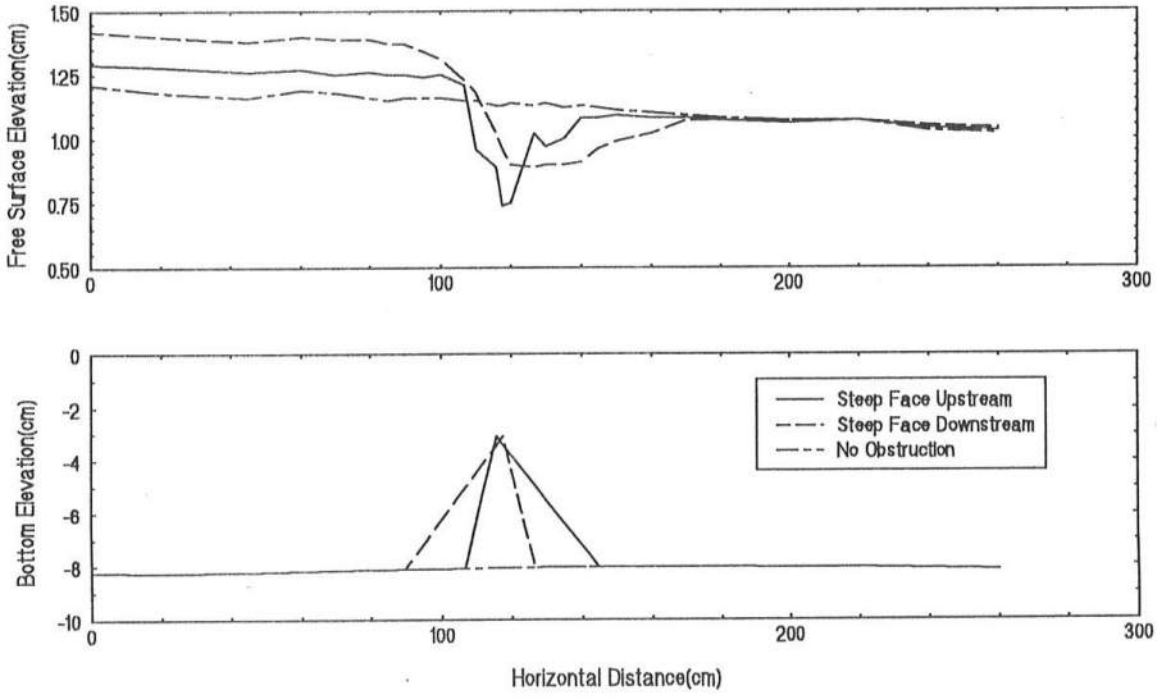

Figure 2: Measured Free Surface and Bottom Elevations for Three Tests.

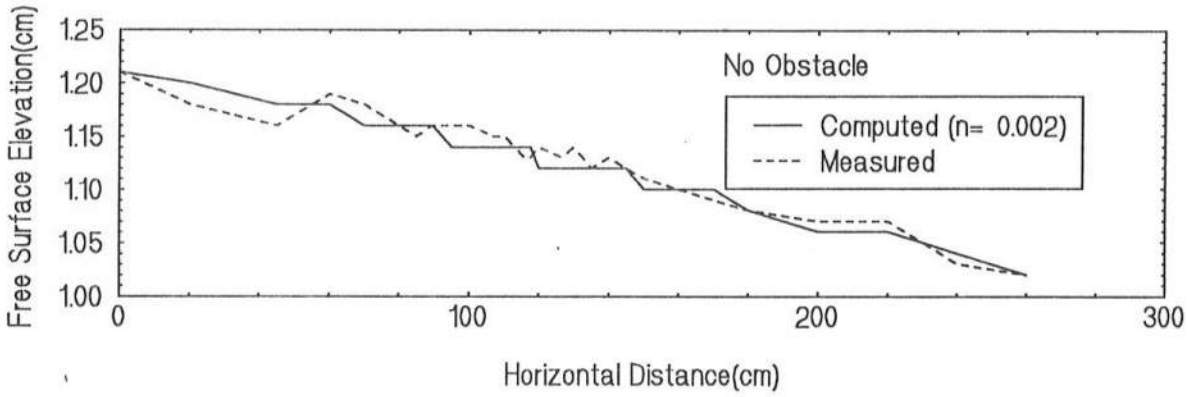

Figure 3: Measured and Computed Free Surface Variations for Test with no Obstacle.

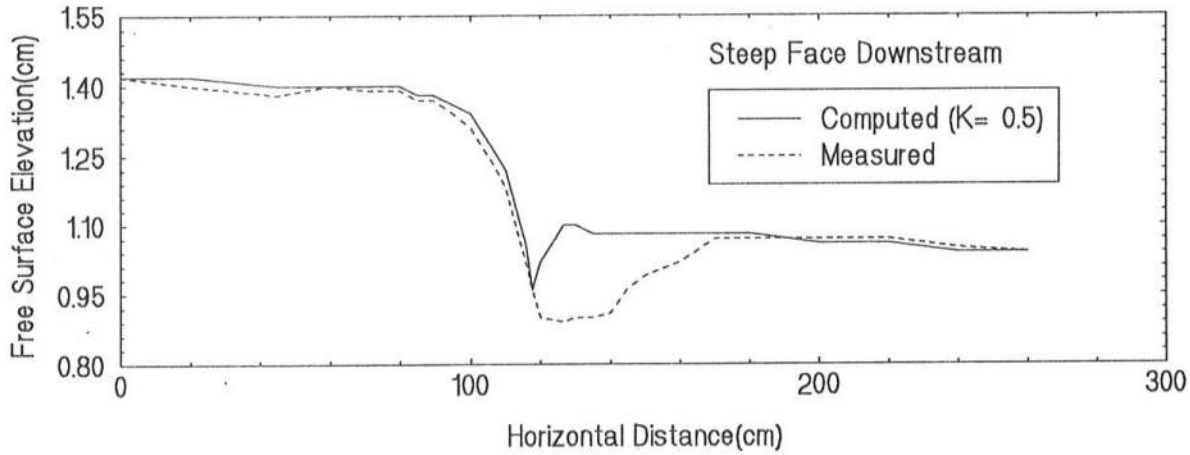

Figure 4: Measured and Computed Free Surface Variations for Test with Steeper Slope Facing Downstream.

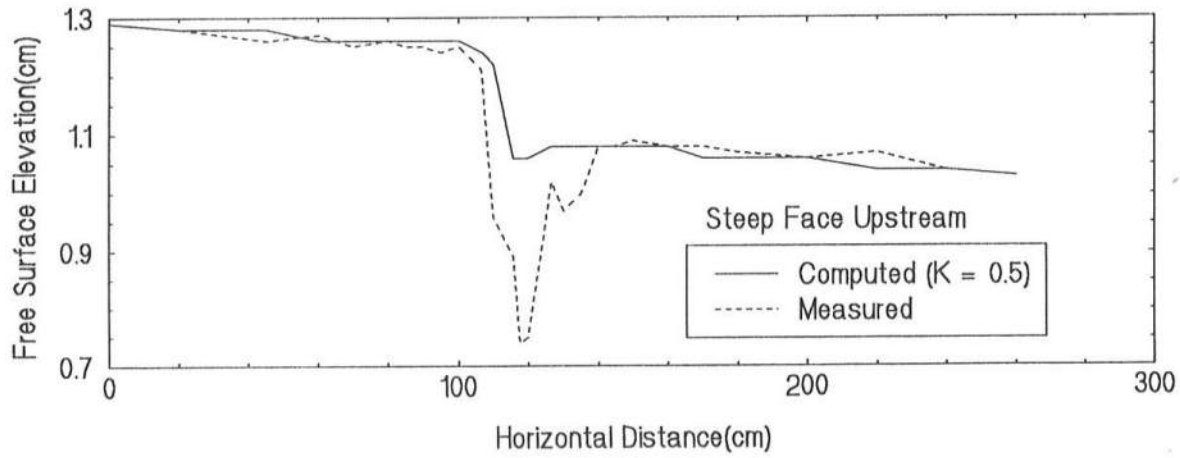

Figure 5: Measured and Computed Free Surface Variations for Test with Steeper Slope Facing Upstream.

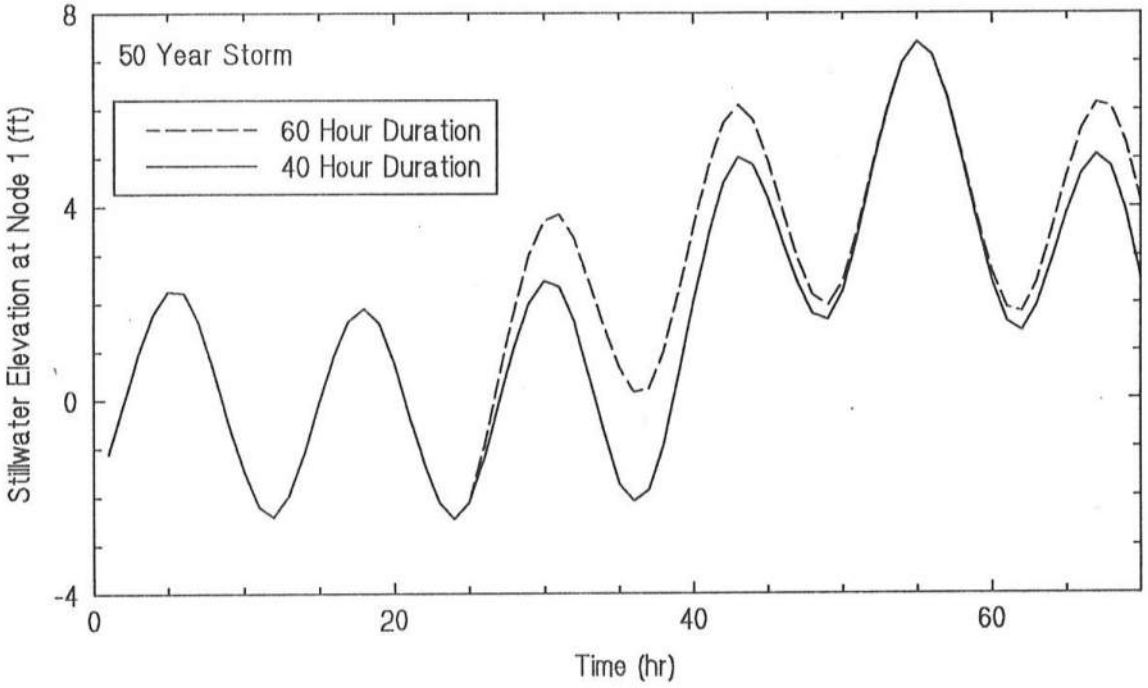

Figure 6: Specified Temporal Variations of Stillwater Elevation at Node 1 for 50 yr Storm.

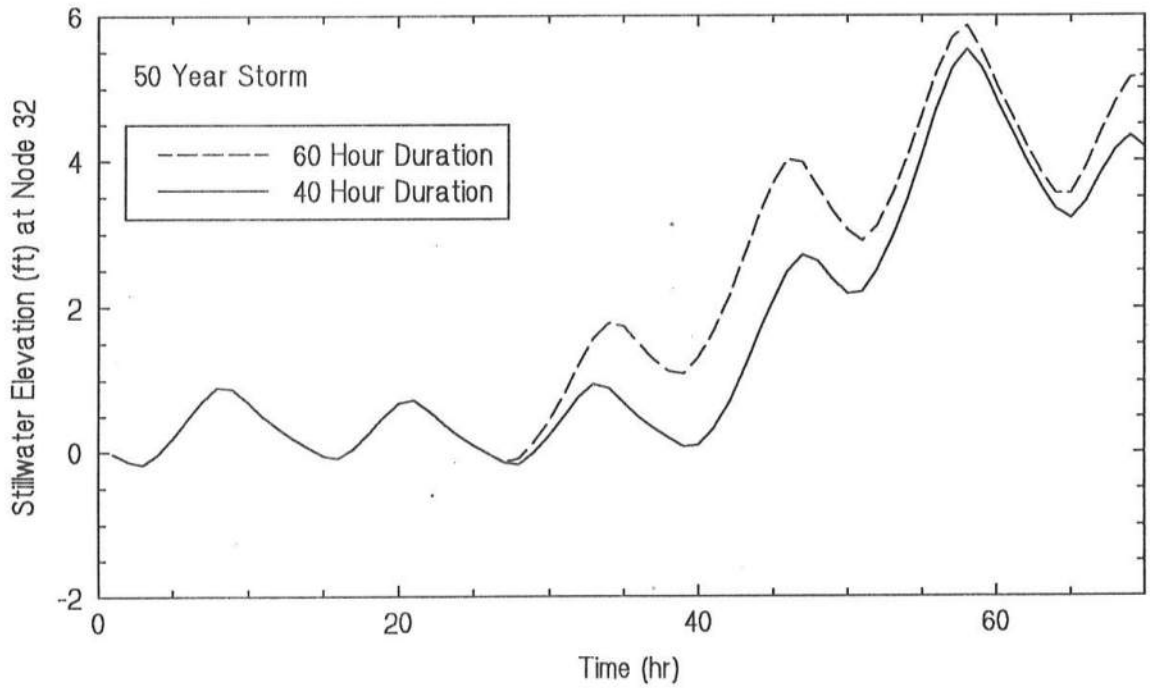

Figure 7: Computed Temporal Variations of Stillwater Elevation at Node 32 for 50 yr Storm.

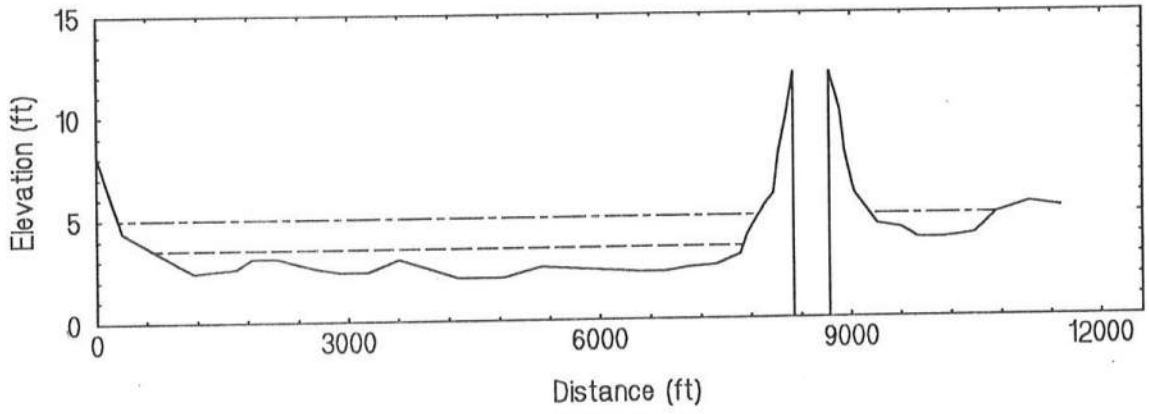

Figure 8: Cross Sections for Existing and Raised Roadways.

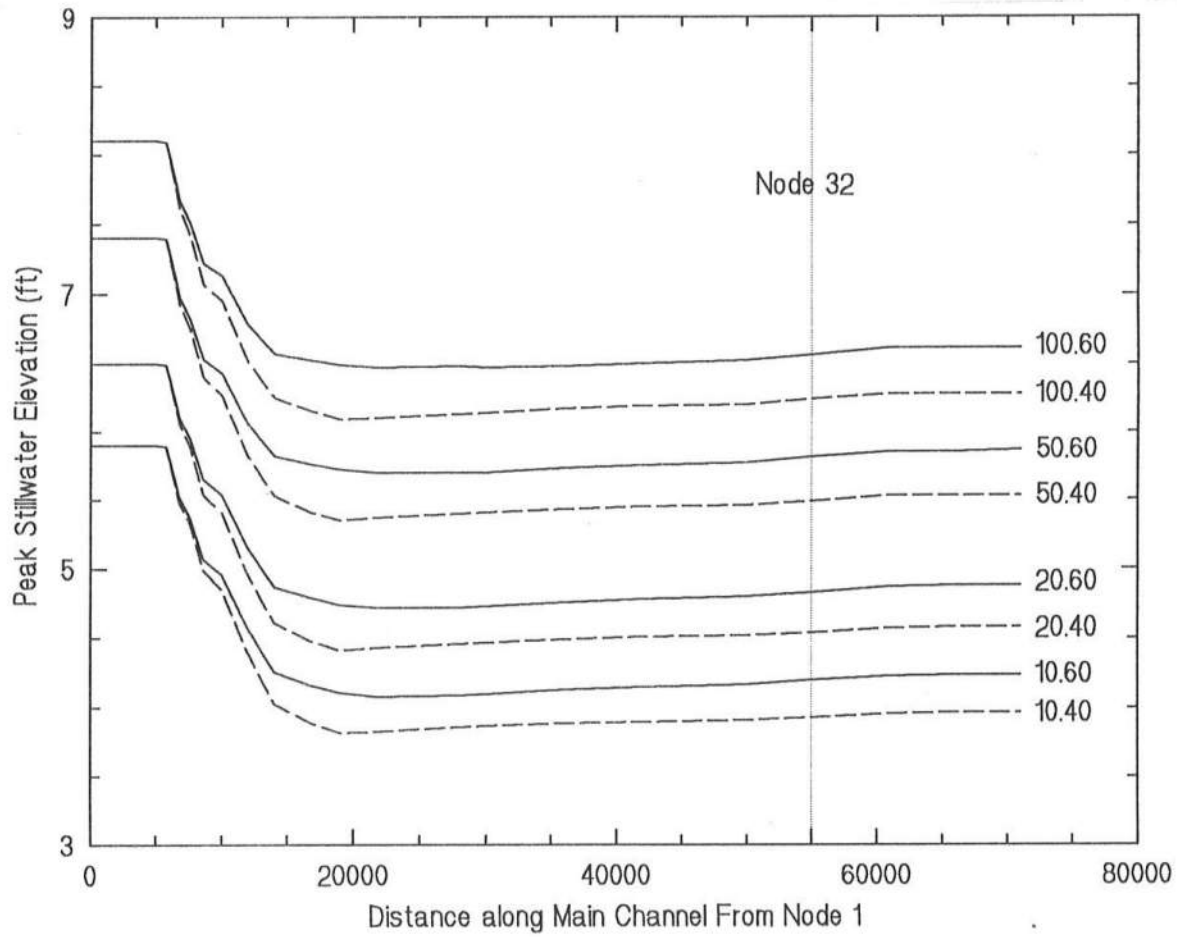

Figure 9: Peak Stillwater Elevations as a Function of Horizontal Distance along Main Channel from Node 1 for 10, 20, 50 and 100 yr Storms.

The Propagation of Water Waves in Channels

Robert A. Dalrymple, James T. Kirby, and Li Li
Center for Applied Coastal Research
Ocean Engineering Laboratory
University of Delaware, Newark, DE 19716

Abstract

Short waves in a channel can present navigational problems and may excite harbor oscillations. Channel sidewalls may reduce much of this wave energy, if they are sufficiently porous or they are sloped. Here we present a model for wave propagation in prismatic channels of arbitrary cross-section utilizing a numerical eigenfunction expansion. Sloping sidewalls are shown to produce edge wave motions.

Introduction

Long waves in channels have served to provide much of the impetus for the study of waves. Kelland (1839, as cited in Lamb, 1945) provided a wave equation for waves in prismatic channels of arbitrary cross-section. Scott Russell (1844) provided evidence for the presence of solitary waves in channels. More recent work is Peregrine (1968, 1969), who examined nonlinear long waves in narrow channels, and Mathew and Akylas (1990), who examined the wide channel case, noting the three-dimensional nature of the waves.

Here we treat short waves, such that the depth/wave length ratio can exceed 1/20. For straight channels with rectangular cross-sections of width $2b$, the wave propagation problem can be viewed as a summation of simple wave modes, whose amplitudes are determined at the mouth of the channel. For example, Dalrymple (1989), examining waves in rectangular channels past abrupt changes in cross-section, expanded the wave field in cross-channel eigenmodes,

$$\cos(\lambda_n y), n = 0, 1, 2, \ldots, \tag{1}$$

where $\lambda_n = n\pi/b$. Each of these modes satisfies a no-flow boundary condition at the vertical sidewalls. The total (forward-propagating) wave potential satisfies the Laplace equation and is given by

$$\widehat{\phi}(x,y)\ \frac{\cosh k(h+z)}{\cosh kh}\ e^{-\mathrm{i}\omega t}$$

where

$$\widehat{\phi}(x,y) = e^{\mathrm{i}kx} + \sum_{n=1}^{\infty} A_n\ e^{\mathrm{i}\sqrt{k^2-\lambda_n^2}x} \cos \lambda_n y \tag{2}$$

and k is the wave number, given by the usual linear theory dispersion relationship. This methodology is a discrete form of the *angular spectrum* modelling methodology (e.g., Dalrymple and Kirby, 1992). Dalrymple and Kirby (1988, §3.3) used this angular spectrum approach for waves diffracting into a wide channel.

Dalrymple (1992) examined dissipation of wave energy into channel sidewalls (motivated by the experimental results of Melo and Guza, 1991, which showed dramatic decreases of wave energy). He used an impedance boundary condition at the sidewalls,

$$\frac{\partial \widehat{\phi}}{\partial y} = i\gamma\widehat{\phi} \tag{3}$$

where γ is k (the wave number) times the specific admittance β of the jetties, which is determined empirically. The lateral eigenfunctions that satisfy the boundary conditions at the sidewalls are the same as before (1), but a new relationship establishes the values of λ_n:

$$-\lambda_n \tan \lambda_n b = \mathrm{i}\gamma \tag{4}$$

For channels that are narrow with respect to a wave length, he obtained an exponential wave height decay along the channel centerline depending on the real part of β divided by b (so that the wave decay is less for wider channels). In addition, the effect of uniform currents in the channel was discussed.

Most navigational channels do not have prismatic cross-sections. For example, jettied channels are often trapezoidal in cross-section. Isaacson (1978) has empirically studied the attenuation of waves along a trapezoidal channel with rubble sidewalls. For this case, a mathematical treatment involves lateral eigenfunctions other than the cosines used for a rectangular channel. In this paper, a numerical approach is presented to find the eigenfunctions and the resulting wave motion in prismatic channels. (For non-prismatic channels, the change of the eigenfunctions along the channel also must be taken into account.)

Theory

The wave motion in a channel (for which all of the fluid lies under the free surface; no overhanging banks) is governed by the mild-slope equation (Berkhoff, 1972), which is

transformed into a variable coefficient Helmholz equation (Radder, 1979):

$$\frac{\partial^2 \widehat{\phi}}{\partial x^2} + \frac{\partial^2 \widehat{\phi}}{\partial y^2} + K^2 \widehat{\phi} = 0, \text{ where } K(y) = k^2 - \frac{\nabla^2 \sqrt{CC_g}}{CC_g}$$

with x, the propagation direction, y across the channel, and z vertically upwards from the still water level. Again, k is the wave number, and C and C_g are the phase and group velocity, corresponding the dispersion relationship, $\omega^2 = gk \tanh kh$. Kirby (1994) has shown that this form of the mild slope equation avoids singularities at the shoreline for sloping channel sidewalls. Introducing $\overline{K^2}$ as a cross-channel averaged value of K^2, this equation may be written as

$$\frac{\partial^2 \widehat{\phi}}{\partial x^2} + \frac{\partial^2 \widehat{\phi}}{\partial y^2} + \overline{K^2}\,(1-\nu)\,\widehat{\phi} = 0, \text{ where } \nu(y) = 1 - \frac{K^2}{\overline{K^2}}$$

Separation of variables, $\widehat{\phi} = X(x)Y(y)$, leads to two equations:

$$\frac{\partial^2 Y}{\partial y^2} + \left(\lambda^2 - \overline{K^2}\,\nu(y)\right) Y = 0 \tag{5}$$

$$\frac{\partial^2 X}{\partial x^2} + \left(\overline{K^2} - \lambda^2\right) X = = 0 \tag{6}$$

For a rectangular cross-section, ν, which measures the cross-channel variation in K^2, is zero, and the cosine cross-channel modes given in (2) result from Eq. (5). For non-rectanguler cross-sections, the second term in Eq. (5) for Y has a variable coefficient. There are few analytical representations.

For arbitrary prismatic cross-section, (5) may be solved numerically by finite differences. Representing the y axis as $y = j\Delta y$ and $Y(y)$ as Y_j, we can represent (5) as

$$Y_{j+1} - \left((\widehat{K^2}\nu_j - \lambda^2)\Delta y^2 + 2\right) Y_j + Y_{j-1} = 0 \quad j = 1, 2, \ldots, N$$

and we use the finite difference equivalent of the no-flow (or impedance) boundary conditions at the sidewalls. The resulting numerical eigenvalue problem has as many eigenvalues (λ_n) and eigenfunctions as there are interior grid points (N). Each of these numerical eigenfunctions is then used with the solution of the X equation, which is simply

$$X(x) = A_n e^{\mathrm{i}\sqrt{\overline{K^2} - \lambda_n^2}\, x}$$

where A_n is the contribution of mode Y_n to the initial condition at $x = 0$ (the channel mouth), which is found by using the orthogonality of the eigenfunctions. (Numerical accuracy precludes using much more than $N/2$ modes; therefore N is chosen to be large.)

If K^2 varies down the channel (that is, the channel is not prismatic), then the solutions for X and Y must be obtained at each location down the channel.

Results

Rectangular Channel

To test the methodology, a comparison was made to the analytic model of Dalrymple (1992) for waves in a straight channel with rectangular cross-section of width $2b$. An impedance boundary condition (3) was used to permit wave energy dissipation in porous channel sidewalls. Figure 1 shows the instantaneous wave field ($\eta(x,y) = -(\mathrm{i}\omega/g)\phi(x,y,0)$) and the absolute value of η in a channel with the following characteristics: $l = 2000m$, $b = 120m$, $h = 8m$, $T = 12s$, and the specific admittance is 0.156, which gives $\gamma = 0.012m^{-1}$. (The numerical model was run with grid sizes: $dx = 3.3389m$, $dy = 4.m$, $N = 61$) Note the decay of the wave height with distance along the channel and the curvature of the wave crests due to the propagation of the waves into the dissipative boundaries. (Another analytic treatment of this problem is in Martin and Dalrymple, 1994.)

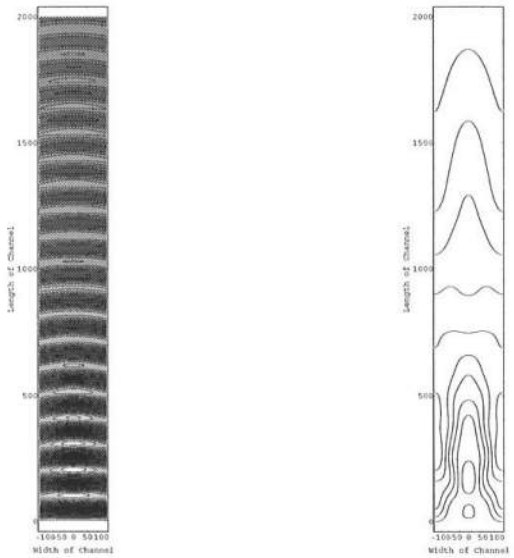

Figure 1: Plan View of Instantaneous Water Surface Elevation (left) and Absolute Value of Water Surface Elevation (right) (Contours Intervals in Contour Plot are 0.1)

The absolute magnitude wave height decay down the channel centerline for this example is given by Dalrymple (1992: $H = H_0 \exp(-\Gamma x)$, where $\Gamma = \gamma/(2kb)$). The difference between this and the numerical results is not large, if an initial focussing of the waves near the mouth of the channel ($x \simeq 200$m) is neglected. The assumed initial condition of normally incident waves with unit amplitude across the channel mouth (that is, neglecting the diffraction of the incident waves by the breakwater tips) leads to a forced phasing of all the modes which comprise the wave field, such that, as

the waves propagate down the channel, there is an (unrealistic?) focussing after one wavelength for this wave period.

Also, there were no discernable differences between the numerically-determined eigenfunctions for the numerical solution and exact cosine eigenfunctions, Eq. (1).

Triangular Channel

Kelland (1879, as cited in Lamb, Art. 261, 1945) considered an infinitely long straight channel with a triangular cross section with the sidewalls inclined at 45^o to the vertical. He obtained an analytical solution for arbitrary water depth, which, for shallow water, corresponds to a zero mode edge wave on the channel sidewall. Macdonald (1894, also cited in Lamb, 261, 1945) treats sidewalls with a 60^o angle analytically.

The left part of Figure 2 shows the instantaneous wave field in a triangular channel, which has the following characteristics: width=16 m, length=100 m, height(deepest)=8 m, $T = 2.05s$. (The numerical model was run with grid sizes: $dx = 0.2506m$, $dy = 0.1333m$, $N = 121$.) Clearly the incident wave train has excited shorter wavelength edge waves along the sloping side walls, while the incident wave train persists in the center of the channel. The corresponding numerical eigenfunctions are also shown in Figure 2. For each of the eigenmodes, there is an even and an odd shape about the centerline. The magnitude of all the odd modes is (numerically near) zero, while the amplitudes of the even modes decrease rapidly. For this case, the zero mode even edge wave amplitude is 1.0, the next eigenmode has a magnitude of 0.443, and the third mode has an amplitude of only 0.013. Therefore only three of the eigenmodes account for most of the wave motion.

Trapezoidal Channel

The third example consists of a straight channel with a trapezoidal cross-section. The channel is $150m$ long, $26.72m$ wide, $3m$ deep. The sidewalls are (mildly) inclined at 80^o from the vertical (downward) direction. The wave period $T = 2.2s$. Figure 3 shows the instantaneous wave field. Again, with the sloping sidewalls, edge wave modes are excited. This time, as seen in lower part of Figure 3, edge wave modes zero through five are excited; however, the higher modes merge across the channel. (The numerical model was run with grid sizes: $dx = 0.75188m$, $dy = 0.5041m$, $N = 124$.)

Arbitrary Channel Cross-section

The first example is a straight channel with cross section seen in Figure 4. The channel is $8.2m$ wide, $40m$ long, $2m$ deep at the largest depth, $1m$ at the smallest depth. The

wave period is $2s$. Figure 5 shows the instantaneous wave field and the first five eigenfunctions. This channel cross-section is similar to the analogous case of a circular channel with a flat bottom, conformally mapped to a straight channel. For the arbitrary cross-section channel, the waves are refracted to the right side of the channel, for the circular channel analog, the waves propagate towards the outer side wall due to the curvature of the channel (which bends to the left for this case), cf. Kirby *et al.*, 1994; Dalrymple *et al.*, 1994. (The numerical model was run with grid sizes: $dx = 0.0802m$, $dy = 0.328m$, $N = 25$.)

The second example has the same cross section as the previous example. The channel is now wider ($50m$), $100m$ long, $2m$ in the largest depth, $1m$ in the smallest depth, wave period is $5s$. Figure 6 shows the instantaneous snapshot of the free surface. Clearly the effect of the different wave period and cross-sectional width leads to more refraction to the right sidewall. In the analog to a circular channel, this corresponds to a wider channel, with diffraction on the inner wall, as the wave curve around the bend and reflection from the outer sidewall. (The numerical model was run with grid sizes: $dx = 0.2004m$, $dy = 1.m$, $N = 50$.)

The third example is a straight channel with cross section seen in Figure 7. Channel is $8.2m$ wide, $60m$ long, $3m$ in the largest depth, wave period is $2.5s$. Figure 8 shows the instantaneous wave field and the first five eigenfunctions. (The numerical model was run with grid sizes: $dx = 0.12024m$, $dy = 0.341667m$, $N = 25$.)

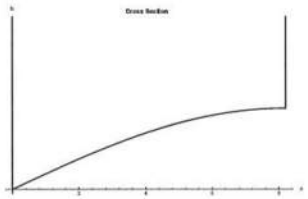

Figure 4: Cross Section of Arbitrary Channel (Case 1)

Conclusion and Discussion

Examples of a numerical methodology for computing short wave fields in prismatic channels have been given for several channel geometries: a straight rectangular channel (to compare with the simple analytic solution), a triangular channel, a trapezoidal channel, and finally a channel with arbitrary cross-section.

For each case, the water surface displacement created by a uniform wave train

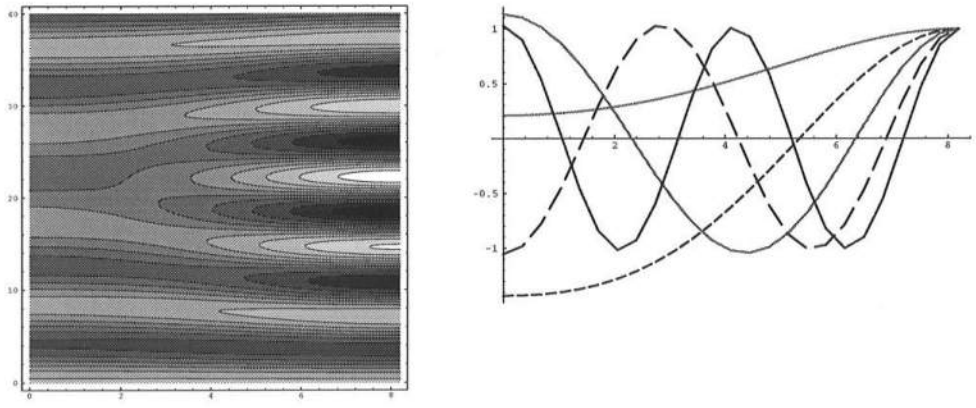

Figure 5: Wave Field and Eigenfunction for Waves in Arbitrary Channel (Case 1)

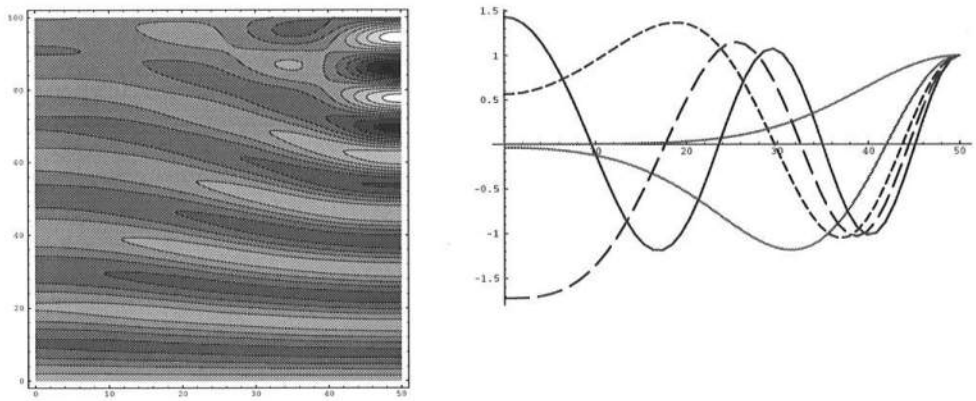

Figure 6: Wave Field and Eigenfunctions for Waves in Arbitrary Channel (Case 2)

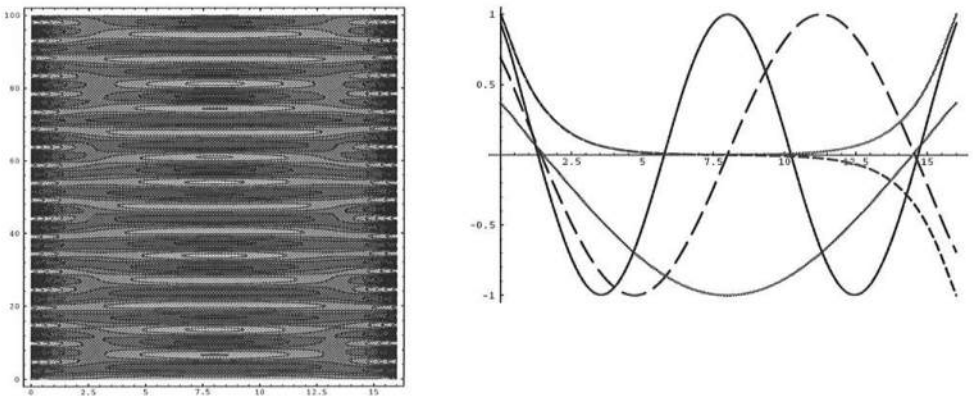

Figure 2: Instantaneous Wave Field and Eigenfunctions for Waves in a Triangular Channel

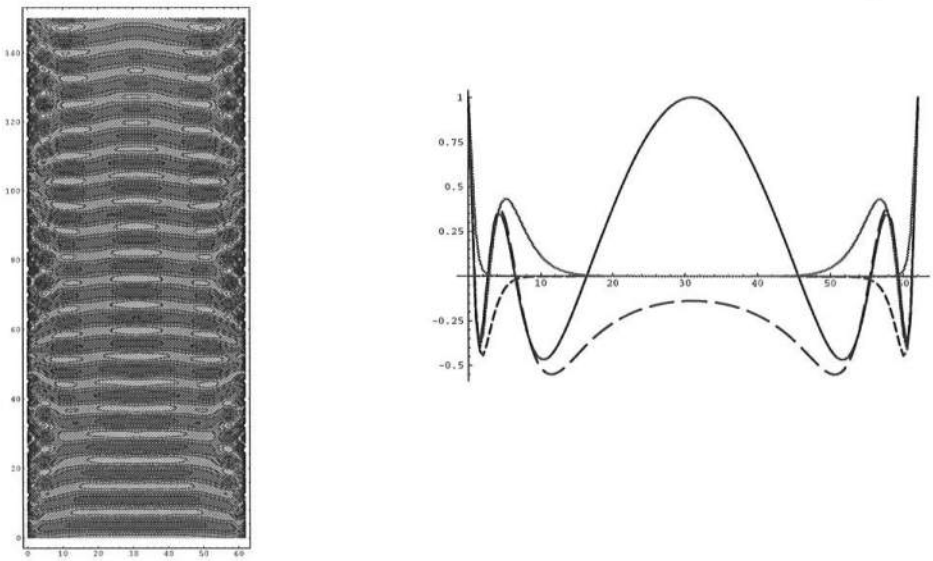

Figure 3: Wave Field and Eigenfunctions for Wave in Trapezoidal Channel

normally incident on the channel is shown. This surface displacement is a superposition of the eigenmodes, determined numerically from the lateral eigenvalue problem.

Channels with sloping sidewalls give rise to the presence of edge waves, excited by the incident wave field. These edge waves have a different wave length than the incident wave field and they are the largest at the shoreline, hence providing potential for greater wave damage and erosion there. Wave breaking has been ignored in this linear analysis, but may be of importance in the field.

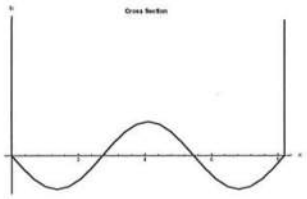

Figure 7: Cross Section of Arbitrary Channel (Case 3)

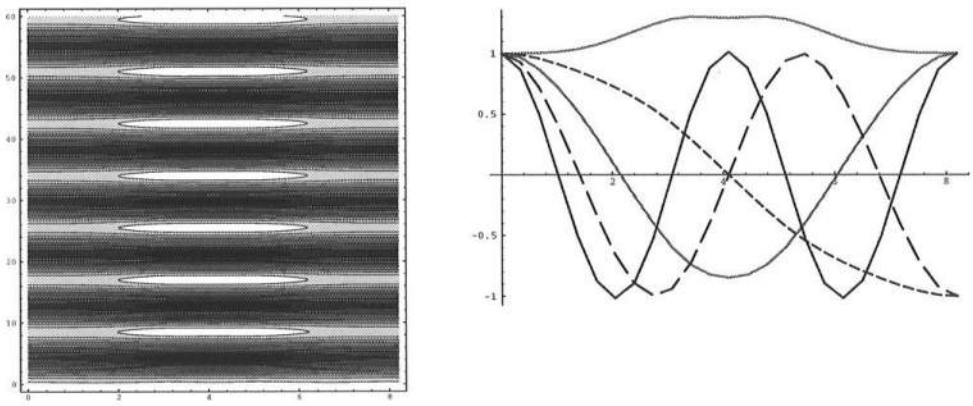

Figure 8: Wave Field and Eigenfunctions for Waves in Arbitrary Channel (Case 3)

Acknowlegments: This work was partially funded by the NOAA Office of Sea Grant, Department of Commerce under Grant No. NA16RG0162-02 (R/OE-12 and R/OE-13). The U.S. Government is authorized to produce and distribute reprints for government purposes notwithstanding any copyright notation that may appear herein.

References

Berkhoff, J.C.W. 1972. Computation of Combined Refraction-diffraction. *Proc. 13th Intl. Coastal Engrg. Conf.*, ASCE, Vancouver, 471-490.

Dalrymple, R.A. 1989. Water Waves Past Abrupt Channel Transitions. *Applied Ocean Research*, 11, 4.

Dalrymple, R.A. 1992. Water Wave Propagation in Jettied Channels. *Proc. 23rd Intl. Coastal Engrg. Conf.*,, ASCE, Venice, 3040-3053.

Dalrymple, R.A. and J.T. Kirby, 1988. Models for Very Wide Angle Water Waves and Wave Diffraction. *Journal of Fluid Mechanics*, 192, 33-5.

Dalrymple, R.A. and J.T. Kirby, 1992. Angular Spectrum Modelling of Water Waves. *Reviews in Aquatic Sciences*, CRC Press, 6, Iss. 5 and 6, 383-404, 1992.

Dalrymple, R.A., J.T. Kirby, and P.A. Martin, 1994. Spectral Methods for Forward-propagating Water Waves in Conformally-mapped Channels. Center for Appld. Coastal Res., Univ. Delaware, CACR-94-01.

Isaacson, M. St.Q. 1978. Wave Dampening due to Rubblemound Breakwaters. *J. Waterways, Port, Coastal and Ocean Engrg.*, ASCE, 117, 5, 493-510.

Kirby, J.T. 1994. Free-surface Oscillations in a Basin: the Mild-slope Equation and Radder's Transformation. In preparation.

Lamb, H. 1945. **Hydrodynamics**, 6th ed., Dover Press.

Martin, P.A. and R.A. Dalrymple. 1994. On the Propagation of Water Waves Along a Porous-walled Channel. *Proc. Royal Society, London, A*, 444, 411-428.

Mathew, J. and T.R. Akylas. 1990. On Three-dimensional Long Water Waves in a Channel with Sloping Sidewalls. *J. Fluid Mech.*, 215, 289-307.

Melo, E. and R.T. Guza. 1991. Wave Propagation in a Jettied Entrance Channel, II: Observations. *J. Waterways, Port, Coastal and Ocean Engrg.*, ASCE, 117, 5, 493-510.

Peregrine, D.H. 1968. Long Waves in a Uniform Channel of Arbitrary Cross-section. *J. Fluid Mech.*, 32, 2, 353-365.

Peregrine, D.H. 1969. Solitary Waves in Trapezoidal Channels. *J. Fluid Mech.*, 35, 1, 1-6.

Radder, A.C. 1979. On the Parabolic Equation Method for Water-wave Propagation, *J. Fluid Mech.*, 95, 159-176.